eXPRESS Polymer Letters Vol.10, No.12 (2016) 964
Available online at www.expresspolymlett.com
DOI: 10.3144/expresspolymlett.2016.89

Editorial corner – a personal view

Molecular architecturing in thermosets – Still chance 'at the bottom'?

J. Karger-Kocsis[1], *S. Grishchuk*[2]

[1]Department of Polymer Engineering, Faculty of Mechanical Engineering, Budapest University of Technology and Economics, H-1111 Budapest, Hungary
[2]Institute for Composite Materials, TU Kaiserslautern, D-67663 Kaiserslautern, Germany

Major goal of materials science is property improvement. Modification of thermosets with fillers and reinforcements of micro- and macroscale appearance is considered as one the right tools for property tailoring. In the meantime, the related knowledge and know-how gained is successfully transferred to nanoscale resulting in numerous thermosetting nanocomposites. Toughening of highly crosslinked resins has been under focus of interest all the time. Common aspect of toughening strategies is the creation of micro- and nanoheterogeneous systems in which cavitation/debonding-induced shear deformation of the matrix resin prevails. It is widely accepted that the molecular network of the crosslinked resin itself is homogeneous. This is not obvious since resins and hardeners are multifunctional compounds, and thus the reactivity of primary and secondary functionalities are different. Depending on reaction conditions, this can influence the compatibility of growing chains during cure. Therefore, kinetically driven phase separation or nanostructuring could occur. Several experimental and theoretical reports suggest formation of a nanoheterogenous structure of thermosets. This may be expected when intra- and intermolecluar crosslinking occur separately which may happen during co-crosslinking (e.g styrene crosslinked vinylester (DOI: 10.3144/expresspolymlett.2013.38)), formation of interpenetrating networks, and different chemical pathways in hybrid resins. However, the frequently observed nanoscale nodular morphology in epoxy resins (DOI: 10.1016/j.matlet.2015.12.066) may be an experimental artifact (DOI: 10.1016/j.polymer.2014.06.030). Unfortunately, the range of the experimental techniques for morphology detection of thermosets is limited. Moreover, no physical etching techniques proved to be artifact-free. There are several possibilities for network architecturing. The easiest and widely practiced way, is to control the network density. This, however, still yields a quasi-homogenous morphology. Can we introduce some regular inhomogeneity in the network structure in order to improve toughness and other mechanical parameters? Recent strategies focus on the creation of 'partially reacted substructures' (DOI: 10.1021/acs.macromol.5b00677), build-up of dangling chains in the network (DOI: 10.1177/1045389X13478275), controlled topological structuring (DOI: 10.1016/j.polymer.2016.07.038), also via vitrimer chemistry (DOI: 10.1039/C5SC02223A). The outcome may be comparable with that of tougheners incorporated via reaction induced phase separation. Further possibilities for network tailoring can be expected from molecular dynamics simulation studies (e.g. DOI: 10.1021/acs.macromol.5b01183). So, there is still 'plenty room at the bottom' (R. Feynman, 1959) for thermosets - why not explore it?

Prof. Dr. Dr. h.c.
József Karger-Kocsis
Editor-in-Chief

Dr. Sergiy Grishchuk

---

*Corresponding author, e-mail: karger@pt.bme.hu

eXPRESS Polymer Letters Vol.10, No.12 (2016) 965–976
Available online at www.expresspolymlett.com
DOI: 10.3144/expresspolymlett.2016.90

Spherical and rod-like dialdehyde cellulose nanocrystals by sodium periodate oxidation: Optimization with double response surface model and templates for silver nanoparticles

F-F. Lu[1], H-Y. Yu[1,2*], Y. Zhou[1], J-M. Yao[2]

[1]The Key Laboratory of Advanced Textile Materials and Manufacturing Technology of Ministry of Education, College of Materials and Textiles, Zhejiang Sci-Tech University, 310018 Hangzhou, China
[2]National Engineering Lab for Textile Fiber Materials & Processing Technology, Zhejiang Sci-Tech University, 310018 Hangzhou, China

Received 12 April 2016; accepted in revised form 30 June 2016

Abstract. A novel double response surface model is used first time to optimize a regioselective process to prepare spherical dialdehyde cellulose nanocrystals (SDACN) and rod-like dialdehyde cellulose nanocrystals (RDACN) via one-step sodium periodate ($NaIO_4$) oxidation. The influence of four preparation factors (solid-liquid ratio, $NaIO_4$ concentration, reaction time and temperature) on the yields and aldehyde contents of the final products were evaluated. For comparison, rod-like cellulose nanocrystals (CN-M and CN-S) were prepared by hydrochloric/formic acid hydrolysis and sulfuric acid hydrolysis, respectively. The RDACN shows high crystallinity of 82%, while SDACN presents low crystallinity due to the high degree of oxidation. Thus, SDACN has poorer thermal stability than RDACN and CN-M, but higher than CN-S. Compared to CN-M, SDACN with higher aldehyde contents as templates is beneficial to deposit more Ag nanoparticles with diameters of 30±4 nm and the resultant nanohybrids exhibit good antibacterial activities against both Gram-negative *E. coli* and Gram-positive *S. aureus.*

Keywords: *nanomaterials, dialdehyde cellulose nanocrystals, $NaIO_4$ oxidation, response surface model, antibacterial activity*

1. Introduction

Recently, cellulose nanocrystals (CNs) with various morphologies (rod-like or spherical) isolated from the most abundant cellulosic materials have gained increasing attention in some fields such as antimicrobial packagings [1, 2], template for metallic nanoparticles [3], aerogels for wastewater treatment [4], drug delivery [5], and protein immobilization [6] due to their excellent properties, including easily modified functional groups, high specific area, aspect ratios, and outstanding stiffness. As the nanofillers, the requirement of CNs surface group varies with the different applications. The traditional methods like acid hydrolysis [4, 7], enzyme-assisted hydrolysis [8] and mechanical treatments [9] can extract the CNs with hydroxyl groups, which are usually modified into other functional groups for further applications. Recently, CNs with functional groups (carboxyl or aldehyde groups) have been developed by 2,2,6,6-tetramethylpiperidinyl-1-oxyl (TEMPO) [10, 11], ammonium persulfate (APS) [12], two-step approach combined acid hydrolysis and $NaIO_4$ oxidations [13–15], and one-step $NaIO_4$ oxidation [16]. The TEMPO and APS oxidations consume for a long time and the oxidizing agents are toxic [10, 12]. So that, there are growing interests in the preparation of dialdehyde

---

[*]Corresponding author, e-mail: phdyu@zstu.edu.cn

cellulose nanocrystal (DACN) by two-step approach $NaIO_4$ oxidation, in which DACN with 50–376 nm in length and 3–18 nm in diameter were prepared by the sulfuric acid hydrolysis of fibers (cotton fibers and bleached softwood pulp) and then $NaIO_4$ oxidation [13–15]. However, the two-step approach $NaIO_4$ oxidation was complicated and needed environmental unfriendly acid hydrolysis process that leads to the low yield of DACN. More recently, one-step $NaIO_4$ oxidation was used to fabricate DACN efficiently [16]. Theoretically, the $NaIO_4$ oxidation can selectively convert hydroxyl groups on the cellulose into aldehyde groups and form CNs by oxidative cleavage between at C_2 and C_3 bonds of the glucose repeat units [17, 18]. The aldehyde groups on the DACN surfaces can be used as the binding site for the fluorescent bioimaging [19] and nanohybrid templates [1, 2, 20]. Yang *et al.* [16] obtained the rod-like DACN with length of 100–200 nm and diameter of 5 nm by $NaIO_4$ oxidation of sheet from kraft softwood pulp after soaking in the water for 2 days, but the oxidation process needed long reaction time of 96 h with stirring speed of 105 rpm. From above, these mentioned oxidation methods were inefficient and the influence model of reaction conditions on the morphology, yield and aldehyde content of DACN has not been established.

In this work, a novel double response surface model on yield and aldehyde content was established to optimize the regioselective extraction of spherical and rod-like DACN from microcrystalline cellulose by a one-step $NaIO_4$ oxidation method without additives within a shorter reaction time. The morphologies, microstructures and properties of the resultant DACN were investigated, and their potential application as a template for nanohybrids was also evaluated.

2. Experimental

2.1. Materials

Commercial microcrystalline cellulose (MCC, rubby-shaped fragments with particle size of 15–30 μm) was purchased from Shanghai Chemical Reagents (Shanghai, China). Sodium periodate ($NaIO_4$), silver nitrate ($AgNO_3$), hydrochloric acid (HCl), formic acid (HCOOH), sulfuric acid (H_2SO_4), ammonia solution ($NH_3·H_2O$) and hydroxylamine-hydrochloride ($NH_2OH·HCl$) were purchased from Hangzhou Mike Chemical Agents Co. Ltd., China. All the chemical reagents and materials were in used as-received without further purification, and the water used in experimental procedures was deionized water (Millipore Milli-Q purification system).

2.2. Preparation of DACN

It is well known that the $NaIO_4$ oxidation can selectively convert hydroxyl groups on the cellulose into aldehyde groups and formed CNs by oxidative cleavage between at C_2 and C_3 bonds of the glucose repeat units. The yield and the aldehyde content of DACN are considered as the important criteria to judge the effectiveness of this method. Thus, a novel double response surface models and an orthogonal experiment with four factors and three levels (L_{16} $(3)^4$ array) were carried out to optimize the preparation for DACN. In detail, the DACN was fabricated by $NaIO_4$ oxidation under different conditions (solid-liquid ratio range of 1:25-1:100 [g/mL], $NaIO_4$ solution concentration of 0.1–0.5 M, time of 0.5–1.5 h, and temperature of 30–60 °C, shown in Table 1). The detailed process was as follows: 1 g of MCC was put into $NaIO_4$ solution in 100 mL flask with continuous stirring. After desired reaction time, the product was collected by centrifugation and freeze-dried for 48 h.

Table 1. The factorial experiments of solid-liquid ratio, $NaIO_4$ concentration, reaction time and temperature (A: solid-liquid ratio; B: $NaIO_4$ concentration; C: reaction time; D: temperature; Y: yield; ADC: aldehyde group content; DO: degree of oxidation; X_c: crystallinity)

Sample NO.	A [g/mL]	B [M]	C [h]	D [°C]	Y [%]	ADC [mmol/g]	DO	X_c [%]
1	1:100	0.1	0.5	30	93.2	0.5	0.04	72
2	1:100	0.25	1	45	74.3	3.2	0.26	81
3	1:100	0.5	1.5	60	68.4	9.8	0.80	79
4	1:50	0.1	1	60	84.1	3.0	0.24	80
5	1:50	0.25	1.5	30	78.4	1.6	0.13	72
6	1:50	0.5	0.5	45	97.7	3.8	0.31	60
7	1:25	0.1	1.5	45	86.0	1.2	0.10	67
8	1:25	0.25	0.5	60	90.8	0.7	0.06	74
9	1:25	0.5	1	30	91.5	2.5	0.20	72

For comparison, cellulose nanocrystals were prepared by acid hydrolysis from MCC using 64 wt% H_2SO_4 (CN-S) and HCl/HCOOH mixture (CN-M), respectively, as previously reported [1, 2, 7].

2.3. Determination of the aldehyde group content and degree of oxidation

The aldehyde content was determined by pH titration of forming HCl obtained from oxime reaction between the $NH_2OH{\cdot}HCl$ and aldehyde groups of DACN [21]. Firstly, 0.01 M HCl was added to 20 mL $NH_2OH{\cdot}HCl$ solution (0.3 M), and a pH meter was used to monitor the pH of the solution simultaneously, then a curve for pH vs. HCl volume (V_{HCl}) was plotted. Next, dried samples (approx. 0.1 g) were added to the same solution which was described above, and the mixture was sufficiently stirred for 24 h at the room temperature, then the pH of the mixture was measured by the pH meter at the room temperature. Finally, the V_{HCl} [mL] of the reaction was determined from the pH vs. V_{HCl} curve, and the aldehyde group content of the sample [mmol/g] was calculated as shown in Equation (1):

$$[\mathrm{CHO}] = V_{\mathrm{HCl}} \cdot \frac{c_{\mathrm{HCl}}}{m_0} \qquad (1)$$

where [CHO] is the aldehyde content [mmol/g], V_{HCl} is the HCl volume, c_{HCl} is the concentration of the HCl aqueous solution, m_0 is the mass of dried DACNs [g]. The degree of oxidation (DO) of DACNs refers to the average number of hydroxyls oxidized by $NaIO_4$ on the anhydrous glucose unit (AGU) and was determined by Equation (2):

$$\mathrm{DO} = \frac{\dfrac{[\mathrm{CHO}]}{2 \cdot m_0}}{162} \qquad (2)$$

where DO is the degree of oxidation, m_0 is the mass of dried DACNs [g], 162 is the molar mass [g/mol] of AGU, and the value of 2 is the theoretical DO value.

2.4. Preparation of CN-Ag nanoparticles

The synthesized procedures of CN-Ag nanohybrids were according to the previously described method [1, 2]. In general, the aqueous solution of silver ammonia (silver ammonia aqueous solution was prepared by adding 1 mL of 25% ammonia to 100 mL $AgNO_3$ (0.85 g) solution. The final stage of ammonia addition was performed dropwise to give a clear solution [1, 2, 22]) was mixed with the CNs suspensions (approx. 1.0 g dry sample), and then heated to 90 °C for about 20 min. After cooling to the room temperature, the precipitates were washed with deionized water by successive centrifugation to remove the residual silver ammonia and the reaction byproducts. Moreover, the CN-M with formate esters, RDACN and SDACN with aldehyde groups were selected to synthesize CN-Ag nanohybrids. The samples were dried and denoted as CN-M-Ag-0.85, SDACN-Ag-0.85 and RDACN-Ag-0.85, respectively, and the FE-SEM photos were shown below (Figures 7a, 7b and 7c).

2.5. Characterization

The morphologies of the CNs were observed using field-emission scanning electron microscopy (FE-SEM, JSM-5610; JEOL, Japan) at an acceleration voltage of 1.0 kV at room temperature. Chemical structure of samples was measured on a Nicolet 5700 Fourier transform infrared (FT-IR) spectra and the crystal structure was performed on an X-ray powder diffractometer (XRD, ARL X'RA; Thermo Electron Corp.). The thermal stability test was conducted on samples by using a thermogravimetric analyzer (TGA, Pyris Diamond I; PerkinElmer Corp.) under a nitrogen atmosphere with a heating rate of 20 °C/min from room temperature to 600 °C. Particle size of aqueous CN suspension was tested by the Nano ZS Malvern Zetasizer. *E. coli* as the model Gram-negative bacteria and *S. aureus* as the model Gram-positive bacteria were chosen to investigate the antimicrobial activities of CN-M-Ag-0.85, SDACN-Ag-0.85 and RDACN-Ag-0.85 nanohybrids as reported in previous literatures [1, 2, 20].

3. Results and discussion

3.1. Model fitting and optimization

The orthogonal experiment ($L_{16}\,(3)^4$ array) was carried out with four factors (Table 1), 'A', 'B', 'C', and 'D' stand for the solid-liquid ratio, $NaIO_4$ concentration, reaction time and temperature, respectively. From range analysis results of Table 2 and Table 3, it is found that the influencing order of the factors on the yield is C>D>A>B, while that on the aldehyde content is B>A>D>C. It suggests that the reaction time plays an important role in the yield of DACN, while $NaIO_4$ concentration has a significant effect on the formation of aldehyde groups. According to the results of the factorial experiments, the optimal combination $A_3B_2C_2D_2$ was obtained for maximum yields of 97.7% (the DACN with rod-like shape (see below in Figure 3c) in this condition was denoted as RDACN). Similarly, the optimal combination $A_1B_3C_3D_3$ was the oxidization conditions for the highest content of aldehyde groups of 9.8 mmol/g with the highest DO value (about 0.8) (the DACN with spherical shape (see below in Figure 3b) in this condition was denoted as SDACN). However, when the $NaIO_4$ concentration was increased (over 0.5 M), the obtained product was becoming completely amorphous (without crystalline region), the XRD spectrum was shown in Figure 4c, which was similar to previous work [23]. In addition, in order to confirm the complete conversion of DACN, the sample 1 (shortest reaction time of 0.5 h, lowest aldehyde content of 0.5 mmol/g) was tested in Figure 3d. The results of FE-SEM image and particle size distribution indicated the nanoscale sizes of DACN were achieved even under a short reaction time (0.5 h).

Table 2. Analyses of the factorial experiments for yields [%] (A: solid-liquid ratio; B: $NaIO_4$ concentration; C: reaction time; D: temperature)

	A **[g/mL]**	**B** **[M]**	**C** **[h]**	**D** **[°C]**
K_1	78.7	81.5	87.7	81.4
K_2	86.7	87.5	89.6	92.3
K_3	89.4	85.9	77.6	81.1
R	10.7	6.0	12.0	11.2

Priority factor C>D>A>B
Optimal combination $A_3B_2C_2D_2$
K = (∑ yield after oxidation of single-factor)/3.
R = $K_{max} - K_{min}$.

Table 3. Analyses of the factorial experiments for aldehyde group contents [mmol/g] (A: solid-liquid ratio; B: $NaIO_4$ concentration; C: reaction time; D: temperature)

	A **[g/mL]**	**B** **[M]**	**C** **[h]**	**D** **[°C]**
K_1	10.3	1.6	1.7	1.6
K_2	2.8	1.9	2.9	2.8
K_3	1.5	11.2	10.1	10.3
R	8.8	9.6	8.4	8.7

Priority factor B>A>D>C
Optimal combination $A_1B_3C_3D_3$
K = (∑aldehyde content after oxidation of single-factor)/3.
R = $K_{max} - K_{min}$.

The mathematical model representing the yield and aldehyde content of DACN against the function of the independent variables within the range under investigation is expressed Equations (3) and (4):

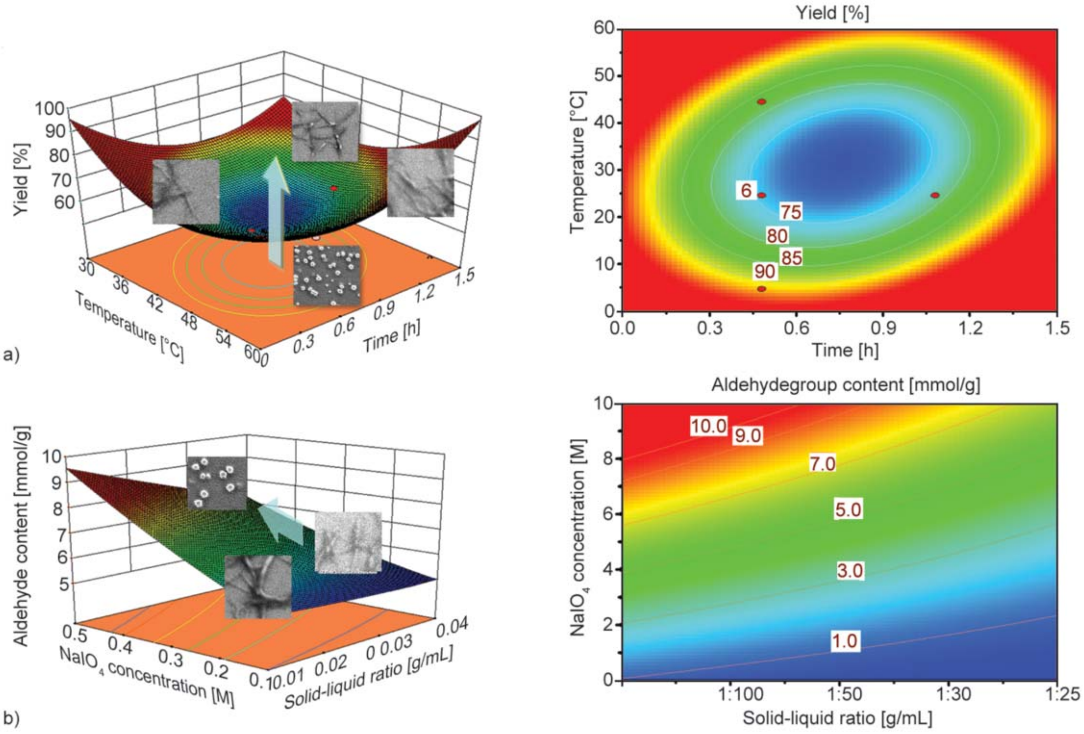

Figure 1. Response surface plots for maximum yield and aldehyde content of DACN: effects of temperature and reaction time on the yield [%] (a), effects of $NaIO_4$ concentration and solid-liquid ratio on the aldehyde content [mmol/g] of DACN (b)

$$\begin{aligned}Y_1 = {} & 135.81 - 12.97X_1 - 0.88X_2 - 41.20X_3 - \\ & - 1.30X_4 - 8.88\cdot10^{-13}X_1X_2 + 3.70\cdot10^{-14}X_1X_3 + \\ & + 2.46\cdot10^{-1}X_1X_4 - 2.22\cdot10^{-14}X_2X_3 - \\ & - 8.88\cdot10^{-16}X_2X_4 - 0.25X_3X_4 + 259.30{X_1}^2 + \\ & + 1.46{X_2}^2 + 18.93{X_3}^2 + 0.02{X_4}^2 \end{aligned} \qquad (3)$$

$$\begin{aligned}Y_2 = {} & 2.80 + 40.15X_1 + 17.60X_2 - 3.67X_3 - 0.18X_4 - \\ & - 666.67X_1X_2 - 1.48\cdot10^{-14}X_1X_3 - \\ & - 2.96\cdot10^{-15}X_1X_4 - 1.27\cdot10^{-1}X_2X_3 - \\ & - 2.83\cdot10^{-16}X_2X_4 - 4.44\cdot10^{-17}X_3X_4 + \\ & + 1648.15{X_1}^2 + 14.90{X_2}^2 + 1.83{X_3}^2 + \\ & + 2.04\cdot10^{-3}{X_4}^2 \end{aligned} \qquad (4)$$

where Y_1 and Y_2 are the yield and aldehyde content of DACN, whereas X_1, X_2, X_3 and X_4 are the coded variables for solid-liquid ratio, $NaIO_4$ concentration, reaction time and temperature, respectively. In general, poor or misleading results may be produced by the exploration and optimization of a fitted response surface unless the model exhibited good fitness [24, 25]. Since the P-value of the model was less than 0.0001, the model's fitness was good. The effects of the variables on the yield and aldehyde content of DACN are shown in Figure 1. Based on the prediction of the computing program and taking the practical operating condition into consideration, the optimal conditions to obtain the highest yields are solid-liquid ratio of 1: 50, $NaIO_4$ concentration of 0.5 M, reaction time of 0.5 h, and temperature of 45 °C, while the optimal conditions to obtain the highest aldehyde contents are solid-liquid ratio of 1:100, $NaIO_4$ concentration of 0.5 M, reaction time of 1.5 h and temperature of 60 °C. Thus, the experimental conditions should be chosen moderately according to the double response surface model, and the RDACN and SDACN could be obtained using this model under controllable conditions.

3.2. Morphology of DACN

In order to observe the morphologies of SDACN and RDACN, their FE-SEM images are clearly shown in Figure 2, in which the morphologies for different kinds of CNs are compared. MCC displayed rubby-shaped fragments with particle size of 15–30 µm (Figure 2a). The CN-M (Figure 2b) and CN-S (Figure 3a) both exhibited rod-like shape with average

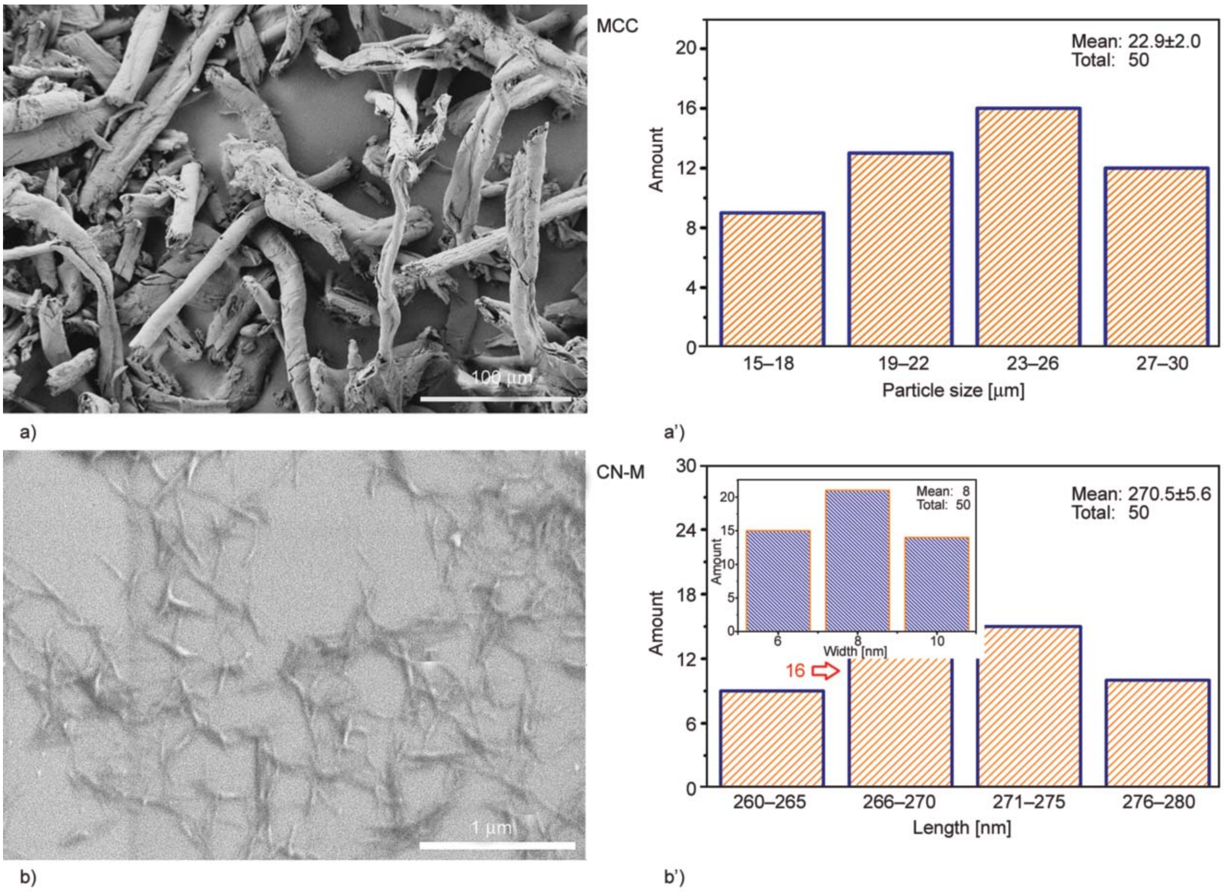

Figure 2. FE-SEM images of MCC (a), CN-M (b), rod-like DACN and the particle size distribution (a', b')

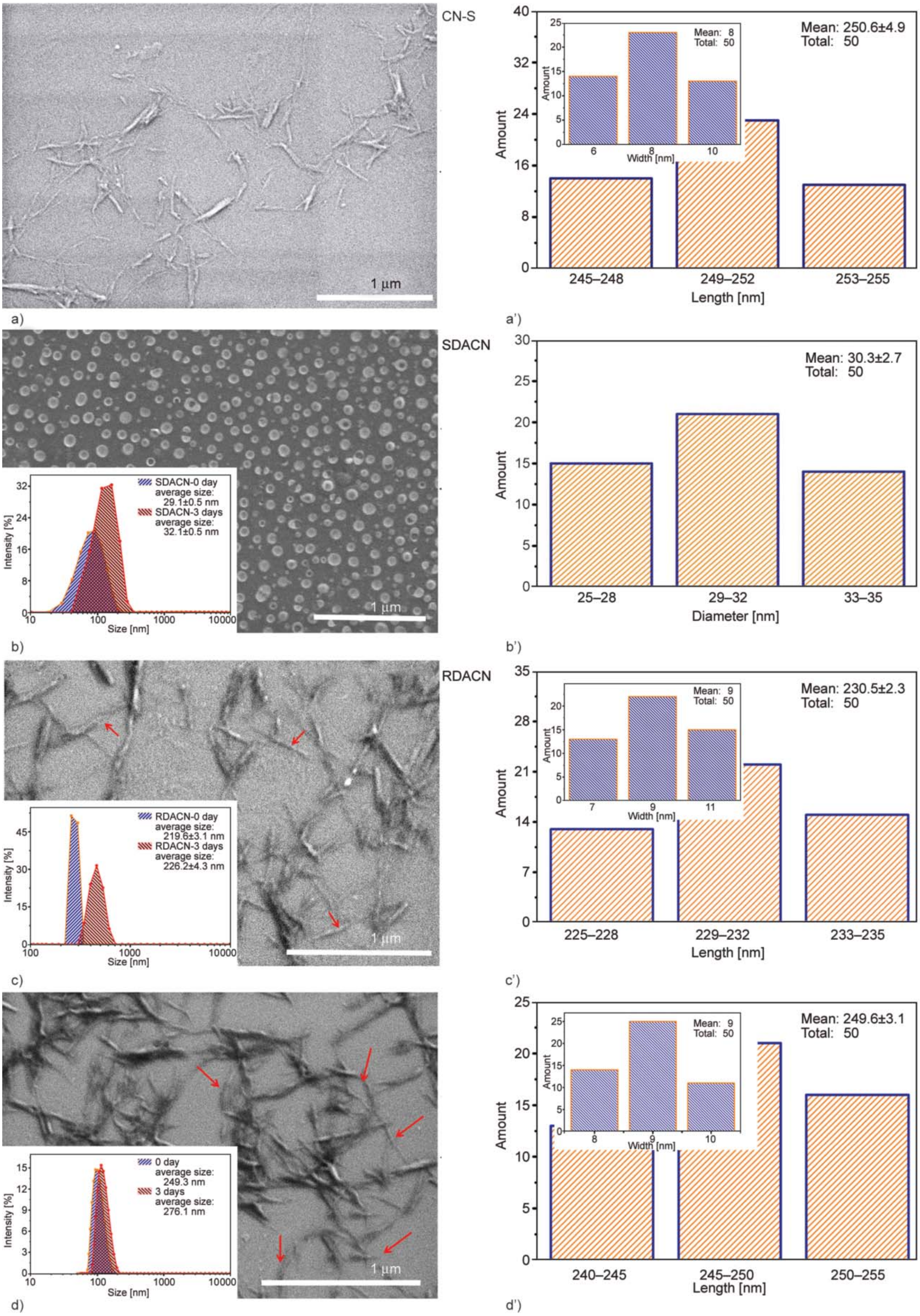

Figure 3. FE-SEM images of CN-S (a), RDACN (b), SDACN (c), rod-like DACN (d) and the particle size distribution (a', b', c', d')

length of 270.5±5.6, 250.6±4.9 nm, respectively, while the width for both samples was about 8 nm. The similar dimension agreed well with previously reported work [7]. In particular, a good dispersion of CN-S was found due to electrostatic repulsion of sulfate groups after the hydrolysis of sulfuric acid. In Figure 3b, SDACN showed spherical nanoparticles with a diameter of 25–35 nm, while RDACN showed rod-like shape with average length of 230.5±2.3 nm and width of 9 nm, respectively (Figure 3c). Furthermore, the particle sizes (freshly dispersed and kept in the room temperature for 3 days) of SDACN (insert in Figure 3b) and RDACN (insert in Figure 3c) were tested by the Nano ZS Malvern Zetasizer, and the results indicated the nanoscale size of SDACN and RDACN were obtained. Thus, the above mentioned results indicated that with the help of the oxidizing agent ($NaIO_4$), rod-like or spherical DACN can be regioselectively prepared by modulating the degree of oxidation. The $NaIO_4$ oxidation as acid-free method showed great potential to prepare the CNs, which can replace common acid-hydrolyzed approach.

3.3. Chemical structure of DACN

FT-IR measurement was performed to determine the variation of surface chemical groups of different kinds of CN samples, and the FT-IR spectra are shown in Figure 4a. Some characteristic peaks of cellulose at 3414, 2909, 1639, 1032–1056 and 895 cm^{-1} were assigned to O–H, symmetric C–H, absorbed moisture, C–O–C stretching vibration and β-glycosilic linkages between the sugar units, respectively [14, 18, 26, 27]. For CN-S, a unique absorption band at 1205 cm^{-1} corresponded to S=O stretching from sulfate groups was observed [7]. Because of the esterification reaction between hydroxyl groups on the surface of commercial MCC and HCOOH, an obvious carbonyl (C=O) peak at 1719 cm^{-1} was found for CN-M due to its surface formate groups (each formate group contained an aldehyde structure) [2, 20], while the DACN samples show new C=O peak at 1725 cm^{-1} assigned to their aldehyde groups. Further, compared to CN-M, the DACN exhibited higher normalized intensity of C=O peak, indicating more aldehyde groups were introduced into DACNs by $NaIO_4$ oxidation than mixed acid hydrolysis. Similar

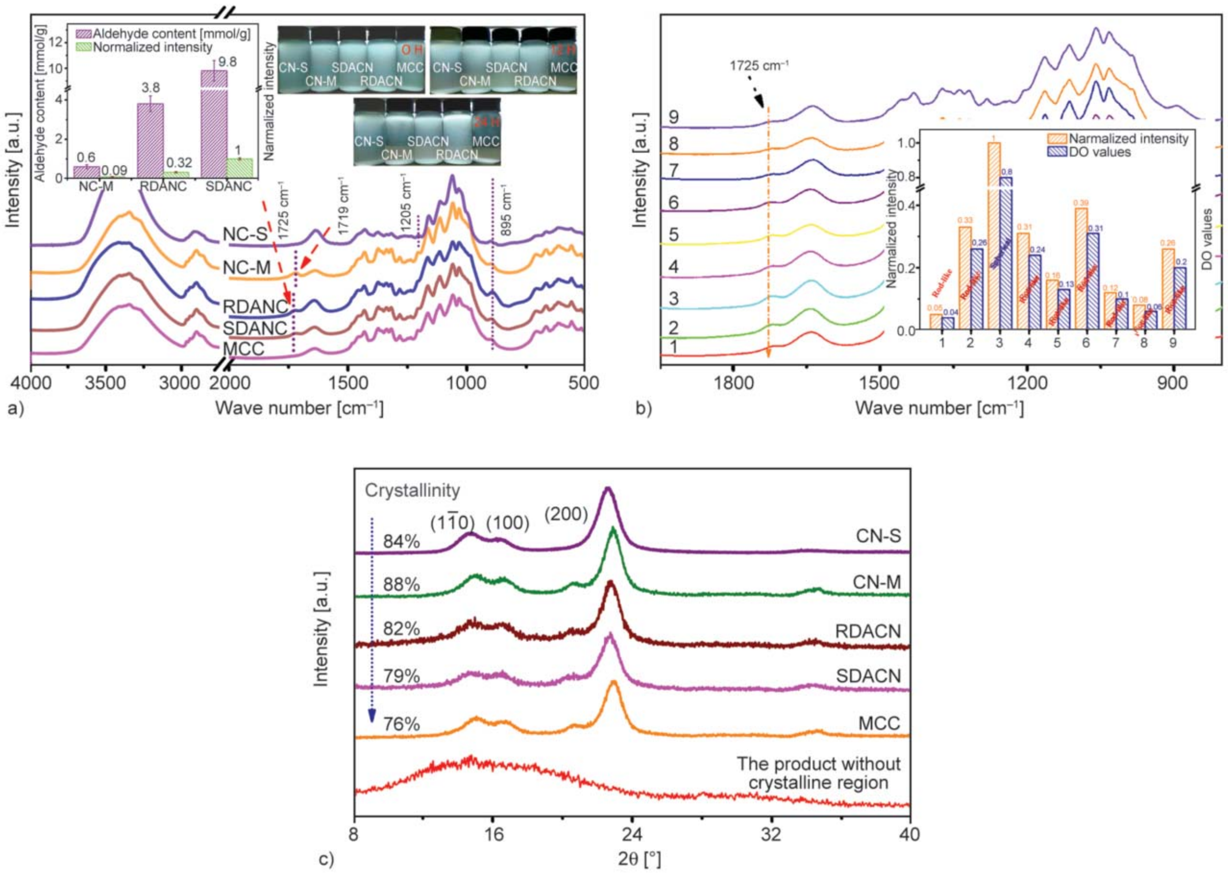

Figure 4. FT-IR spectra (normalization intensity of carbonyl peak at 1719 and 1725 cm^{-1}) of CNs and MCC (a), FT-IR spectra (b) of nine orthogonal experiment groups (c), and XRD patterns of CNs and MCC

phenomenon was observed in $NaIO_4$ oxidation of CNs (natural cellulose fibers) [14]. When the skeleton band of cellulose at 800–900 cm^{-1} was fixed, normalization intensity of aldehyde C=O peak for DACNs can be used to qualitatively comparison analysis. Moreover, the SDACN showed the higher normalized intensity for C=O peak than that of RDACN, suggesting that spherical nanoparticles with high specific surface area were more susceptible to be attacked by $NaIO_4$, leading to the formation of more aldehyde groups. Meanwhile, the FT-IR spectra, normalized intensity for C=O peak at 1725 cm^{-1} and corresponding OD values of DACNs (9 samples from orthogonal experiment groups) prepared by $NaIO_4$ oxidation were shown in Figure 4b. The results of normalized intensity for C=O peak for CNs can support above results. Additionally, the DACNs prepared by $NaIO_4$ oxidation exhibited as good suspension stability as CN-M and CN-S samples (insert in Figure 4a).

3.4. Crystal structure and crystallinity of DACN

The XRD spectra for MCC and CN samples were presented in Figure 4c. MCC and the other CNs possessed typical peaks of cellulose I with main peaks at 2θ = 14.5, 16.5, and 22.6°, which assigned to the crystalline planes of $(1\bar{1}0)$, (110) and (200), respectively [1, 2, 14, 18]. By using Segal's method [28], the crystallinity of MCC, CN-S and CN-M were 76, 84 and 88%, respectively. Compared to CN-S and CN-M, a slight reduction in crystallinity (82%) was found for RDACN and SDACN (79%). The results showed that all CNs have higher crystallinity than MCC, which indicating that parts of MCC residual amorphous phase have been dissolved by various treatments (mixed acid (HCl/HCOOH), sulfuric acid, $NaIO_4$ oxidation). For acid hydrolysis, the fabricating process for CNs was aimed at breaking the β-1, 4-glycosidic bonds on the amorphous region of MCC, while the oxidation process would open glucopyranose chains in crystalline or amorphous regions and increase the solubility (Figure 5), which resulting in lower degree of crystallinity than acid hydrolysis process. The decreased crystallinity was ascribed to the higher opened glucopyranose rings (higher DO values) and the higher destruction of ordered CNs structure, under violent condition of $NaIO_4$ oxidation, and the nanocrystals with the selective orientation causing a reduction in diffraction peak intensity from some Bragg planes [18]. Generally, the higher the DO value was, the lower the crystallinity was. Moreover, the higher crystallinity of CN-M was attributed to only amorphous regions of cellulose materials attacked by acid hydrolysis and esterification reactions, without opened glucopyranose rings in crystalline regions.

3.5. Thermal stability of DACN

TGA and DTG curves (Figure 6) revealed the thermal stability for MCC and CN samples. Comparing with MCC (onset degradation temperature (T_0) of 325.3 °C), the CN-M owned the higher T_0 of 346.9 °C, the other CNs samples had lower T_0 values. Especially, CN-S showed very low T_0 value of 208.1 °C because of the existence of sulfate groups on cellulose surface [7, 28], while the RDACN and SDACN had higher T_0 value of 281.6 and 222.1 °C, respec-

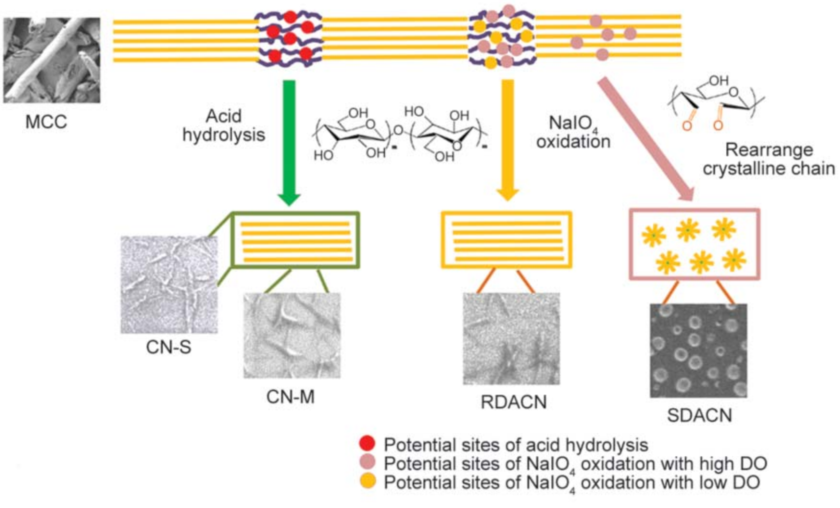

Figure 5. $NaIO_4$ oxidation and acid hydrolysis mechanism schema of CNs

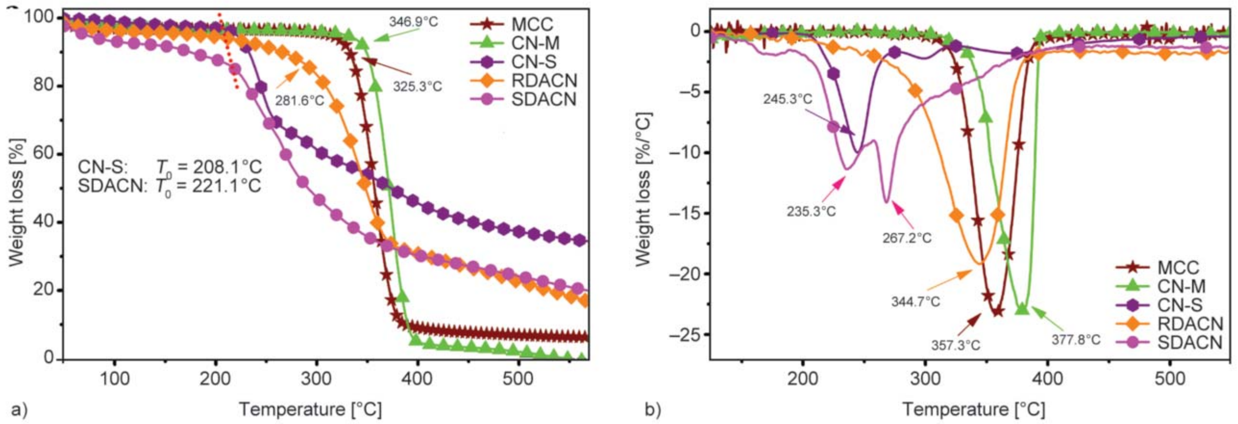

Figure 6. TGA (a) and DTG (b) curve of CN-S, CN-M, RDACN, SDACN and MCC

tively. A similar trend was found for maximum degradation temperature (T_{max}) of the samples. For clear observation, the thermal stability data (T_0, T_{max}, T_f (complete degradation temperature)) were shown in Table 4. In addition, the first derivative of the weight loss curve with respect to temperature (DTG) was shown in Figure 6b. It can be observed that MCC, CN-M and RDACN owned the single step maximum degradation peaks at 357.3, 377.8 and 344.7 °C, respectively. However, CN-S and SDACN started to degrade at lower temperature and exhibited with two main peaks. For CN-S with sulfate groups, the degradation occurred within a wider temperature range and showed three well separated pyrolysis processes: the first one appeared around 196.9–275.0 °C, the second one was around 277.0–324.7 °C, and the other occurred around 325.0–443.9 °C. The multiple degradation peaks exhibited in CN-S curve were attributed to the wide size distribution and the introduction of sulfate groups during sulfuric acid hydrolysis of MCC with possible different sulfonation degrees [7, 28]. On the other hand, SDACN showed two degradation peaks at 235.3 and 267.2 °C. This was due to that the dialdehyde modified SDACNs chains did not form the hemiacetal linkage during the first (195.5–259.8 °C) degradation process. The second degradation process (259.8–411.4 °C) was ascribed to the degradation of cellulose skeleton for the SDACN. Therefore, the CNs prepared by $NaIO_4$ oxidation had better thermal stability than that for H_2SO_4 hydrolyzed one, but poorer than that of CN-M. In addition, RDACN showed the higher degradation temperature than that of SDACN, probably resulting from low degree of oxidation, surface morphology and crystallinity.

3.6. Properties for CN-Ag nanohybrids

In general, the more aldehyde groups on the CNs surface is beneficial to anchor more metal nanoparticles via redox reaction, thus the SDACN with highest aldehyde content, RDACN and CN-M with low aldehyde content were selected to investigate the morphology and antibacterial activity for resulting CN-Ag nanohybrids. It is found that more Ag nanoparticles (29.6%) with diameter of 30±4 nm on the SDACN-Ag-0.85 are observed, whereas the less Ag nanoparticles with diameter of 33±4 and 35±5 nm were fixed on the RDACN-Ag-0.85 (23.9%) and CN-M-Ag-0.85 (21.6%) surfaces, respectively, shown in Figure 7d. The XRD patterns (Figure 7e) of CN-M-Ag-0.85, RDACN-Ag-0.85 and SDACN-Ag-0.85 showed four diffraction peaks at $2\theta = 38.3$, 44.3, 64.5 and 77.5° assigning to the (111), (200), (220) and (311) planes of cubic Ag nanoparticles [1, 20]. Further, the antibacterial activities for CN-Ag nanohybrids against *S. aureus* and *E. coli* by formation of zone of inhibitions are shown in Figure 7f. All the nanohybrids gave extremely strong activities against both the Gram-positive (*S. aureus*) and Gram-negative (*E. coli*) species. Moreover, the SDACN-Ag-0.85

Table 4. Thermal stability data (T_0, T_{max}, T_f) of MCC, CN-M, CN-S, RDACN and SDACN

	MCC	CN-M	CN-S	RDACN	SDACN
T_0 [°C]	325.3	346.9	208.1	281.6	222.1
T_{max} [°C]	357.3	377.8	245.3/294.1/374.6	344.7	235.3/267.2
T_f [°C]	373.4	390.3	363.9	367.1	341.5

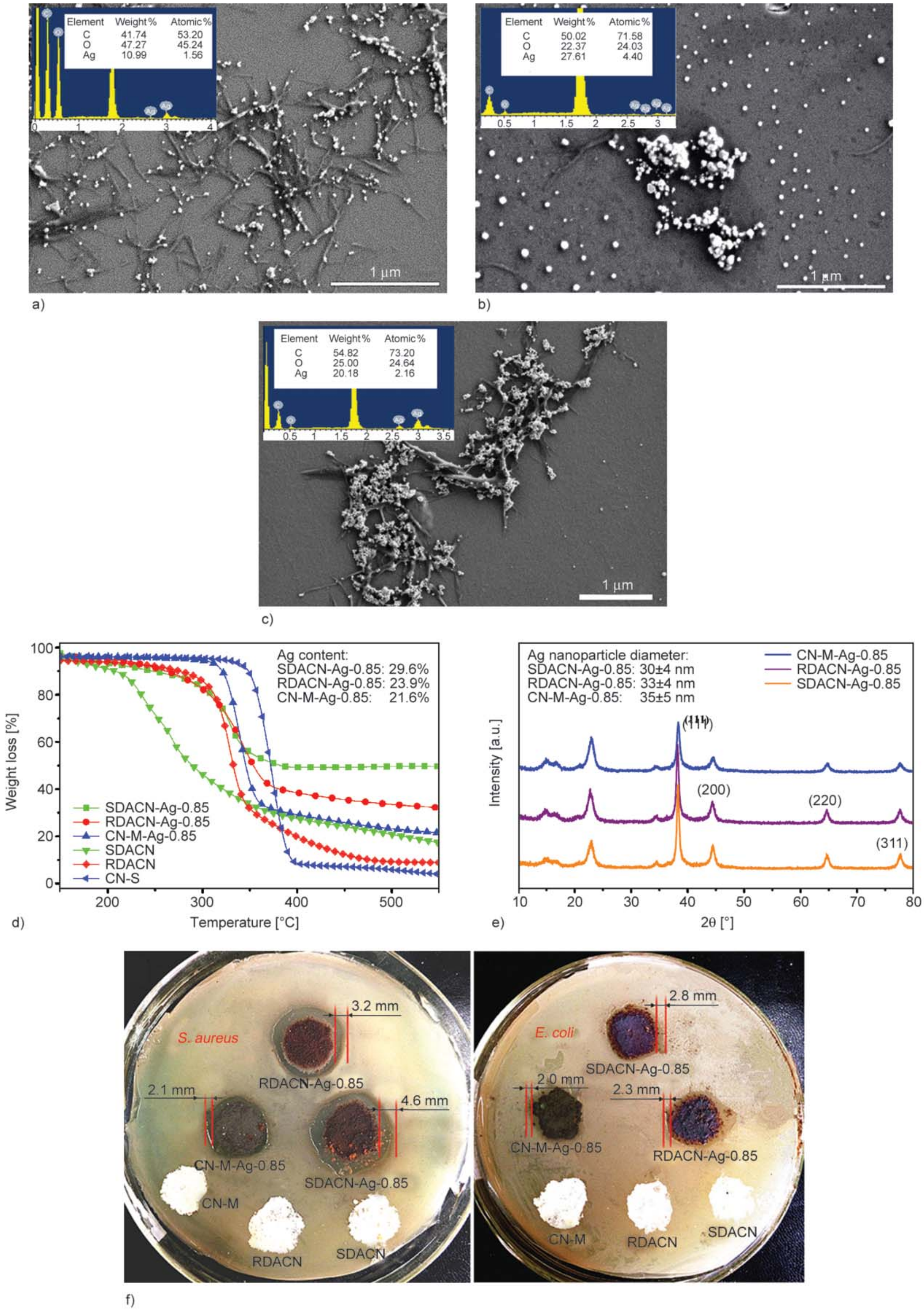

Figure 7. FE-SEM images of CN-M-Ag-0.85 (a), SDACN-Ag-0.85 (b), RDACN-Ag-0.85 nanohybrids (c) and their TGA curves (d), XRD patterns (e), antibacterial abilities against *S. aureus* and *E. coli* (f)

presented the largest inhibition zone against *S. aureus* and *E. coli* (4.6 and 2.8 mm) than RDACN-Ag-0.85 (3.2 and 2.3 mm) and CN-M-Ag-0.85 (2.1 and 2.0 mm), suggesting that the large amount of aldehyde groups on SDACN reduced more Ag^+ into Ag^0 nanoparticles, leading to the high antibacterial activity [1, 2, 20].

4. Conclusions

Spherical and rod-like DACN can be optimized and regioselectively extracted from MCC via one-step $NaIO_4$ oxidation using a novel double response surface model. Both SDACN with the high aldehyde content of 9.8 mmol/g and RDACN with relatively low aldehyde content of 3.8 mmol/g possessed cellulose I crystal structure. Moreover, RDACN and SDACN showed the better thermal stability than CN-S (H_2SO_4 hydrolysis), but lower than CN-M (hydrochloric/formic hydrolysis) due to less destruction of the ordered cellulose structure. In addition, SDACN can act as the reductant for anchoring more Ag nanoparticles, and thus the resultant SDACN-Ag-0.85 nanohybrids demonstrated the highest antibacterial activity against both Gram-negative *E. coil* and Gram-positive *S. aureus*. Thus, one-step $NaIO_4$ oxidation in this study as acid-free route showed more advantages than acid hydrolysis methods, and the DACN may have potential applications in functional papers, sensors, and bioimaging for large-scale production of cellulose-based nanocomposites.

Acknowledgements

The work was financially supported by the National Natural Science Foundation of China (51403187), the public technology research plan of Zhejiang Province, China under Grant No. 2015C33111, and '521' Talent Project of Zhejiang Sci-Tech University and Open fund in Top Priority Discipline of Zhejiang Province in Zhejiang Sci-Tech University (2015YXQN04, 2016YXQN07, 2015YXQN11).

References

[1] Yu H., Sun B., Zhang D., Chen G., Yang X., Yao J.: Reinforcement of biodegradable poly(3-hydroxybutyrate-*co*-3-hydroxyvalerate) with cellulose nanocrystal/silver nanohybrids as bifunctional nanofillers. Journal of Materials Chemistry B, **2**, 8479–8489 (2014).
DOI: 10.1039/C4TB01372G

[2] Yu H-Y., Qin Z-Y., Sun B., Yan C. F., Yao J-M.: One-pot green fabrication and antibacterial activity of thermally stable corn-like CNC/Ag nanocomposites. Journal of Nanoparticle Research, **16**, 2202/1–2202/12 (2014).
DOI: 10.1007/s11051-013-2202-4

[3] Padalkar S., Capadona J. R., Rowan S. J., Weder C., Moon R. J., Stanciu L. A.: Self-assembly and alignment of semiconductor nanoparticles on cellulose nanocrystals. Journal of Materials Science, **46**, 5672–5679 (2011).
DOI: 10.1007/s10853-011-5518-4

[4] Yang X., Cranston E. D.: Chemically cross-linked cellulose nanocrystal aerogels with shape recovery and superabsorbent properties. Chemistry of Materials, **26**, 6016–6025 (2014).
DOI: 10.1021/cm502873c

[5] Wang H. R., He J. L., Zhang M. Z., Tam K. C., Ni P. H.: A new pathway towards polymer modified cellulose nanocrystals *via* a 'grafting onto' process for drug delivery. Polymer Chemistry, **6**, 4206–4209 (2015).
DOI: 10.1039/C5PY00466G

[6] Cao S-L., Li X-H., Lou W-Y., Zong M-H.: Preparation of a novel magnetic cellulose nanocrystal and its efficient use for enzyme immobilization. Journal of Materials Chemistry B, **2**, 5522–5530 (2014).
DOI: 10.1039/C4TB00584H

[7] Yu H., Qin Z., Liang B., Liu N., Zhou Z., Chen L.: Facile extraction of thermally stable cellulose nanocrystals with a high yield of 93% through hydrochloric acid hydrolysis under hydrothermal conditions. Journal of Materials Chemistry A, **1**, 3938–3944 (2013).
DOI: 10.1039/C3TA01150J

[8] Satyamurthy P., Vigneshwaran N.: A novel process for synthesis of spherical nanocellulose by controlled hydrolysis of microcrystalline cellulose using anaerobic microbial consortium. Enzyme and Microbial Technology, **52**, 20–25 (2013).
DOI: 10.1016/j.enzmictec.2012.09.002

[9] Li M-C., Wu Q., Song K., Qing Y., Wu Y.: Cellulose nanoparticles as modifiers for rheology and fluid loss in bentonite water-based fluids. ACS Applied Materials and Interfaces, **7**, 5006–5016 (2015).
DOI: 10.1021/acsami.5b00498

[10] Montanari S., Roumani M., Heux L., Vignon M. R.: Topochemistry of carboxylated cellulose nanocrystals resulting from TEMPO-mediated oxidation. Macromolecules, **38**, 1665–1671 (2005).
DOI: 10.1021/ma048396c

[11] Paralikar S. A., Simonsen J., Lombardi J.: Poly(vinyl alcohol)/cellulose nanocrystal barrier membranes. Journal of Membrane Science, **320**, 248–258 (2008).
DOI: 10.1016/j.memsci.2008.04.009

[12] Cheng M., Qin Z. Y., Liu Y., Qin Y., Li T., Chen L., Zhu M.: Efficient extraction of carboxylated spherical cellulose nanocrystals with narrow distribution through hydrolysis of lyocell fibers by using ammonium persulfate as an oxidant. Journal of Materials Chemistry A, **2**, 251–258 (2014).
DOI: 10.1039/C3TA13653A

[13] Dash R., Ragauskas A. J.: Synthesis of a novel cellulose nanowhisker-based drug delivery system. RSC Advances, **2**, 3403–3409 (2012).
DOI: 10.1039/C2RA01071B

[14] Sun B., Hou Q., Liu Z., Ni Y.: Sodium periodate oxidation of cellulose nanocrystal and its application as a paper wet strength additive. Cellulose, **22**, 1135–1146 (2015).
DOI: 10.1007/s10570-015-0575-5

[15] Huang R., Liu Z., Sun B., Fatehi P.: Preparation of dialdehyde cellulose nanocrystal as an adsorbent for creatinine. The Canadian Journal of Chemical Engineering, **94**, 1435–1441 (2016).
DOI: 10.1002/cjce.22523

[16] Yang H., Chen D., van de Ven T. G. M.: Preparation and characterization of sterically stabilized nanocrystalline cellulose obtained by periodate oxidation of cellulose fibers. Cellulose, **22**, 1743–1752 (2015).
DOI: 10.1007/s10570-015-0584-4

[17] Yang H., Tejado A., Alam N., Antal M., van de Ven T. G. M.: Films prepared from electrosterically stabilized nanocrystalline cellulose. Langmuir, **28**, 7834–7842 (2012).
DOI: 10.1021/la2049663

[18] Yang H., Alam M. N., van de Ven T. G. M.: Highly charged nanocrystalline cellulose and dicarboxylated cellulose from periodate and chlorite oxidized cellulose fibers. Cellulose, **20**, 1865–1875 (2013).
DOI: 10.1007/s10570-013-9966-7

[19] Grate J. W., Mo K-F., Shin Y., Vasdekis A., Warner M. G., Kelly R. T., Orr G., Hu D., Dehoff K. J., Brockman F. J., Wilkins M. J.: Alexa fluor-labeled fluorescent cellulose nanocrystals for bioimaging solid cellulose in spatially structured microenvironments. Bioconjugate Chemistry, **26**, 593–601 (2015).
DOI: 10.1021/acs.bioconjchem.5b00048

[20] Drogat N., Granet R., Sol V., Memmi A., Saad N., Koerkamp C. K., Bressollier P., Krausz P.: Antimicrobial silver nanoparticles generated on cellulose nanocrystals. Journal of Nanoparticle Research, **13**, 1557–1562 (2011).
DOI: 10.1007/s11051-010-9995-1

[21] Kim U-J., Wada M., Kuga S.: Solubilization of dialdehyde cellulose by hot water. Carbohydrate Polymers, **56**, 7–10 (2004).
DOI: 10.1016/j.carbpol.2003.10.013

[22] Wu M., Kuga S., Huang Y.: Quasi-one-dimensional arrangement of silver nanoparticles templated by cellulose microfibrils. Langmuir, **24**, 10494–10497 (2008).
DOI: 10.1021/la801602k

[23] Kim U-J., Kuga S., Wada M., Okano T., Kondo T.: Periodate oxidation of crystalline cellulose. Biomacromolecules, **1**, 488–492 (2000).
DOI: 10.1021/bm0000337

[24] Tang L-R., Huang B., Ou W., Chen X-R., Chen Y-D.: Manufacture of cellulose nanocrystals by cation exchange resin-catalyzed hydrolysis of cellulose. Bioresource Technology, **102**, 10973–10977 (2011).
DOI: 10.1016/j.biortech.2011.09.070

[25] Sun B., Yu H-Y., Zhou Y., Huang Z., Yao J-M.: Single-step extraction of functionalized cellulose nanocrystal and polyvinyl chloride from industrial wallpaper wastes. Industrial Crops and Products, **89**, 66–77 (2016).
DOI: 10.1016/j.indcrop.2016.04.040

[26] Visanko M., Liimatainen H., Sirviö J. A., Heiskanen J. P., Niinimäki J., Hormi O.: Amphiphilic cellulose nanocrystals from acid-free oxidative treatment: Physicochemical characteristics and use as an oil–water stabilizer. Biomacromolecules, **15**, 2769–2775 (2014).
DOI: 10.1021/bm500628g

[27] Keshk S. M. A. S.: Homogenous reactions of cellulose from different natural sources. Carbohydrate Polymers, **74**, 942–945 (2008).
DOI: 10.1016/j.carbpol.2008.05.022

[28] Kargarzadeh H., Ahmad I., Abdullah I., Dufresne A., Zainudin S. Y., Sheltami R. M.: Effects of hydrolysis conditions on the morphology, crystallinity, and thermal stability of cellulose nanocrystals extracted from kenaf bast fibers. Cellulose, **19**, 855–866 (2012).
DOI: 10.1007/s10570-012-9684-6

eXPRESS Polymer Letters Vol.10, No.12 (2016) 977–989
Available online at www.expresspolymlett.com
DOI: 10.3144/expresspolymlett.2016.91

Mechanical behaviour of cyclic olefin copolymer/exfoliated graphite nanoplatelets nanocomposites foamed by supercritical carbon dioxide

A. Biani[1], *A. Dorigato*[1], *W. Bonani*[1,2], *M. Slouf*[3], *A. Pegoretti*[1*]

[1]Department of Industrial Engineering and INSTM Research Unit, University of Trento, via Sommarive 9, 38123 Trento, Italy
[2]Department of Industrial Engineering and BIOtech Research Centre, University of Trento, via delle Regole 101, 38123 Trento, Italy
[3]Institute of Macromolecular Chemistry, Academy of Sciences of the Czech Republic, Heyrovsky sq. 2, 16206 Prague 6, Czech Republic

Received 19 April 2016; accepted in revised form 3 July 2016

Abstract. A cycloolefin copolymer matrix was melt mixed with exfoliated graphite nanoplatelets (xGnP) and the resulting nanocomposites were foamed by supercritical carbon dioxide. The density of the obtained foams decreased with the foaming pressure. Moreover, xGnP limited the cell growth during the expansion process thus reducing the cell diameter (from 1.08 to 0.22 mm with an XGnP amount of 10 wt% at 150 bar) and increasing the cell density (from 12 to 45 cells/mm^2 with a nanofiller content of 10 wt% at 150 bar). Electron microscopy observations of foams evidenced exfoliation and orientation of the nanoplatelets along the cell walls. Quasi-static compressive tests and tensile creep tests on foams clearly indicated that xGnP improved the modulus (up to a factor of 10 for a xGnP content of 10 wt%) and the creep stability.

Keywords: *nanocomposites, foams, graphite nanoplatelets, thermomechanical properties, creep*

1. Introduction

Polymeric foams are nowadays extensively used in automotive, aerospace, construction and in packaging sectors due to their low density. In fact, a significant reduction in the weight of the components can be reached with polymer foams thus leading to substantial fuel savings in transports with noticeable economic and environmental advantages. Furthermore, a low material density implies natural resources savings, since less material is required for the manufacturing of consumer goods [1]. Due to their elevated thermal insulation power, an important application of polymer foams is represented by insulation of building constructions [2]. From a technological point of view, porous plastics are commonly produced with processing routes involving physical blowing by low boiling hydrocarbons or their halogenated derivatives. Considering that about fifteen billion kilograms of solvents are produced every year worldwide, their usage represents a critical environmental problem because of the noticeable emission of toxic compounds and of polluted waste water production [3]. Therefore, traditional blowing agents (such as pentane, butane, chlorofluoro hydrocarbons) have been withdrawn and replaced by gases like argon, nitrogen and carbon dioxide [1, 4]. Recently, the usage of supercritical fluids (SFCs) has been considered as a valuable path to produce polymer foams [5–13]. SCFs possess physical properties intermediate between those of gases and fluids. In fact, their density is close

---

[*]Corresponding author, e-mail: alessandro.pegoretti@unitn.it

to that of the liquids and their viscosity is similar to that of gases. At the same time they possess a greater diffusion coefficient with respect to liquids [14]. In addition, close to the critical point, small changes in pressure or temperature result in large changes in density. Polymer matrix foaming with supercritical fluids allows avoiding organic solvents and presents several advantages from a chemical, physical and toxicological points of view. Because of its easy processability, cheapness, non-toxicity and non-flammability, carbon dioxide is the most considered among supercritical fluids [15, 16]. The usage of carbon dioxide as a solvent could lead to several advantages from a manufacturing, economical and safety points of view.

In the last years, the synthesis of thermoplastic polymers through metallocene-based catalysis attracted the attention of various research groups [17–20]. Particular interest has been devoted to cycloolefin copolymers (COCs) that are amorphous thermoplastics obtained by the copolymerization of norbornene and ethylene. COCs manifest remarkable properties in terms of stiffness, high chemical resistance, good moisture barrier properties, low moisture absorption, and low density. Therefore, COCs are often applied in the production of transparent products (optical data storage, lenses, and sensors), medical and diagnostic devices, food containers, packaging of drugs etc. Considering that the glass-transition temperature (T_g) of COCs can be tailored by varying the percentage of norbornene [21], various COC grades suitable for specific applications are available on the market. Also polyolefin/COC blends, especially polypropylene/COC blends [22] and polyethylene/COC blends, have been extensively investigated [23].

It is also well known that the incorporation of nanofillers at concentrations of 5–10 wt% into a polymer matrix can significantly affect its mechanical behaviour, dimensional stability, thermal degradation and chemical resistance and also gas and solvents impermeability [24]. Moreover, the typical drawbacks related to the use of traditional inorganic microfillers (i.e. embrittlement, loss of transparency, loss of lightness) [25] can be avoided. Some attention has been also devoted to the investigation of COC-based nanocomposites [18, 26].

In the last years, several papers have been published in the open scientific literature on polymer nanocomposites filled with carbonaceous plate-like nanofillers, such as exfoliated graphite nanoplatelets (xGnP) [27–33]. xGnP nanofiller is constituted by very thin crystalline graphite stacked layers. Due to the honeycomb arrangement of the carbon atoms in the crystal lattice, xGnP is endowed with exceptional properties in terms of stiffness and strength [34] and it can be therefore used to improve the mechanical properties of a wide range of polymeric materials [27, 33]. The avoidance of xGnP agglomeration is an essential condition for xGnP based nanocomposites, because most of the above cited advantages are due to an homogeneous distribution of the nanofiller within the matrix [35, 36]. Moreover, xGnP has been successfully used to improve barrier properties as well as electrical properties of polymeric materials at low percolation threshold [27]. In fact, its graphitic structure makes it an excellent electrical conductor [37].

In the open literature a few papers can be found on the preparation and physical properties of polymer nanocomposites foamed through supercritical carbon dioxide ($scCO_2$) [9, 10]. For instance, Bhattacharya *et al.* [5] studied the effect of the foaming parameters (i.e. saturation pressure and temperature, foaming temperature, foaming time and quench temperature) on the physical properties of polypropylene/clay nanocomposites of the prepared materials. In another work of Strauss and D'Souza [12] on supercritical CO_2 processed polystyrene nanocomposite foams, it was demonstrated how the foaming process affected both the thermal and morphological behaviour of the prepared materials. Chen *et al.* [38] performed an experimental and theoretical investigation of the compressive properties of multi-walled carbon nanotubes (MWNTs)/poly (methyl methacrylate) nanocomposite foams, finding that the addition of MWNTs increased both the Young's modulus and the compressive properties of polymer foams.

Quite surprisingly, only marginal attention has been devoted to xGnP based nanocomposites foamed through supercritical carbon dioxide. The thermal stability of polycarbonate/xGnP nanocomposite foams was studied by Gedler *et al.* [39], while in another work the dependency of the cellular structure of these nanocomposite foams on the processing parameters (i.e. saturation and foaming temperature) was investigated [40]. Antunes *et al.* [41] devoted their attention on the microstructural features and the thermo-mechanical behaviour of polypropylene foams containing xGnP and expanded through $scCO_2$. A similar topic was presented in the paper of Yeh *et al.* [42] about the effect of dispersion method and process variables on the properties of supercritical CO_2 foamed polystyrene/graphite nanocomposite foams. To the best of our knowledge, no papers dealing with the physical properties of COC/exfoliated graphite nanoplatelets foamed through $scCO_2$ can be found in the open literature.

Starting from the above considerations, the objective of the present work is to prepare and characterize COC/xGnP nanocomposites at various filler concentrations and to foam them by $scCO_2$. A comparison between bulk and foamed samples will be then performed, in order to assess the real effectiveness of xGnP nanoparticles in improving the mechanical properties of the foams. A detailed analysis of the influence of the foaming processing parameters on the physical properties of the produced materials will be reported.

2. Experimental part

2.1. Materials

A cycloolefin copolymer (COC) Topas 8007 (melt flow index at 2.16 kg, 190 °C = 2.17 g/10 min, density = 1020 g/dm^3) was supplied by Ticona (Florence, Kentucky, USA) in the form of polymer chips. Exfoliated graphite nanoplatelets xGnP-M-5, (specific surface area of 120 m^2/g, mean diameter of 5 μm and thickness of 6–8 nm [29]) were provided by XG Sciences Inc. (East Lansing, Michigan, USA). Both materials were used as received.

2.2. Samples preparation

2.2.1. Bulk samples preparation

The filler was melt compounded with COC in a Thermo Haake internal mixer operating at 190 °C, applying a rotors speed of 90 rpm. In order to prevent their agglomeration, the nanoparticles were added slowly in the mixer chamber immediately after the complete melting of the COC. The mixing time was set at 15 minutes, enough to promote a complete and homogeneous mixing. This procedure was already reported in our previous paper on COC-fumed silica nanocomposites [18]. In that case, the mixing time was selected after a preliminary characterization of the microstructural properties of the prepared nanocomposites. The resulting materials were then hot pressed at 0.2 kPa for 10 minutes at a temperature of 190 °C in a Carver press, in order to prepare 0.8 mm thick square sheets.

In this study, COC/xGnP bulk nanocomposites were prepared with a filler weight percentage of 1, 2, 5 and 10 wt%. Each sample was designated indicating the matrix, the nanofiller type and its weight concentration. For instance, COC-xGnP-1 denotes the nanocomposite bulk sample with a xGnP content of 1 wt%.

2.2.2. Foaming process

Polymer foams were prepared through a supercritical carbon dioxide treatment at the BIOtech Center of the University of Trento. In Figure 1a, a representation of the $scCO_2$ foaming plant is reported. The equipment is composed by a CO_2 tank, a cryostat, a pump and a reaction chamber. The carbon dioxide with a gas purity higher than 99.5 vol% in liquid/vapor equilibrium state was supplied in a pressure vessel (60 bar at room temperature) by Messer Italia S.r.l. (Padova, Italy).

Foamed samples were prepared starting from bulk rectangular specimens 5 mm wide and 20 mm long. Neat COC copolymer and COC/xGnP bulk nanocomposites at various filler contents were placed within a high-pressure reaction vessel (BR-300, Berghof Products + Instruments, Eningen, Germany), consisting of a stainless steel 316Ti vessel with an internal polytetrafluoroethylene (PTFE) liner. The PTFE cylinder with a capacity of 700 ml had a diameter of 60 mm and a height of 250 mm, with a maximum pressure and temperature services of 200 bar and 260 °C, respectively. The reactor cap was equipped with fluid inlet valve, pressure relief valve and safety valve set at 250 bar. The reactor was also equipped with a submersion thermocouple and a pressure sensor connected to a computer. In order to cool the CO_2 lines and pump head, a cryostatic bath with a temperature of –9 °C (Model M408-BC, MPM Instruments s.r.l., Bernareggio, MB, Italy) was used.

Once the system was sealed, liquid CO_2 was pumped into the reactor and pressurized through a high-performance liquid chromatography (HPLC) pump (Model 426, Alltech, Deerfield, IL, USA) till the supercritical conditions at desired working pressure were reached. The temperature of the reactor was imposed by an electrical heating jacket (BHM 700,

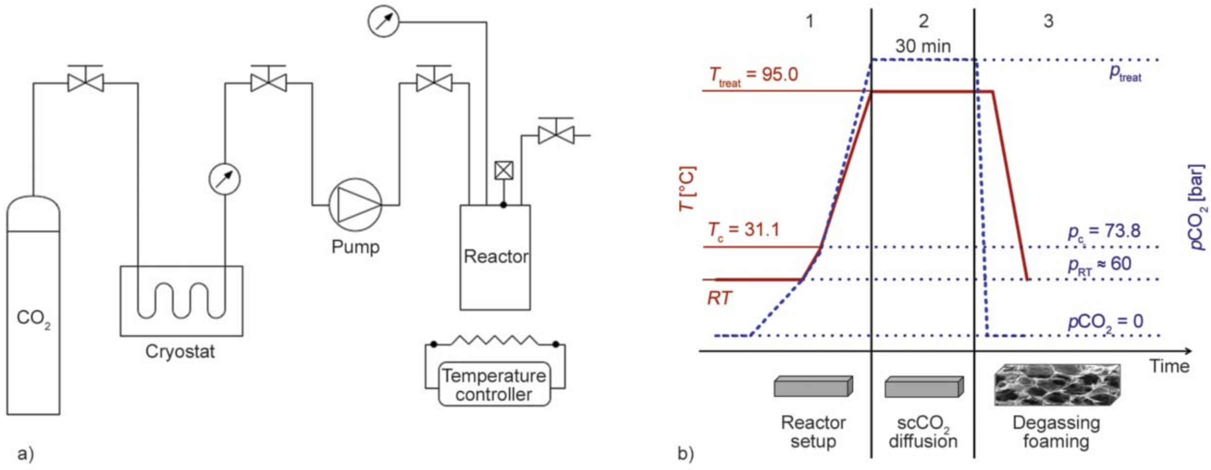

Figure 1. (a) Plant scheme of the foaming process through $scCO_2$, (b) plot of temperature and CO_2 pressure conditions in the reactor chamber during the foaming process: stage (1), setup of the treatment conditions; stage (2), 30 min incubation at constant temperature and pressure in $scCO_2$; stage (3), fast depressurization and consequent foaming of the samples

Berghof) run by a BDL-3000 temperature controller (Berghof). In this study, neat COC copolymer and composite samples were exposed to $scCO_2$ at four different pressures (90, 110, 130 and 150 bar) for 30 min. A constant temperature was set at 95 °C (i.e. about 15 °C higher than COC glass transition temperature). Foaming was obtained upon fast depressurization from supercritical to ambient conditions. It is worthwhile to note that the above parameters were optimized in a previous work of this group regarding the preparation and characterization of COC/fumed silica nanocomposite foams [43].

The plot in Figure 1b outlines the experimental conditions at which the composite materials were subjected during the foaming process in the reactor. During stage (1) bulk composite specimens were introduced into the reactor at *RT* and the inlet valve was open to place the reactor vessel in communication with the pressurized storage vessel. After the reactor reached an equilibrium state (60 bar at *RT*), CO_2 pressure and reactor temperature were progressively increased to establish supercritical conditions (T_c = 31.1 °C, p_c = 73.8 bar) and then to meet the desired treatment conditions (namely, P_{treat} equal to 90, 110, 130 and 150 bar and T_{treat} = 95 °C). During stage (2) composite samples were exposed to $scCO_2$ under constant temperature and pressure for 30 min to allow for supercritical fluid diffusion into the material. Later in stage (3), the outlet valve was open and CO_2 was abruptly released (depressurization rate 50 bar/min) to trigger the foaming of the samples. The structure of the foams was then stabilized with the temperature drop from T_{treat} to ambient conditions.

Foamed samples were designated indicating the matrix, the filler type, the filler content and the foaming pressure. As an example, COC-xGnP-5_e90 indicates

Table 1. List of the prepared samples

Abbreviation	xGnP content [wt%]	Foaming pressure [bar]
COC	–	–
COC-xGnP-1	1	–
COC-xGnP-2	2	–
COC-xGnP-5	5	–
COC-xGnP-10	10	–
COC-xGnP-15	15	–
COC-xGnP-20	20	–
COC_e90	–	90
COC-xGnP-1_e90	1	90
COC-xGnP-2_e90	2	90
COC-xGnP-5_e90	5	90
COC-xGnP-10_e90	10	90
COC_e110	–	110
COC-xGnP-1_e110	1	110
COC-xGnP-2_e110	2	110
COC-xGnP-5_e110	5	110
COC-xGnP-10_e110	10	110
COC_e130	–	130
COC-xGnP-1_e130	1	130
COC-xGnP-2_e130	2	130
COC-xGnP-5_e130	5	130
COC-xGnP-10_e130	10	130
COC_e150	–	150
COC-xGnP-1_e150	1	150
COC-xGnP-2_e150	2	150
COC-xGnP-5_e150	5	150
COC-xGnP-10_e150	10	150
COC-xGnP-15_e150	15	150
COC-xGnP-20_e150	20	150

nanocomposite foams with a filler amount of 5 wt%, expanded with depressurization from 90 bar. Table 1 summarizes the list of the prepared samples.

2.3. Experimental methodologies

2.3.1. Microstructure

Density measurements were carried out by a Gibertini E42 hydrostatic balance, through the displacement method in acetone (density at 20 °C of 0.792 g/cm^3).

The distribution of the cell size was measured through a Heerbrugg Wild M3Z optical microscope, and a statistical analysis was then performed to determine the mean cell diameter and the relative standard deviation values. The microstructural features of the foam cells were observed through a Carl Zeiss AG Supra 40 FESEM microscope, operating at an acceleration voltage of 5 kV. Samples were cryofractured in liquid nitrogen before observations. A Tecnai G2 Spirit Twin FEI TEM microscope operating at an accelerating voltage of 120 kV was used to investigate the silica dispersion within the polymeric matrix of both bulk and foamed materials in bright field (BF) imaging mode. Ultrathin specimens (thickness of about 50 nm) were prepared at room temperature by using an Ultracut UCT Leica ultramicrotome.

2.3.2. Mechanical properties

Quasi-static tensile tests on the bulk samples were performed through an Instron 4502 tensile testing machine, equipped with a load cell of 1 kN. ISO 527 1BA specimens were tested. Elastic modulus was evaluated at 1 mm/min, through a resistance extensometer with a gage length of 12.5 mm, while tensile tests at break were carried out without the extensometer at a crosshead speed of 5 mm/min. Mechanical properties of the foamed samples were evaluated at 1 mm/min in compression mode on square specimens with a lateral dimension of about 10 mm and a height of about 3 mm. The Young's modulus (E) of the foamed materials was determined by fitting the stress-strain curves in the initial linear region. All the tests were performed at ambient temperature and at least five specimens were tested for each composition.

Creep tests were carried out by a DMA Q800 machine (TA Instruments, USA) at a testing temperature of 30 °C for 60 minutes under a constant stress of 10% of the ultimate tensile strength of the neat matrix. Rectangular specimens 5 mm wide and 1 mm thick with a gage length of 10 mm were used to test both bulk samples and polymer foams.

3. Results and discussion

3.1. Morphology

Density values of the neat COC and bulk nanocomposites are reported in Table 2. The progressive increase of the density with the nanofiller amount can be explained considering the higher density of xGnP with respect to the neat matrix. It is also important to evaluate the effect of xGnP addition on the morphological properties of the prepared foams. Therefore, density measurements were performed also on the foams. In Figure 2 the foams density as a function of the nanofiller content is represented. A systematic

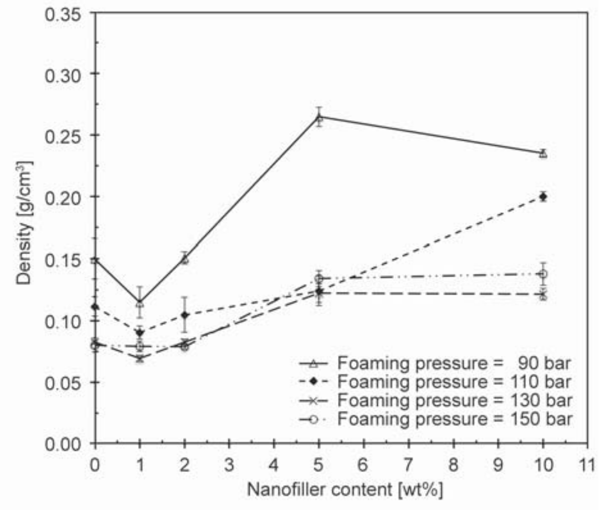

Figure 2. Foams density as a function of the nanofiller content for different foaming pressures

Table 2. Density, elastic modulus (E), stress at break (σ_b), strain at break (ε_b) and values of the creep compliance at 3600 s of bulk samples of neat COC and relative nanocomposites

Sample	Density [g/cm^3]	E [GPa]	σ_b [MPa]	ε_b [%]	$D(t = 3600)$ [MPa^{-1}]
COC	1.008±0.001	2.17±0.14	59.4±1.1	5.75±0.21	1.09
COC-xGnP-1	1.012±0.001	2.39±0.07	51.2±2.5	4.92±0.33	0.83
COC-xGnP-2	1.017±0.001	2.37±0.10	51.2±0.8	5.12±0.18	0.68
COC-xGnP-5	1.029±0.002	2.75±0.21	44.9±1.4	4.40±0.23	0.66
COC-xGnP-10	1.054±0.001	3.36±0.07	37.7±1.6	3.22±0.25	0.60

increase of density with the nanofiller amount can be observed over the whole range of applied pressures. Considering the density variation due to nanofiller addition in bulk samples (see Table 2), it is clear that the density increase in the nanocomposite foams cannot be simply explained by the higher density of xGnP, but also by a morphological change within the foam microstructure (i.e. cell density and cell size). In fact, as the foaming pressure increases, a density reduction can be observed for all the compositions. This could be due to the fact that at elevated pressures, the diffusion of the $scCO_2$ within the matrix is favoured and the foaming process is more efficient. To fully understand the density increment of the

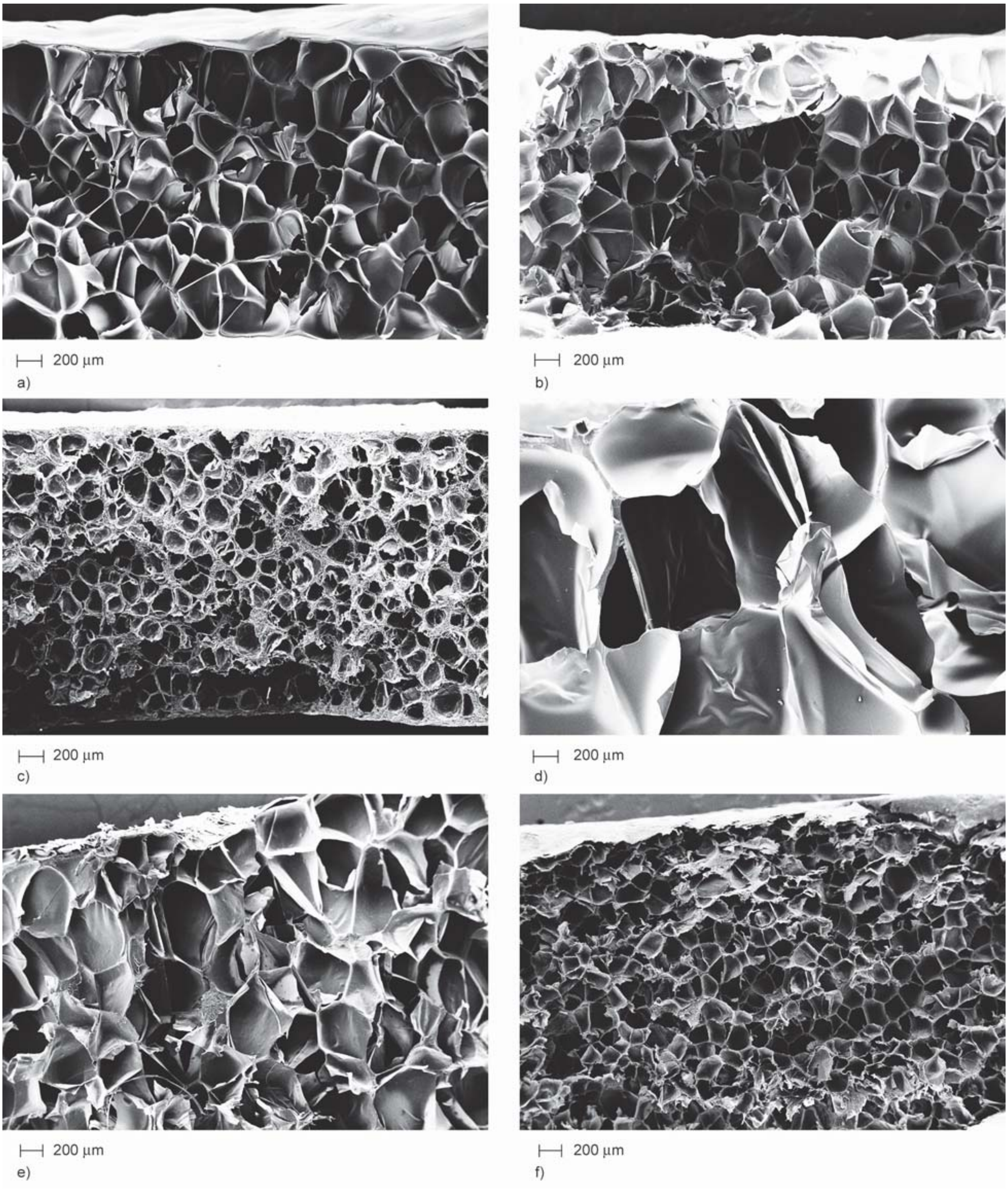

Figure 3. FESEM micrographs of the cryofractured surfaces of the foamed samples: (a) COC_e90, (b) COC-xGnP-1_e90, (c) COC-xGnP-10_e90 and (d) COC_e150, (e) COC-xGnP-1_e150, (f) COC-xGnP-10_e150

foams and the real contribution played by xGnP addition on the morphology of the prepared cellular solids, FESEM analysis was carried out. In Figure 3, low magnification FESEM micrographs of the foamed nanocomposite materials COC_e90, COC-xGnP-1_e90, COC-xGnP-10_e90 (Figure 3a, 3b, and 3c respectively) and COC_e150, COC-xGnP-1_e150, COC-xGnP-10_e150 (Figure 3d, 3e and 3f respectively) are compared. All foams present closed cell morphology with a narrow statistical distribution of the cell sizes around an average value. Similar morphological features were observed in a previous work of this group on COC foams filled with nanosilica [43]. From these micrographs, it is immediately evident the role played by the xGnP content and of the foaming pressure on the morphology of the samples. An increase of the nanofiller amount promotes a reduction of the cell size and a consequent increase of the cell density, while opposite effects can be obtained increasing the foaming pressure. A quantitative evaluation of the cell size distribution was performed by using ImageJ software (U. S. National Institutes of Health, Bethesda, Maryland, USA) [44]. Average cell diameter and cell density [cells/mm^2] as a function of the nanofiller content for foams expanded at 90 and 150 bar are reported in Figure 4. The nanofiller introduction hinders the cell growth during the expansion process, thus reducing the cell diameter both at 90 and 150 bar. At the same time, it promotes cell nucleation, increasing the cell density. In previous works of our group it was demonstrated how the nanofiller addition promotes a strong increase of the polymer viscosity in the molten state [45, 46]. It is therefore reasonable to assume that xGnP can enhance the matrix viscosity above the glass transition temperature, thus hindering the expansion process. Moreover, the foaming pressure seems to act in the opposite way. In fact, when scCO$_2$ pressure increases, the cell size increases while the cell density decreases. Therefore, it can be hypothesized that at higher pressure cell growth is favoured over cell nucleation.

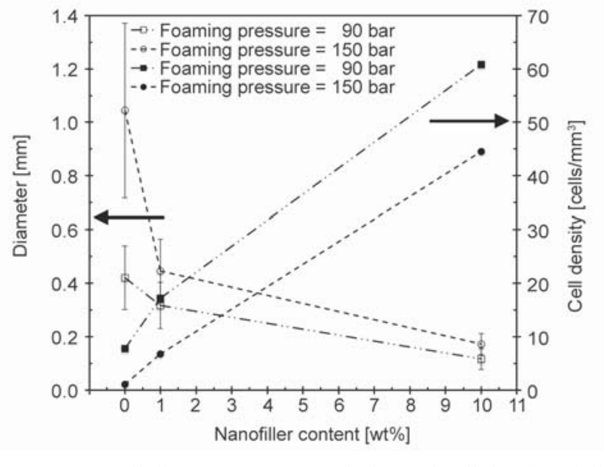

Figure 4. Cell diameter (open symbols) and cell density (full symbols) as a function of the nanofiller content for nanocomposite foams expanded at 90 bar and at 150 bar

A more detailed analysis at higher magnification levels was performed with FESEM equipment, in order to investigate possible exfoliation and/or orientation effects of xGnP nanoplatelets as a consequence of the foaming process. A FESEM micrograph of COC-xGnP-10 bulk sample is reported in Figure 5a. It is possible to observe that xGnP nanoplatelets are randomly oriented within the matrix, with the presence of agglomerates of stacked lamellae. Moreover, the fracture surface is irregular and jagged. Similar morphological features were also observed by Shadlou *et al*. [46] and Kalaitzidou *et al*. [33] on other xGnP-based nanocomposite systems. In Figure 5b and 5c the fracture surfaces of COC-xGnP-10_e90 and COC-xGnP-10_e150 are reported. An alignment of xGnP nanoplatelets along the cell walls can be noticed, and this effect is more pronounced at higher foaming pressures, where thinner cell walls can be detected. It is possible that under the selected foaming conditions the xGnP exfoliation process and alignment along the cell wall was promoted. The evident alignment of xGnP nanoplatelets at high foaming pressures can be better visualized in FESEM micrographs on COC-xGnP-10_e150 sample at high magnification (see Figure 5d).

In order to perform a deeper investigation of the dispersion level of xGnP in both bulk and foamed samples, TEM analysis was carried out. In Figure 6, TEM micrographs of bulk and foamed samples are reported. Figures 6a and 6b respectively show COC-xGnP-1 and COC-xGnP-10 bulk samples, while Figures 6c and 6d show the corresponding foamed samples at 150 bar. In Figure 6a it is clear that bulk samples at low filler amounts are characterized by stacks of xGnP lamellae with a lateral dimension of less than 50 nm and a length of about 1 μm. As already seen in other nanocomposite systems, an increase of the filler loading promotes a strong aggregation of the

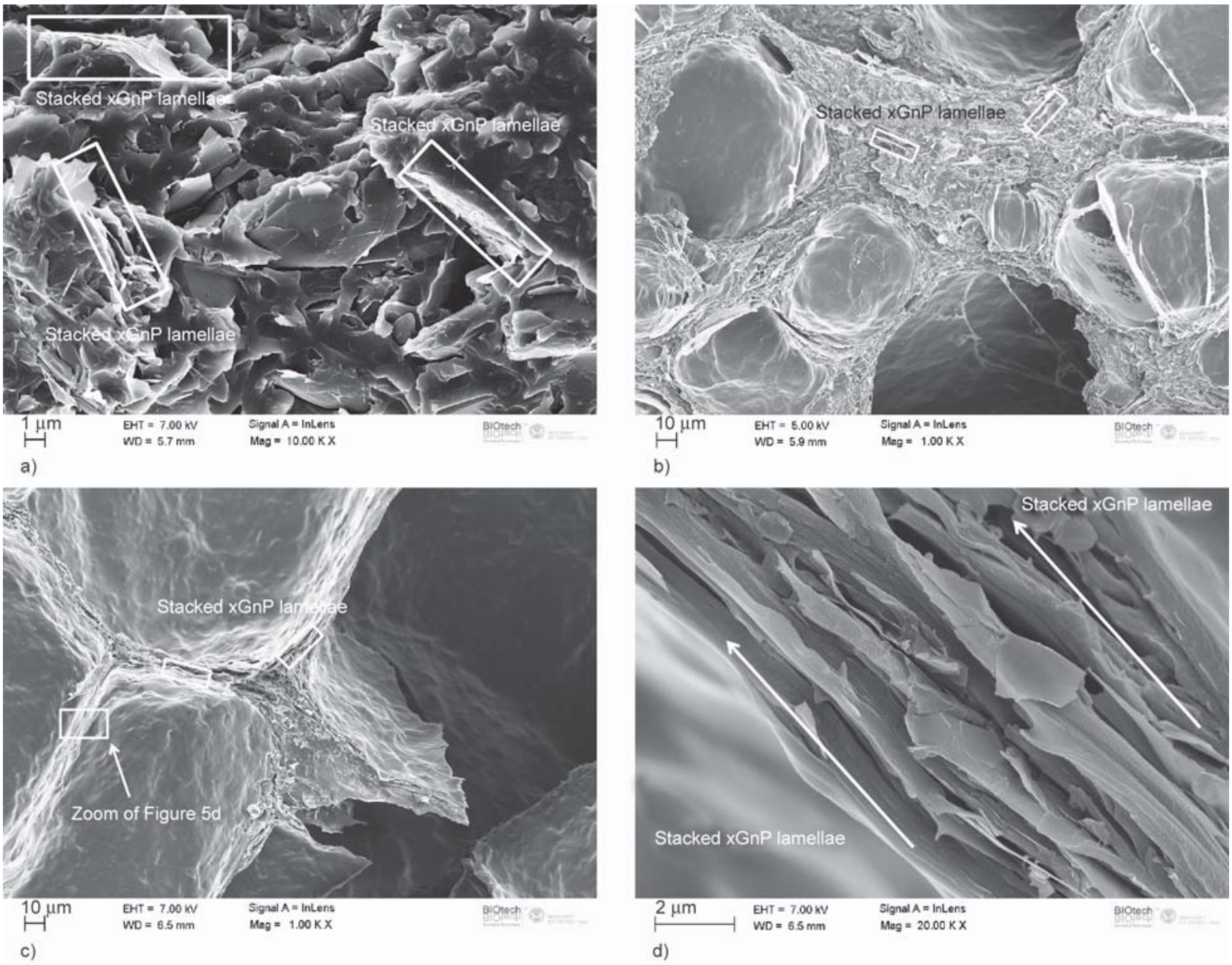

Figure 5. FESEM micrographs of the cryofractured surfaces of the samples: (a) COC-xGnP-10, (b) COC-xGnP-10_e90, (c) and (d) COC-xGnP-10_e150 at different magnifications

nanoplatelets [18] (see Figure 6b). It is interesting to observe that the foaming process leads to an improved exfoliation of xGnP nanoplatelets. In fact, comparing Figure 6a and 6c it is clear that in the foamed samples the agglomeration of the xGnP stacks is reduced. The same effect can be detected at higher filler loadings (see Figures 6b and 6d).

3.2. Mechanical behaviour

The effect of the nanofiller loading on the quasi-static tensile properties of the bulk samples was investigated and the most important results are summarized in Table 2. As frequently observed in nanofilled samples, the xGnP introduction leads to a noticeable increase of the elastic modulus [33]. In fact, composites with an xGnP content of 10 wt% show a 55% increase in the tensile modulus. The stiffening effect reported in our previous work for the same COC matrix reinforced with silica nanoparticles was less pronounced [18, 43]. This discrepancy is probably due to the higher stiffness of the xGnP with respect to silica and to its high aspect ratio which favours the load transfer. As a drawback, the presence of the nanofiller causes an embrittlement of the bulk samples, revealed by the decrease of both the stress and strain at break values (σ_b and ε_b) as the xGnP content increases. Most likely the nanofiller aggregation observed at higher filler loadings plays a negative effect on the ultimate properties of the resulting materials. The effect of xGnP introduction on the mechanical behaviour of the prepared foams under compression has been also investigated. Representative stress-strain curves from quasi-static compression tests on neat COC and relative nanocomposites foams at 110 bar are reported in Figure 7. In all the samples, a linear elastic region followed by the yielding of the samples and the plastic deformation of the material is observed. In the third region, a sharp increase of the stress can be detected. A quantitative evaluation of the elastic properties of the foams as a function of

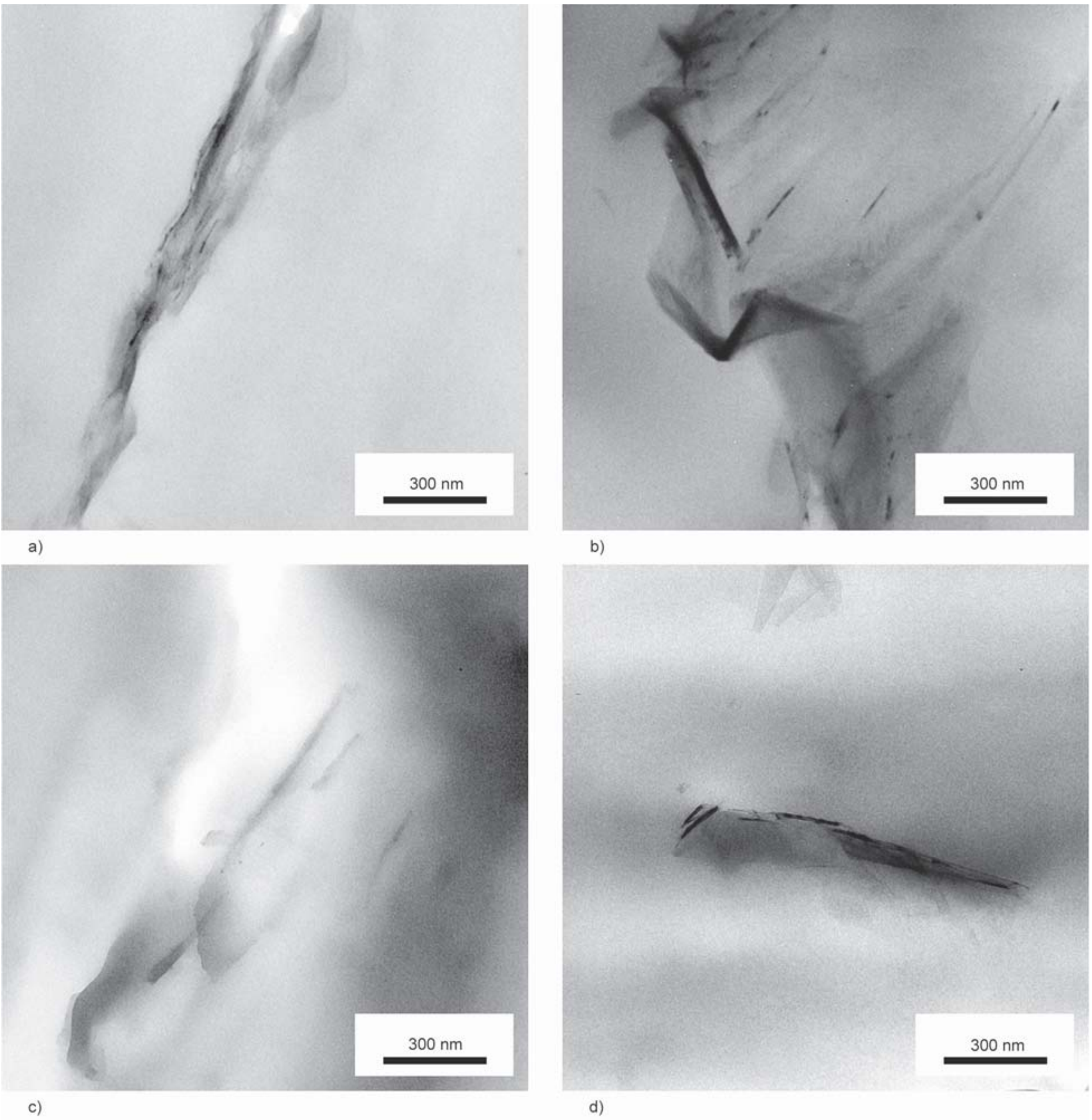

Figure 6. TEM micrographs of the bulk and foamed samples. (a) COC-xGnP-1, (b) COC-xGnP-10, (c) COC-xGnP-1_e150 and (d) COC-xGnP-10_e150.

the nanofiller loading is reported in Figure 8a and 8b, where the trends of the modulus and of the specific modulus (i.e. the ratio between the elastic modulus and density) are respectively represented. It is interesting to observe how the nanofiller introduction leads to a remarkable increase of the elastic modulus of the foams, over the whole range of applied foaming pressures. It is worthwhile to observe that the increase of the elastic modulus displayed by the nanofilled foams is noticeably higher than that of the corresponding bulk materials. In fact, with an applied pressure of 150 bar, the COC-xGnP-10_e150 sample manifests an elastic modulus about 10 times higher than the corresponding unfilled foam (see Figure 8a). Even in the case of specific modulus (Figure 8b) the stiffening effect due to nanofiller introduction is evident, especially at higher filler loadings. With an applied pressure of 150 bar, the COC-xGnP-10_e150 sample presents a specific elastic modulus almost 6 times higher than the corresponding unfilled foam. From this example, it is clear that the enhancement of the foams stiffness is partially due to a change in the foams density, but the greater contribution is due to the xGnP addition. As already observed in the pre-

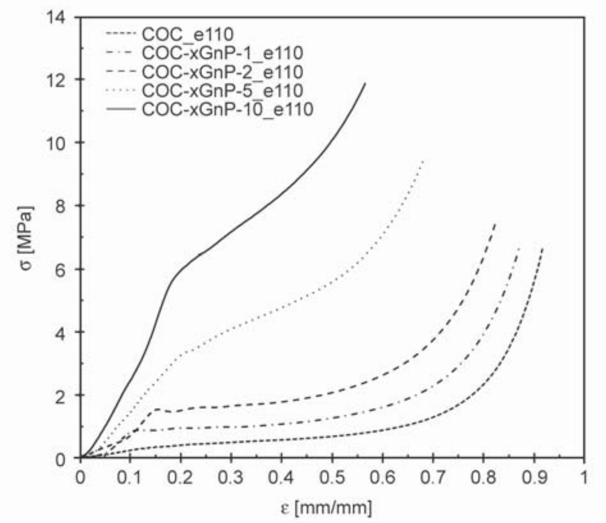

Figure 7. Representative stress-strain curves from quasi-static compression tests on neat COC and relative nanocomposites foamed at 110 bar

vious paragraph, the occurrence of xGnP exfoliation and orientation given by the foaming pressure can increase the mechanical properties of the matrix itself. However, a more detailed morphological analysis is required to achieve a complete description of the role played by nanofiller morphology on the elastic properties of the nanocomposite foams. The enhancement in the mechanical properties of foams with the nanofiller amount was also observed by Jo *et al*. [47] in their study about HDPE/clay nanocomposite foams.

In order to confirm the positive effect played by xGnP nanoplatelets on the mechanical behaviour of bulk and foamed nanocomposites, creep tests were performed. From Table 2 it can be observed how the stabilizing effect due to nanofiller introduction in the bulk materials leads to an interesting decrease of the creep compliance with respect to the neat COC. For instance, with a nanofiller amount of 10 wt%, the creep compliance at 3600 s is reduced of about 45% with respect of the neat COC. This effect is even more pronounced for foamed materials. In Figure 9a creep compliance curves of neat COC and relative nanocomposite foams expanded at 110 bar are reported, while Figure 9b shows the creep compliance values at 3600 s. In accordance with elastic modulus results, it can be concluded that the creep stability increases due to nanofiller introduction along the whole range of applied pressures. For instance, considering a pressure of 150 bar, the creep compliance at 3600 s is reduced of about 2.5 times with a nanofiller amount of 10 wt%. Even in this case, the observed stabilizing effect is partly due to a change in the foam density, and a key role is played by xGnP exfoliation and orientation effects.

4. Conclusions

Cycloolefin copolymer/exfoliated graphite nanoplatelets (xGnP) composites were prepared at different filler amounts through a melt compounding process. The resulting materials were foamed through a supercritical carbon dioxide based process by varying the foaming pressure. Bulk and foamed materials were then characterized from a morphological and a mechanical points of view, in order to understand the role of the nanofiller amount and of the foaming pressure on their physical properties. It was observed how the xGnP introduction systematically increased both bulk (from 1.01 up to 1.05 g/cm^3 with a xGnP

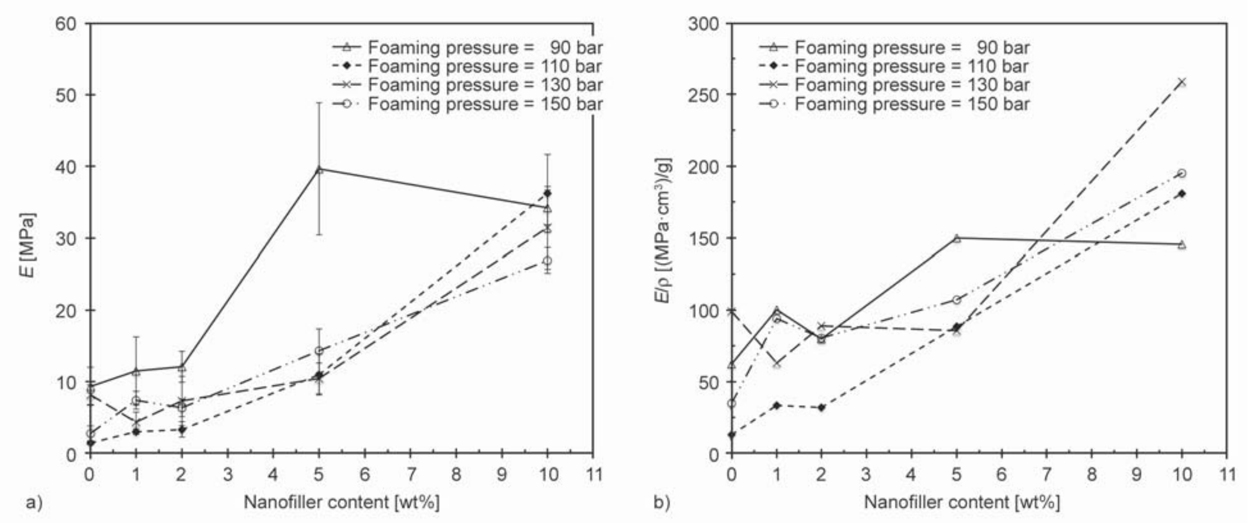

Figure 8. (a) Elastic modulus (*E*), (b) normalized elastic modulus over density (*E*/ρ) of the foamed samples

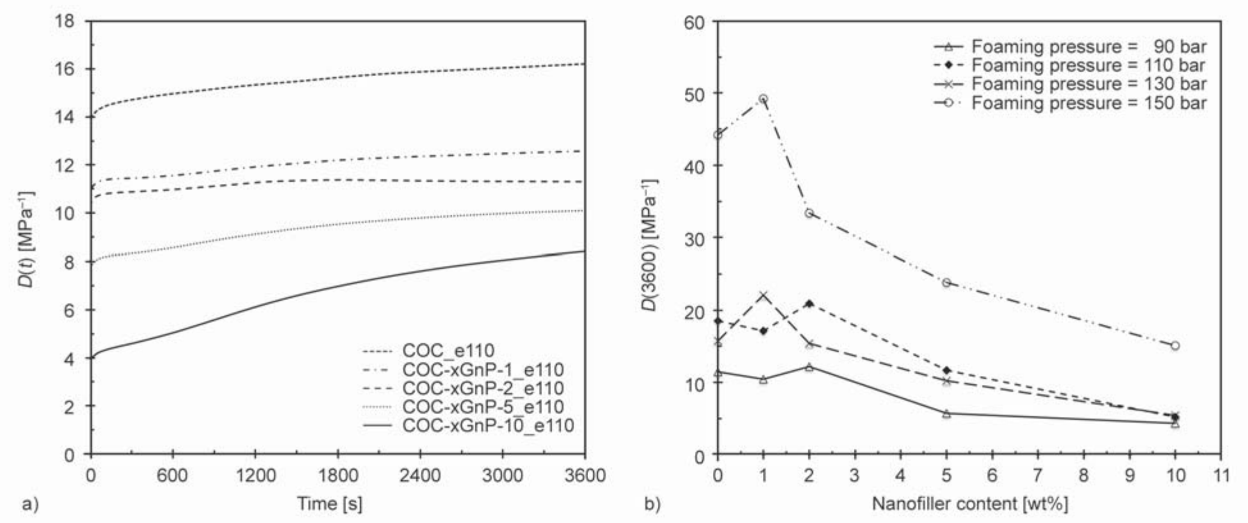

Figure 9. (a) Creep compliance curves of neat COC and relative nanocomposites at a foaming pressure of 110 bar. (b) Creep compliance at 3600 s as a function of the nanofiller content for nanocomposite foams at different foaming pressures.

amount of 10 wt%) and foam density (from 0.15 up to 0.24 g/cm^3 with a xGnP amount of 10 wt% at 90 bar), while elevated foaming pressures promoted a consistent density reduction. Microstructural analysis on the resulting foams highlighted a progressive increase of the mean cell size with the foaming pressure, accompanied by an evident exfoliation and orientation of the nanoplatelets along the cell walls direction. These microstructural effects were responsible for an important improvement of the mechanical properties of the foams, with a progressive enhancement of the elastic properties with xGnP amount (with a pressure of 150 bar, the COC-xGnP-10_e150 sample has an elastic modulus about 10 times higher than the corresponding unfilled foam), and also the creep stability was noticeably improved. Concluding, foaming process of COC nanocomposites through supercritical carbon dioxide could represent an effective way to prepare low density polymeric foams characterized by higher mechanical stability with respect to the corresponding neat COC copolymer.

Acknowledgements

TEM microscopy at the Institute of Macromolecular Chemistry was supported by projects TE01020118 (Technology Agency of the CR) and POLYMAT LO1507 (Ministry of Education, Youth and Sports of the CR, program NPU I).

References

[1] Kozlowski M.: Lightweight plastic materials. InTech, Rijeka (2012).

[2] Papadopoulos A. M.: State of the art in thermal insulation materials and aims for future developments. Energy and Buildings, **37**, 77–86 (2005). DOI: 10.1016/j.enbuild.2004.05.006

[3] Cooper A. I.: Porous materials and supercritical fluids. Advanced Materials, **15**, 1049–1059 (2003). DOI: 10.1002/adma.200300380

[4] Lee S-T., Scholz D. P. K.: Polymeric foams: Technology and developments in regulation, process, and products. CRC Press, Boca Raton (2008).

[5] Bhattacharya S., Gupta R. K., Jollands M., Bhattacharya S. N.: Foaming behavior of high-melt strength polypropylene/clay nanocomposites. Polymer Engineering and Science, **49**, 2070–2084 (2009). DOI: 10.1002/pen.21343

[6] Gendron R., Champagne M. F., Tatibouet J., Bureau M. N.: Foaming cyclo-olefin copolymers with carbon dioxide. Cellular Polymers, **28**, 1–23 (2009).

[7] Han X., Koelling K. W., Tomasko D. L., Lee L. J.: Continuous microcellular polystyrene foam extrusion with supercritical CO$_2$. Polymer Engineering and Science, **42**, 2094–2106 (2002). DOI: 10.1002/pen.11100

[8] Han X., Zeng C., Lee L. J., Koelling K. W., Tomasko D. L.: Extrusion of polystyrene nanocomposite foams with supercritical CO$_2$. Polymer Engineering and Science, **43**, 1261–1275 (2003). DOI: 10.1002/pen.10107

[9] Jiang X-L., Bao J-B., Liu T., Zhao L., Xu Z-M., Yuan W-K.: Microcellular foaming of polypropylene/clay nanocomposites with supercritical carbon dioxide. Journal of Cellular Plastics, **45**, 515–538 (2009). DOI: 10.1177/0021955X09339470

[10] Nam P. H., Maiti P., Okamoto M., Kotaka T., Nakayama T., Takada M., Ohshima M., Usuki A., Hasegawa N., Okamoto H.: Foam processing and cellular structure of polypropylene/clay nanocomposites. Polymer Engineering and Science, **42**, 1907–1918 (2002).
DOI: 10.1002/pen.11083

[11] Otsuka T., Taki K., Ohshima M.: Nanocellular foams of PS/PMMA polymer blends. Macromolecular Materials and Engineering, **293**, 78–82 (2008).
DOI: 10.1002/mame.200700257

[12] Strauss W., D'Souza N. A.: Supercritical CO_2 processed polystyrene nanocomposite foams. Journal of Cellular Plastics, 40, 229-241 (2004).
DOI: 10.1177/0021955X04043720

[13] Xu Z-M., Jiang X-L., Liu T., Hu G-H., Zhao L., Zhu Z-N., Yuan W-K.: Foaming of polypropylene with supercritical carbon dioxide. The Journal of Supercritical Fluids, **41**, 299–310 (2007).
DOI: 10.1016/j.supflu.2006.09.007

[14] McHugh M., Krukonis V.: Supercritical fluid extraction: Principles and practice. Elsevier, Amsterdam (2013).

[15] Nalawade S. P., Picchioni F., Janssen L. P. B. M.: Supercritical carbon dioxide as a green solvent for processing polymer melts: Processing aspects and applications. Progress in Polymer Science, **31**, 19–43 (2006).
DOI: 10.1016/j.progpolymsci.2005.08.002

[16] Yeo S-D., Kiran E.: Formation of polymer particles with supercritical fluids: A review. The Journal of Supercritical Fluids, **34**, 287–308 (2005).
DOI: 10.1016/j.supflu.2004.10.006

[17] Arndt M., Beulich I.: C_1-symmetric metallocenes for olefin polymerisation, 1. Catalytic performance of $[Me_2C(3\text{-}^{tert}BuCp)(Flu)]ZrCl_2$ in ethene/norbornene copolymerisation. Macromolecular Chemistry and Physics, **199**, 1221–1232 (1998).
DOI: 10.1002/(SICI)1521-3935(19980601)199:6<1221::AID-MACP1221>3.0.CO;2-2

[18] Dorigato A., Pegoretti A., Fambri L., Slouf M., Kolařík J.: Journal of Applied Polymer Science, **119**, 3393–3402 (2011).
DOI: 10.1002/app.32988

[19] Ou C-F., Hsu M-C.: Preparation and properties of cycloolefin copolymer/silica hybrids. Journal of Applied Polymer Science, **104**, 2542–2548 (2007).
DOI: 10.1002/app.25983

[20] Ou C-F., Hsu M-C.: Preparation and characterization of cyclo olefin copolymer (COC)/silica nanoparticle composites by solution blending. Journal of Polymer Research, **14**, 373–378 (2007).
DOI: 10.1007/s10965-007-9119-5

[21] Forsyth J. F., Scrivani T., Benavente R., Marestin C., Pereña J. M.: Thermal and dynamic mechanical behavior of ethylene/norbornene copolymers with medium norbornene contents. Journal of Applied Polymer Science, **82**, 2159–2165 (2001).
DOI: 10.1002/app.2063

[22] Pegoretti A., Kolařík J., Fambri L., Penati A.: Polypropylene/cycloolefin copolymer blends: Effects of fibrous phase structure on tensile mechanical properties. Polymer, **44**, 3381–3387 (2003).
DOI: 10.1016/s0032-3861(03)00248-9

[23] Kolařík J., Pegoretti A., Fambri L., Penati A.: High-density polyethylene/cycloolefin copolymer blends, Part 2: Nonlinear tensile creep. Polymer Engineering and Science, **46**, 1363–1373 (2006).
DOI: 10.1002/pen.20580

[24] Ajayan P. M., Schadler L. S., Braun P. V.: Nanocomposite science and technology. Wiley, New York (2006).

[25] Bondioli F., Dorigato A., Fabbri P., Messori M., Pegoretti A.: High-density polyethylene reinforced with submicron titania particles. Polymer Engineering and Science, **48**, 448–457 (2008).
DOI: 10.1002/pen.20973

[26] Dorigato A., Pegoretti A., Migliaresi C.: Physical properties of polyhedral oligomeric silsesquioxanes–cycloolefin copolymer nanocomposites. Journal of Applied Polymer Science, **114**, 2270–2279 (2009).
DOI: 10.1002/app.30593

[27] Drzal L. T., Fukushima H.: Exfoliated graphite nanoplatelets (xGnP): A carbon nanotube alternative. in 'Proceedings of NSTI Nanotechnology Conference and Trade Show, Boston, USA' Vol 1, 170–173 (2006).

[28] Kim S., Do I., Drzal L. T.: Thermal stability and dynamic mechanical behavior of exfoliated graphite nanoplatelets-LLDPE nanocomposites. Polymer Composites, **31**, 755–761 (2010).
DOI: 10.1002/pc.20781

[29] Pedrazzoli D., Pegoretti A.: Expanded graphite nanoplatelets as coupling agents in glass fiber reinforced polypropylene composites. Composites Part A: Applied Science and Manufacturing, **66**, 25–34 (2014).
DOI: 10.1016/j.compositesa.2014.06.016

[30] Persson H., Yao Y., Klement U., Rychwalski R.: A simple way of improving graphite nanoplatelets (GNP) for their incorporation into a polymer matrix. Express Polymer Letters, **6**, 142–147 (2012).
DOI: 10.3144/expresspolymlett.2012.15

[31] Ferreira C. I., Dal Castel C., Oviedo M. A. S., Mauler R. S.: Isothermal and non-isothermal crystallization kinetics of polypropylene/exfoliated graphite nanocomposites. Thermochimica Acta, **553**, 40–48 (2013).
DOI: 10.1016/j.tca.2012.11.025

[32] Akın D., Kasgoz A., Durmus A.: Quantifying microstructure, electrical and mechanical properties of carbon fiber and expanded graphite filled cyclic olefin copolymer composites. Composites Part A: Applied Science and Manufacturing, **60**, 44–51 (2014).
DOI: 10.1016/j.compositesa.2014.01.008

[33] Kalaitzidou K., Fukushima H., Drzal L. T.: Mechanical properties and morphological characterization of exfoliated graphite–polypropylene nanocomposites. Composites Part A: Applied Science and Manufacturing, **38**, 1675–1682 (2007).
DOI: 10.1016/j.compositesa.2007.02.003

[34] Pierson H. O.: Handbook of carbon, graphite, diamonds and fullerenes: Processing, properties and applications. William Andrew, Norwich (2012).

[35] Liu W-W., Chai S-P., Mohamed A. R., Hashim U.: Synthesis and characterization of graphene and carbon nanotubes: A review on the past and recent developments. Journal of Industrial and Engineering Chemistry, **20**, 1171–1185 (2014).
DOI: 10.1016/j.jiec.2013.08.028

[36] Mittal G., Dhand V., Rhee K. Y., Park S-J., Lee W. R.: A review on carbon nanotubes and graphene as fillers in reinforced polymer nanocomposites. Journal of Industrial and Engineering Chemistry, **21**, 11–25 (2015).
DOI: 10.1016/j.jiec.2014.03.022

[37] Singh V., Joung D., Zhai L., Das S., Khondaker S. I., Seal S.: Graphene based materials: Past, present and future. Progress in Materials Science, **56**, 1178–1271 (2011).
DOI: 10.1016/j.pmatsci.2011.03.003

[38] Chen L., Schadler L. S., Ozisik R.: An experimental and theoretical investigation of the compressive properties of multi-walled carbon nanotube/poly(methyl methacrylate) nanocomposite foams. Polymer, **52**, 2899–2909 (2011).
DOI: 10.1016/j.polymer.2011.04.050

[39] Gedler G., Antunes M., Realinho V., Velasco J. I.: Thermal stability of polycarbonate-graphene nanocomposite foams. Polymer Degradation and Stability, **97**, 1297–1304 (2012).
DOI: 10.1016/j.polymdegradstab.2012.05.027

[40] Gedler G., Antunes M., Realinho V., Velasco J. I.: Novel polycarbonate-graphene nanocomposite foams prepared by CO_2 dissolution. IOP Conference Series: Materials Science and Engineering, **31**, 012008/1–012008/9 (2002).
DOI: 10.1088/1757-899X/31/1/012008

[41] Antunes M., Gedler G., Velasco J. I.: Multifunctional nanocomposite foams based on polypropylene with carbon nanofillers. Journal of Cellular Plastics, **49**, 259–279 (2013).
DOI: 10.1177/0021955X13477433

[42] Yeh S-K., Huang C-H., Su C-C., Cheng K-C., Chuang T-H., Guo W-J., Wang S-F.: Effect of dispersion method and process variables on the properties of supercritical CO_2 foamed polystyrene/graphite nanocomposite foam. Polymer Engineering and Science, **53**, 2061–2072 (2013).
DOI: 10.1002/pen.23468

[43] Pegoretti A., Dorigato A., Biani A., Slouf M.: Cyclic olefin copolymer–silica nanocomposites foams. Journal of Materials Science, **51**, 3907–3916 (2016).
DOI: 10.1007/s10853-015-9710-9

[44] Dorigato A., Pegoretti A., Penati A.: Linear low-density polyethylene/silica micro-and nanocomposites: Dynamic rheological measurements and modelling. Express Polymer Letters, **4**, 115–129 (2010).
DOI: 10.3144/expresspolymlett.2010.16

[45] Pedrazzoli D., Dorigato A., Pegoretti A.: Monitoring the mechanical behaviour of electrically conductive polymer nanocomposites under ramp and creep conditions. Journal of Nanoscience and Nanotechnology, **12**, 4093–4102 (2012).
DOI: 10.1166/jnn.2012.6219

[46] Shadlou S., Ahmadi-Moghadam B., Taheri F.: The effect of strain-rate on the tensile and compressive behavior of graphene reinforced epoxy/nanocomposites. Materials and Design, **59**, 439–447 (2014).
DOI: 10.1016/j.matdes.2014.03.020

[47] Jo C., Naguib H. E.: Constitutive modeling of HDPE polymer/clay nanocomposite foams. Polymer, **48**, 3349–3360 (2007).
DOI: 10.1016/j.polymer.2007.03.056

eXPRESS Polymer Letters Vol.10, No.12 (2016) 990–1002
Available online at www.expresspolymlett.com
DOI: 10.3144/expresspolymlett.2016.92

Fluorescence detection system based on silicon quantum dots–polysilane nanocomposites

L. Sacarescu[*], *G. Roman, G. Sacarescu, M. Simionescu*

Petru Poni Institute of Macromolecular Chemistry, Aleea Grigore Ghica Voda 41A, 700487 Iasi, Romania

Received 4 May 2016; accepted in revised form 16 July 2016

Abstract. A dual channel fluorescence system that combines the optical properties of silicon quantum dots–polysilane nanocomposites with those of 2-(4-chlorophenyl)-6-(thiophen-2-yl)pyridine, a fluorescent cytotoxic agent, is presented. The system is capable to alternatively trigger emission signals at two different wavelengths by excitation at a single wavelength. For this purpose a highly stable colloidal dispersion of silicon quantum dots–polysilane nanocomposite is prepared by a one-pot synthetic method using microwave-activated Wurtz coupling of organochlorosilanes. The size and shape of the silicon quantum dots within the polysilane thin film are studied by TEM. The colloidal dispersions are investigated by SAXS, which evidences that polysilane plays also a role as stabilizing agent to prevent aggregation. UV-vis spectrophotometry of the silicon quantum dots–polysilane nanocomposites in the presence of 2-(4-chlorophenyl)-6-(thiophen-2-yl)pyridine is used to define the active wavelength range and establish the fluorescence detection method.

Keywords: *polymer composites, nanomaterials, quantum dots, chemical synthesis, optical properties*

1. Introduction

During the last decade, intense efforts have been undertaken to miniaturize optical and electronic devices while increasing their efficiency [1–3]. Nowadays, the development of nano and quantum devices for high tech applications is close to go beyond the fundamental conceptual stage. From this point of view an attractive and still unexplored domain is related to systems were inorganic nanoparticles interact with organic molecules or polymers having specific optoelectronic properties [4–6]. The variety of particles and polymers having exciting optical and/or electronic properties continuously grows, and several of them seem to have the necessary potential toward new developments [7–10]. This work aims at showing the interesting optical properties that could be obtained when both the inorganic nanoparticles and polymer are silicon-based structures.

Quantum dots are promising materials for a wide range of applications related to quantum electronics [11–14]. Silicon itself represents a special case amongst the semiconductive materials used to obtain quantum dots. An important advantage of silicon quantum dots (SiQDs) is that, unlike other elements, silicon is biocompatible. Consequently, SiQDs can be used in hot research fields of nanomedicine, such as fluorescent sensing, labelling and dynamic therapy [15–18]. On the other hand, SiQDs still undergo intensive research, since their fundamental photophysics is less understood than the photophysics of particles made from direct gap semiconductors [19]. In addition, obtaining SiQDs in a controlled manner is still a challenge.

Within the class of silicon-based conjugated polymers, polysilanes present interesting optoelectronic properties owing to their σ conjugated chains [20, 21]. An increase in the substitution of the silicon

---

[*] Corresponding author, e-mail: livius@icmpp.ro

chain in polysilanes with aromatic moieties leads to further enhancement of their optoelectronical properties, owing to the intermingling of σ and σ–π conjugation. This extended conjugation also makes polysilanes sensitive towards light, but this disadvantage could be turned into an advantage in applications such as micro- and nanolithography [22–24]. In addition, polysilanes have interesting non-linear optical (NLO) properties, and they possess intrinsic semiconductivity [25–31].

Polyhydrosilanes are a distinct class of polyorganosilane polymers containing hydrosilyl moieties [32]. The properties of these functional silicon-based macromolecular structures are different from those of poly(diorganosilylene)s [33, 34]. Due to the reactive methylhydrosilyl segments, such materials have been used to generate *in situ* important amounts of silicon nanoparticles [35]. Steady-state fluorescence analysis showed that the presence of the silicon nanoparticles within the polysilane matrix leads to characteristic modifications in the emission spectrum profile [36].

The current study describes a one-pot synthetic method and the optical properties of silicon quantum dots–polysilane nanocomposites (NQD). Subsequently, the dual channel fluorescence of NQD in the presence of the antitumoral agent 2-(4-chlorophenyl)-6-(thiophen-2-yl)pyridine (CTP) is studied. Such materials have a high potential for applications in the field of nanomedicine as molecular contrasting agents in imaging and therapy of tumours.

2. Experimental

2.1. Materials

Dichlorodiphenylsilane, $(C_6H_5)_2SiCl_2$, (>98%, 42930) and dichloromethylsilane (>98%, 440248), $(CH_3)HSiCl_2$, were purchased from Sigma-Aldrich Chemie GmbH, Germany and distilled prior to use. Toluene (244511) and tetrahydrofuran (THF, 401757) were purchased from Aldrich and used after distillation over sodium wire under nitrogen atmosphere. 2-Acetylthiophene (W503509), paraformaldehyde (P6148), dimethylamine hydrochloride (38960), 2-bromo-1-(4-chlorophenyl)ethanone (101273), ammonium acetate (A7330), pyridine (270970) and the solvents required for the synthesis of CTP were obtained from Sigma-Aldrich Chemie GmbH, Germany and were used as such. 3-Dimetylamino-1-(thiophen-2-yl)propan-1-one hydrochloride and 1-(2-(4-chlorophenyl)-2-oxoethyl)pyridinium bromide were prepared as already described in a previously published article [37].

Poly[diphenyl-*co*-methyl(H)]silane copolymer, molar ratio $(C_6H_5)_2Si/CH_3(H)Si$ 1:1, was obtained in a closed reaction system using a Discover Labmate microwave reactor (CEM Corporation, USA) equipped with an infrared temperature probe and a magnetic stirrer [38]. The reactor was operated in standard conditions under the control of its Synergy software, by employing temperature as main parameter.

2.2. Synthesis of NQD

A simple, one-pot method to obtain soluble polysilane–silicon nanoparticles composite has been described previously [39]. This approach is based on the Wurtz coupling of methyldichlorosilane with various organodichlorosilanes in heterogeneous conditions. Thus, beside the polyhydrosilane copolymer, silicon nanoparticles are present in the final reaction product. In order to increase the content in silicon nanoparticles within the polymer matrix, a modified synthetic procedure is presented in this work. This time the coupling reaction is performed under microwaves irradiation.

A 10 mL microwave vial containing a magnetic stirring bar was flushed with dry nitrogen at 80 °C for 30 min, then a mixture of diphenyldichlorosilane (1.5 g, 6 mmol) and methyl(H)dichlorosilane (0.7 g, 6 mmol) in 2 mL dry toluene was added. Next, a dispersion of sodium (0.5 g) in toluene (2 mL) was carefully added, and then the reaction mixture was degassed by ultrasonication under dry nitrogen. The microwave reactor setup was in standard mode, close vessel conditions, with the following parameters: power = 50 W; temperature = 120 °C; time = 10 min. The exothermal coupling reaction started almost instantly, and the temperature rose quickly to approx. 100 °C. At the end of the reaction time, the dark purple mixture was cooled to room temperature before it was transferred into a 50 mL flask. Dry toluene (10 mL) was added, and the unreacted sodium was quenched carefully, under efficient stirring, using 10 mL of ethanol. The organic layer was washed with distilled water until neutral pH and subsequently dried over anhydrous $MgSO_4$. Toluene was removed under reduced pressure, and then THF (1 mL) was added to dissolve the solid material. The solution was poured onto 100 mL methanol, and the resulting white precipitate was filtered and vacuum dried at 50 °C overnight to afford NQD as a powder (1.7 g, 75%). ^{1}H-NMR (400 MHz, $CDCl_3$, δ): 0.48 (Si–CH_3), 4.7 (Si–H), 7.28 (Si–C_6H_5). FTIR (KBr, cm^{-1}): 3064 and 3045 (C–H_{arom}), 2953 and 2893 (C–H_{aliph}), 2100 (Si–H), 1424 and 1096 (Si–C_6H_5), 1243 (Si–CH_3), 695 (Si–C), 461 (Si–Si). GPC (SLS-MALS, 1 mg/mL in THF): $M_w = 4495$ mol·g^{-1}; $M_w/M_n = 1.5$.

2.3. Synthesis of 2-(4-chlorophenyl)-6-(thiophen-2-yl)pyridine (CTP)

CTP was synthesized using a previously reported procedure through the condensation of 3-dimetylamino-1-(thiophen-2-yl)propan-1-one hydrochloride **1**, 1-(4-chlorophenacyl) pyridinium bromide **2** and ammonium acetate, and obtained as colorless crystals, mp 88–89 °C. ^{1}H-NMR (400 MHz, $CDCl_3$, δ): 7.13 (dd, J = 3.8 and 5.0 Hz, 1H), 7.42 (dd, J = 1.0 and 5.0 Hz, 1H), 7.46 (d, J = 8.8 Hz, 2H), 7.54–7.61 (m, 2H), 7.65 (dd, J = 1.0 and 3.8 Hz, 1H), 7.74 (t, J = 8.0 Hz, 1H), 8.06 (d, J = 8.8 Hz, 2H). ^{13}C-NMR (400 MHz, $CDCl_3$, δ): 117.3, 118.1, 124.8, 127.9, 128.1, 128.3, 129.0, 135.3, 137.5, 137.7, 145.4, 152.5, 155.6. Anal. calcd. for $C_{15}H_{10}ClNS$: C 66.29, H 3.71, N 5.15; found: C 66.41, H 3.62, N 5.27 [37].

3. Measurements

^{1}H- and ^{13}C-NMR spectra were recorded at room temperature using a Bruker DRX 400 MHz NMR instrument (Bruker Corporation, Germany). In the case of CTP, the signals owing to the residual protons in $CDCl_3$ were used as internal standard for the ^{1}H-NMR spectrum, while the chemical shifts for the carbon atoms in the ^{13}C-NMR spectrum are given relative to residual $CHCl_3$ (δ = 77.16 ppm). Gel permeation chromatography (GPC) analysis was performed in THF solution at 25 °C and at a flow rate of 1 mL/min using a WGE SEC/GPC multidetection chromatograph (WGE Dr Bures GmbH&Co KG, Germany) equipped with two Agilent PLgel 5 µm MIXED columns (103 and 500 Å). Transmission electron microscopy (TEM) analysis was performed with a Hitachi HT7700 microscope (Hitachi High-Technologies Corporation, Japan) operated in high-contrast mode at 100 kV accelerating voltage. The microscope was used to examine the samples in High Resolution/High Contrast, Diffraction and STEM-EDX modes. The samples were prepared by drop casting the solution directly on the TEM grids (Ted Pella, 300 mesh, carbon layer) and they were subsequently kept in a box saturated with solvent vapors for 24 h. Finally, the box was slowly flushed with nitrogen for another 24 h, and the samples were dried under vacuum at room temperature for 60 h. TEM analysis was performed at –190 °C in order to avoid the thermal destruction of the samples. Small-angle X-ray scattering (SAXS) measurements were carried out using a Bruker NanostarU instrument (Bruker Corporation, Germany) equipped with a IµS microsource with copper anode and a three-pinhole collimation system. A highly sensitive 2D detector (Vantec-2000), having 68 µm resolution, was used to record the scattered intensity. The scattered intensity $I(q)$ is measured as a function of the momentum transfer vector $q = 4\pi\sin\theta/\lambda$, where λ is the wavelength of the X-rays (Cu Kα radiation, 1.54 Å), and θ is half the scattering angle. The sample-to-detector distance was 107 cm, allowing measurements with q values between 0.008 and 0.3 Å^{-1}. The angular scale was calibrated by the scattering peaks of a silver behenate standard. Solutions of the samples under study were sealed in a quartz capillary and measured under vacuum at constant temperature, 25 °C for 8000 s. The raw data was normalized for the transmission coefficient and the incoherent scattering due to the capillary and solvent backgrounds were subtracted in the data analysis using the SAXS–Bruker AXS software. Data analysis was done using ATSAS 2.5.1 package and DIFFRAC^{plus} NanoFit [40]. Electronic absorption spectra (UV-vis) were recorded using a UV 7100 spectrophotometer (Shimadzu, Japan), while fluorescence spectra were obtained on a Horiba FluoroMax-4 spectrofluorometer (Horiba Scientific, Japan). All spectroscopic measurements were performed in solution at room temperature after the samples were deaerated thoroughly with nitrogen for 20 min. Fluorescence spectra were recorded by exciting the investigated materials at their corresponding absorption maxima.

4. Results and discussion

4.1. Morphologies and structures

The synthesis of NQD has been performed by the heterogeneous Wurtz coupling of equimolar amounts of diphenyldichlorosilane and methyl(H)dichlorosilane using microwaves. The reaction takes place in toluene solvent in the presence of dispersed sodium. The process is complex and the influence of microwaves is reflected especially in the effects on the reaction time, the yield and the content of silicon particles in the nanocomposite. In the current approach microwaves were used at a considerably low power. Thus, the action of microwaves was strong enough to act upon the polar species present in the reaction system, while being too weak to initiate secondary reactions. Figure 1 shows the mechanism through which the main intermediates responsible for the generation of SiQDs arise from the thermal cleavage of the methylhydrosilyl segments. These silylenes are prone to be affected by microwaves, and they accelerate the chemo-restructuration processes that finally lead to formation of SiQDs (Figure 1). This process runs in competition with the main Wurtz coupling reaction and lead to scission of some of polyhydrosilane chains into low molecular weight species. These are soluble in methanol and are eliminated during purification. Through this approach, relative large quantities of NQD could be obtained easily in a sequence of experiments under perfectly controlled conditions. While the microwave-assisted method ensures a high reproducibility of the process, it has always been difficult to obtain batches of composites with similar characteristics using conventional heating [39]. Another important advantage of the method is that it produces *in situ* a solid state precursor for colloidal SiQDs dispersions. Such colloidal dispersions can be obtained by simply dissolving NQD in common organic solvents (xylenes, toluene, tetrahydrofuran). Due to the specific interfacial properties, polyhydrosilane acts like a stabilizing agent for SiQDs, and these dispersions are highly stable. For example, samples kept in the dark at room temperature and under an inert atmosphere preserve their properties and appearence unaltered, and they can be used to produce thin films on various supports.

The polymeric matrix resulted from this synthesis is a polyhydrosilane copolymer with a statistical distribution of methylhydrosilyl and diphenylsilyl segments. The molar rate for these two structural units was $M_r = 1:0.8$, as estimated by ^{1}H-NMR. As shown previously, the main characteristic of this material is the presence of silicon nanoparticles that are dispersed within the solid polymer [35, 36, 39]. The ex-

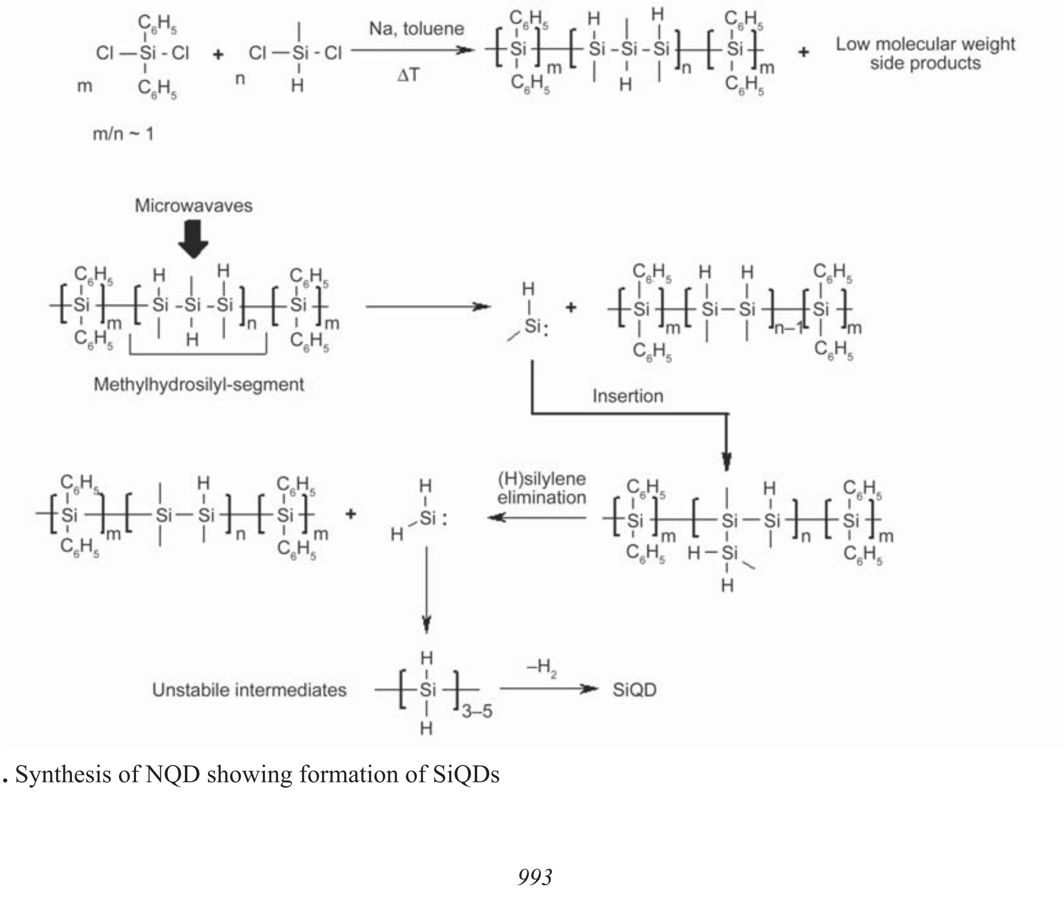

Figure 1. Synthesis of NQD showing formation of SiQDs

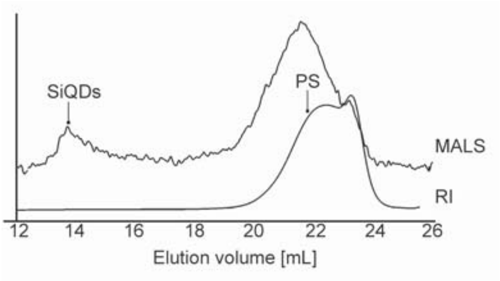

Figure 2. GPC comparison of MALS to RI traces that evidence existence of the SiQDs peak

istence of these nanoparticles can be also inferred from GPC analysis. Thus, beside the peak representing the polysilane molecular weight distribution, the MALS (multi angle light scattering) detector clearly evidenced another, unusual and low intensity peak at 14 mL elution volume. It is important to note that this peak is not detected by the refractive index (RI) detector (Figure 2). The difference should be related to the detection principle of the instruments. Since the low intensity peak is present only in MALS trace then the best guess is to assign it to the presence of solid particles within the liquid sample flow. Further investigations were meant to ascertain their specific characteristics as SiQDs.

In this regard, the TEM images provided clarifying details concerning the thin layer of the composite. Thus, well-defined nanoparticles dispersed within the bulk material can be noticed at high magnification (Figure 3). The nanoparticles were spherical and polydisperse, with average dimensions within the 3–30 nm range (Figure 3b). STEM images showed that the particles are compact, with an even distribution of highly dense material in all directions (Figure 4). Obviously, the particles are covered by a polysilane layer. However, the EDX line profile analysis indicates that, compared with the background, silicon is the main constitutive element of the observed nanoparticles. Furthermore, in order to have insights concerning the particle structure, the selected-area electron diffraction (SAED) pattern was investigated (Figure 4b). Thus, there are three diffraction rings that confirm the crystalline nature of the nanoparticles.

The disadvantage of TEM imaging is that it shows details on a very small fraction of the sample which is deposed on the grid surface. In order to obtain more reliable information the average dimensions and shape of the SiQDs in NQD colloidal dispersion were determined by SAXS analysis. Diluted samples of NQD have been submitted to X-ray exposure.

The collected 2D patterns were further reduced by azimuthal integration to 1D plots where the intensity of the scattering, *I*, is printed versus the momentum transfer vector, *q* (Figure 5). It is known that the scattering intensity *I*(*q*) is related to the averaged ensemble form of the particles. The intraparticle effects can be described by the so called form factor *P*(*q*), while the interparticle ones effects can be expressed by the structure factor *S*(*q*).

In the case of diluted systems, *S*(*q*) could be neglected. Both *P*(*q*) and *S*(*q*) are interrelated and described by the variation of scattering intensity with the mo-

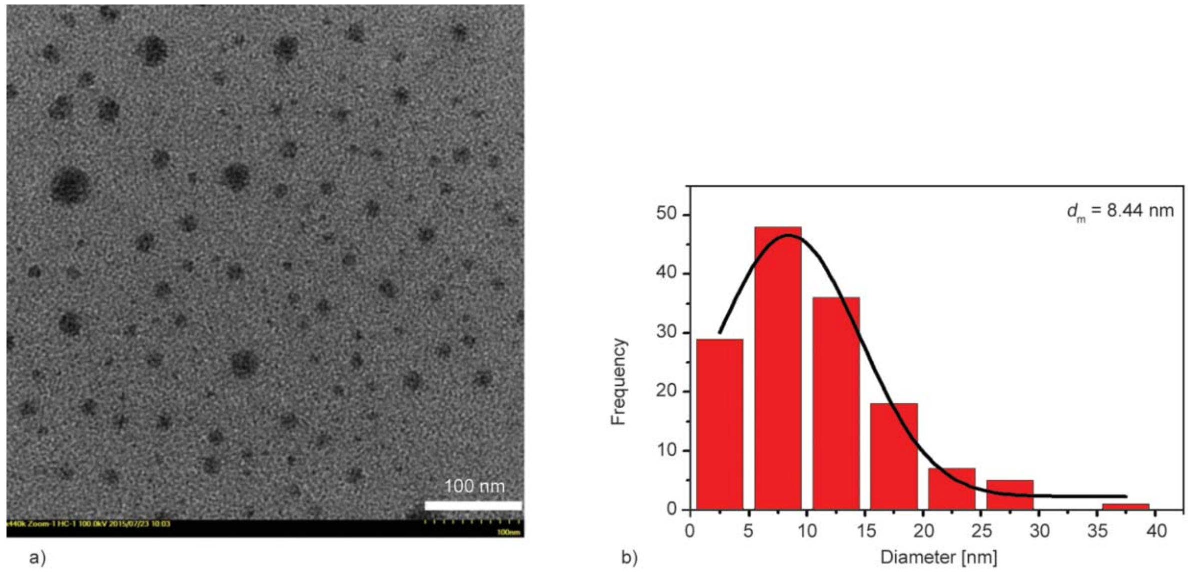

Figure 3. TEM high contrast image showing the presence of SiQD in polysilane (a); SiQDs size distribution histogram and fitted curve showing the average diameter (b)

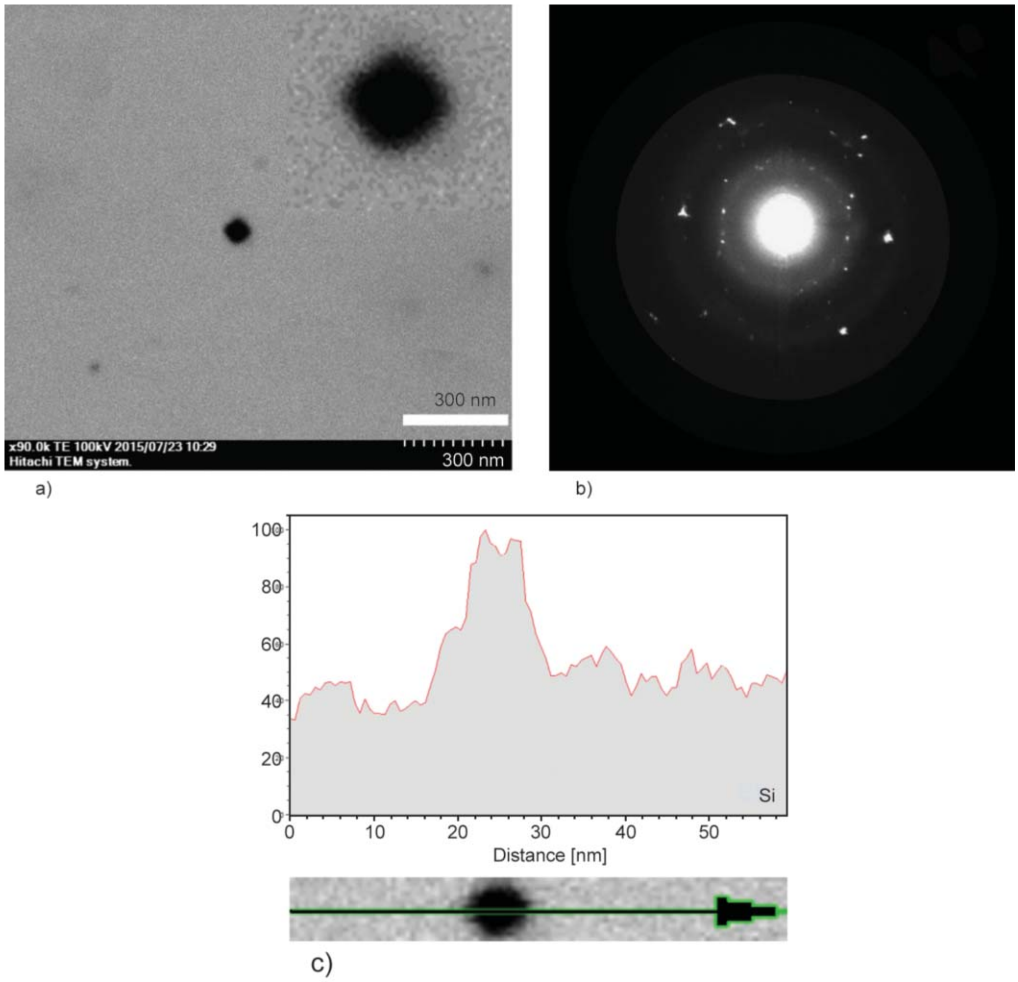

a)

b)

c)

Figure 4. STEM image in bright field detection showing the compact structure of SiQD (a); SAED pattern showing the characteristic three rings (b); EDX analysis, line profile comparison of the silicon content in SiQD versus background (c)

mentum transfer vector, q [41]. In the region of small scattering angles, the form factor $P(q)$ can be approximated by a Gaussian curve. According to Guinier, this particular part of the curve is related to the overall size of the particles and can be used to calculate their radius of gyration (R_g) [42]. Thus, R_g is the slope determined by the strait-line fitting in the graphical representation of the ln(I) versus q^2 (Figure 6) according to Equation (1):

$$\ln I(q) = \ln a_0 - \frac{R_g^2 q^2}{3} \tag{1}$$

R_g is the size parameter and it is model independent, and ao is the extrapolated zero angle intensity. The result obtained through this approach was R_g = 24.5 Å. Since the TEM-STEM analysis showed that the particles are quite homogeneous and of spherical shape, then the average diameter of the SiQDs in real

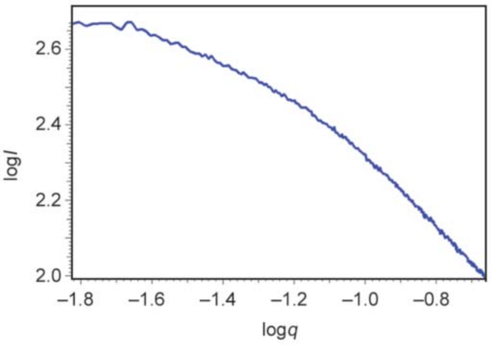

Figure 5. Scattering curve of NQD solution sample in logarithmic plot

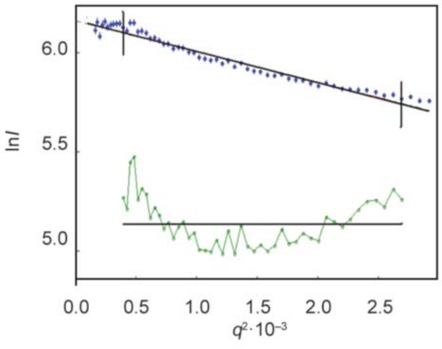

Figure 6. Guinier plot of the scattering intensity for NQD samples in solution

space calculated using Equation (2) is $D_{\max} = 6.3$ nm.

$$D_{\max} = 2\left(\frac{5}{3}\right)^{1/2} R_g \qquad (2)$$

Further interpretation of the SAXS results intended to tentatively reveal the origin of the high stability of the SiQDs colloidal solution. Such extremely stable colloidal dispersions of nanoparticles are normally obtained by using additional stabilizing agents. Because no stabilizing agents are necessary for the NQD dispersions, it was hypothesized that part of the polysilane chains are physically adsorbed onto the SiQDs surface, thus preventing their aggregation and separation.

In order to verify this hypothesis by SAXS, the model approach data analysis is usually done with the appropriate software. DIFFRAC$^{\text{plus}}$ NanoFit is an interactive graphics-based, non-linear least-squares data analysis program for one-dimensional SAXS data. This data evaluation software attempts modelling of small-angle scattering data from systems showing short-range order only and isotropic scattering spectra, so that the scattering intensity is only a function of the modulus of the scattering vector. The 2D intensity distribution in reciprocal space is further processed in order to obtain the corresponding real-space structure. The model in which scatterers are spherical particles containing a dense core and an envelope of polymeric chains is a perfect fit for the aforementioned hypothesis. The mathematical expressions describing such a structure have been derived by Pedersen [43] see Equation (3):

$$P(q) = \frac{1}{M^2}\left[\rho_s^2 F_1^2(q,R) + N_c \rho_c^2 P_{GP}^2(q,L) + \right. \\ \left. + N_c(N_c - 1)\rho_c^2 S_{cc}(q) + 2N_c \rho_s \rho_c S_{cc}(q)\right] \qquad (3)$$

with $S_{cc}(q)$ described by Equation (4):

$$S_{cc}(q) = F_1(q,R)\psi(q,R_g)\left[\frac{\sin\left(q\left(R + dR_g\right)\right)}{q\left(R + dR_g\right)}\right]^2 \qquad (4)$$

In this relation:

$M = \rho_s + N_c\rho_c$ is the scattering mass, where N_c is the number of chains, ρ_s is the total excess scattering length of the core and ρ_c is the total excess scattering length of a corona chain. Non-penetration of the chains into the core region is mimicked by $d \approx 1$ for $R \gg R_g$; R_g is the root-mean-square radius of gyration; $F_1(q,R)$ is the form factor amplitude of a homogeneous sphere; $P_{GP}(q)$ is the form factor of a Gaussian chain; $\psi(q,R_g) = [1 - \exp(-u)]/u$; $u = R_g^2q^2$.

A fitting of the experimental scattering curve with the calculated plot (Figure 7) shows the perfect match with the proposed model. In addition, further insight on the internal structure of the scatterers has been obtained. Thus, the radius of the dense core of SiQDs was determined to be $R = 2.8$ nm. Also, the radius of gyration corresponding to the polymeric chains adsorbed onto solid surface is $R_c = 1.6$ nm, which confirms the presence of polysilane onto the particle surface. Looking at the SiQDs diameter, as calculated by this model, one should observe that this value is quite similar to that obtained by the free model approach [$D_{\max(\text{model})} = 2\cdot 2.8 = 5.6$ nm]. The difference between the values obtained using each model comes from the polydispersity of the nanoparticles, which was not considered in the first method. In conclusion, SAXS results indicate that both the thin films and the solutions of NQD contain SiQDs as solid nanoparticles of spherical shape and sizes with an average maximum around 6 nm. The SiQDs particles are covered by a thin layer of polymer of about 2 nm thick, which prevents SiQDs aggregation in solution and leads to highly stable colloidal dispersions.

Further experiments investigated the fluorescence of NQD in the presence of CTP.

Diaryl-substituted pyridine derivatives are bioisosteres of terpyridine that are known to exhibit a strong cytotoxicity against several human cancer cell lines through the inhibition of topoisomerase I [44–48]. An analog of such diaryl-substituted pyridines (CTP) was synthesized using 3-dimethylamino-1-(thiophen-2-yl)-1-propanone hydrochloride **1** (a ke-

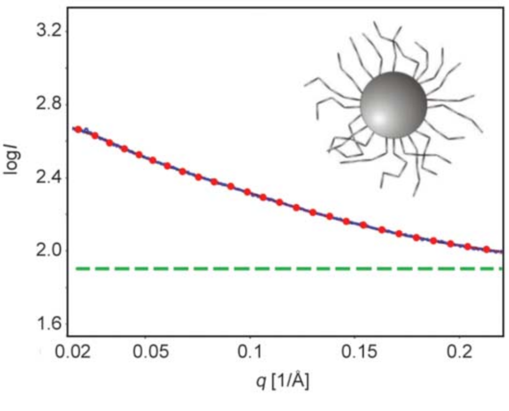

Figure 7. Correlation of the scattering curve between experimental and calculated (doted) showing the perfect mach with the assumed theoretical model

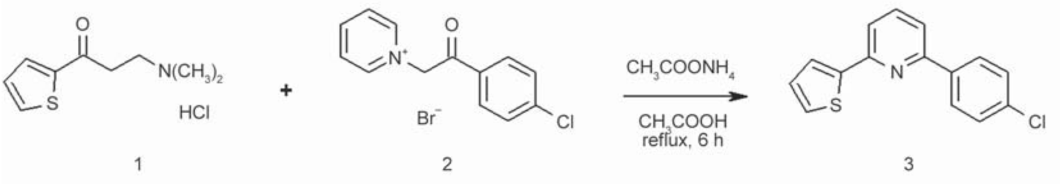

Figure 8. Synthesis of 2-(4-chlorophenyl)-6-(thiophen-2-yl)pyridine 3 (CTP)

tonic Mannich base), 4-chlorophenacylpyridinium bromide **2** and ammonium acetate as starting materials in an one-pot approach (Figure 8). The reaction sequence comprises the addition of the cycloimmonium salt to the α,β-unsaturated ketone thermally generated *in situ* from the ketonic Mannich base to yield a 1,5-diketone, whose subsequent ring closure in the presence of ammonium acetate leads to the desired pyridine derivative [37]. Treatment of a chloroform solution of the crude reaction product with charcoal followed by recrystallization from ethanol of the recovered solid afforded colourless 2-(4-chlorophenyl)-6-(thiophen-2-yl)pyridine 3 (CTP).

4.2. Spectroscopy of CTP

The CTP structure features an electron-acceptor moiety, namely the pyridine ring, linked to an electron-donor moiety, *i.e*. the thiophene ring. Starting from this prototype, similar molecules containing electron-donor and -acceptor units in their structure can be further tailored with a view to obtain lower bandgap, broader absorption, and higher mobility of charges. As the number of reports dealing with the florescence of CTP analogs is scarce, we first examined the photophysical properties of this compound. The study was also required in order to understand the origin of the electronic transitions involved in the emission process.

The UV-vis absorption spectrum of CTP as 0.01% solution in xylenes is shown in Figure 9. The compound has a broad and intense absorption in the range of 290 to 350 nm. The profile of the absorption presents a well-defined maximum at 321 nm, a barely visible shoulder at 302 nm and finally a large wide shoulder centered at 292 nm. The absorption maximum located at 302 nm could be assigned to the π–π* electron transitions within the conjugated thiophene–pyridine system. On the other hand, the 321 nm absorption band results from an intramolecular charge transfer which is specific for fluorescent compounds with electron-donor and -acceptor units in their structure.

The emission spectrum of CTP was measured by excitation around the determined absorption maxima. Irrespective of the excitation wavelength, the corresponding fluorescence (FL) spectrum showed only a single emission band centered at 368 nm. The highest intensity was obtained for an excitation wavelength of 321 nm, and this band was assigned to the emission of the first singlet excited state, S1 (fluorescence).

4.3. Spectroscopy of NQD

Polyhydrosilane presents in its structure numerous phenyl rings that are linked directly to the silicon backbone of the copolymer. The strong effects due to interactions at the level of the excited states between these aromatic rings and the silicon-based chain of the copolymer will determine the material's photophysical properties, which could be further exploited at molecular level. The UV-vis absorption spectrum of NQD is presented in Figure 10. As expected, a large shoulder is noticeable at approximately 310 nm, and its presence in the spectrum has been

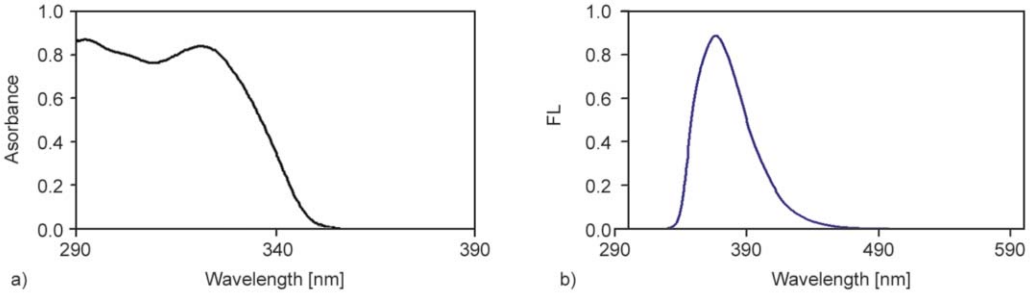

Figure 9. UV-vis absorption spectrum of CTP (a); FL spectrum of CTP. Excitation was done at 321 nm, (b)

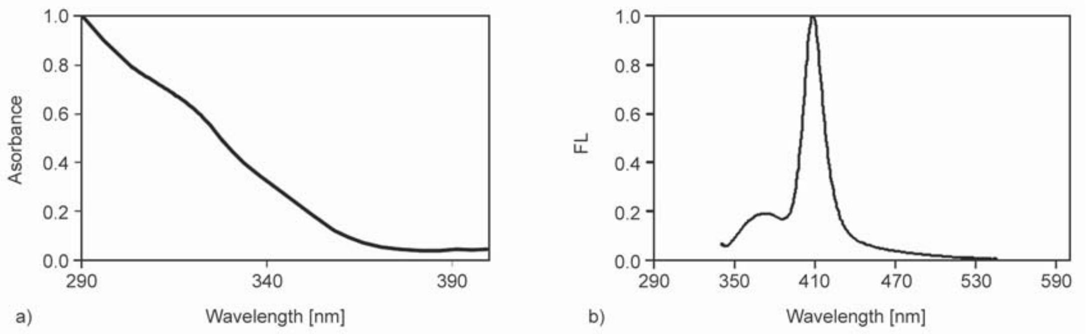

Figure 10. UV-vis spectrum of NQD (a); FL spectra of NQD. Excitation at 330 nm, (b)

associated with the transitions of the σ electrons in the polyhydrosilane matrix. A characteristic feature of polyhydrosilanes is the low resolution of the UV absorption maximum compared with other polysilanes structures. This specific profile is a consequence of the additional segmentation of the linear conjugated chain induced by the more flexible methylhydrosilyl moieties [36, 40, 49].

Excitation around the absorption maximum wavelength leads to the emission profile displayed in Figure 10b. The FL spectrum presented two emission bands. First, there is an expected broad emission band at 370 nm that was assigned to the σ–σ* electrons relaxation specific for the σ conjugated polysilanes. Second, another narrow emission peak with a much higher intensity is present at 410 nm. According to previous reports, this emission is characteristic for the SiQDs with dimensions below 10 nm [50, 51]. It is important to note that the highest intensity of the SiQDs emission was obtained by excitation at 330 nm, the same wavelength as for the polysilane structure.

4.4. Effect of CTP on NQD

UV-vis analysis of colloidal NQD samples having concentrations of CTP within 0.1–1% range has been performed with a view to establish the working limit. Thus, it was noted that for concentrations higher than 0.2%, the stronger absorption of CTP totally conceals the absorption of NQD. Below this value, the UV absorption spectrum shows elements common to both NQD and CTP UV spectra (Figure 11). On one hand, the overall aspect of the UV spectrum of stained NQD is similar to that of the pristine NQD, having just one large, barely noticeable shoulder. On the other hand, the absorption maximum recorded for stained NQD has shifted from 310 nm (as it was in the case of NQD) to 321 nm (as it was recorded for CTP). The probable cause of these modifications is the overlapping of electron transitions having similar energy gap for both NQD and CTP, which in turn affects the corresponding excited states. Interaction of polyhydrosilanes with the neighbouring electroactive species is a consequence of the intramolecular weak charge-transfer structures along the unshielded methyhydrosilyl segments [52]. The presence of CTP molecules in the immediate vicinity of polyhydrosilane leads to an extension of the σ electrons conjugated system through coupling with the dual π conjugated system of CTP. In addition, the presence of phenyl groups attached to the polysilane backbone contributes to a lowering of the band gap energy through σ–π conjugation. This also generates particular excited states, which are involved in electron

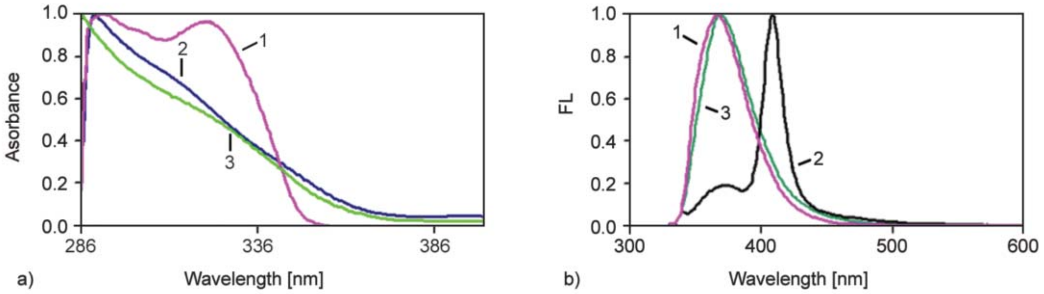

Figure 11. (a) Comparison between the UV absorption spectra of CTP (1), NQD (2) and stained NQD (3); (b) Comparison between the FL emission spectra of CTP (1), NQD (2) and stained NQD (3)

transition processes at both intra- and intermolecular levels [21].

The FL spectrum of stained NQD shows a single emission band at 370 nm for excitation wavelengths within the 310–330 nm range (Figure 11b). Interestingly, the emission profile of stained NQD is similar to that of pristine CTP, and not to the emission profile of NQD.

Another important observation is that a very small concentration of TCP ($0.33\cdot10^{-7}$ M) induced the suppression of SiQDs fluorescence emission up to 29.7%, meanwhile upon addition of $2.33\cdot10^{-7}$ M the fluorescence is quenched with 76.4% (Figure 12a).

Generally, the fluorescence quenching represents the decrease of the quantum yield of fluorescence from the fluorophore induced by different molecular interactions with the quencher molecule (energy transfer, excited-state reaction, molecules rearrangement, ground state complex formation, collision quenching) and also the quenching mechanism can be static or dynamic. Here, in order to elucidate the mechanism of quenching, we employed the well-known Stern-Volmer Equation (5) and modified Stern-Volmer Equation (6) [53]:

$$\frac{I_0}{I} = 1 + K_{\mathrm{SV}}[Q] \tag{5}$$

$$\frac{I_0}{(I_0 - I)} = \frac{1}{f_{\mathrm{a}}} + \frac{1}{f_{\mathrm{a}} k_{\mathrm{a}}[Q]} \tag{6}$$

where I_0 and I are the values of initial fluorescence intensities and in the presence of a quencher, respectively, $[Q]$ is the quencher concentration, K_{SV} is the Stern-Volmer dynamic quenching constant, ka is the fraction of accessible fluorescence and f_{a} is the effected quenching constant for the accessible fluorophores.

The Stern-Volmer plot of NQD in presence of TCP is shown in Figure 12b. It could be noted that the plot is linear, indicating that the quenching mechanism is probably single quenching [53, 54]. Moreover, the curve of $I_0/(I_0 - I)$ versus $1/[Q]$ was also linear for the TCP concentrations used in the study (Figure 12c). Both these obviously represent characteristics of a static quenching mechanism [53, 55].

A system exhibiting this behavior could be used to build multi-channel sensing devices. Thus, the NQD-based sensor will emit an intense signal at 370 nm when in contact with trace amounts of CTP. In the absence of CTP, a different signal will be emitted at 410 nm. Both signals can be generated using the same excitation wavelength, namely 330 nm. In any of these cases, the emission could be collected and used to trigger a specific response. This approach

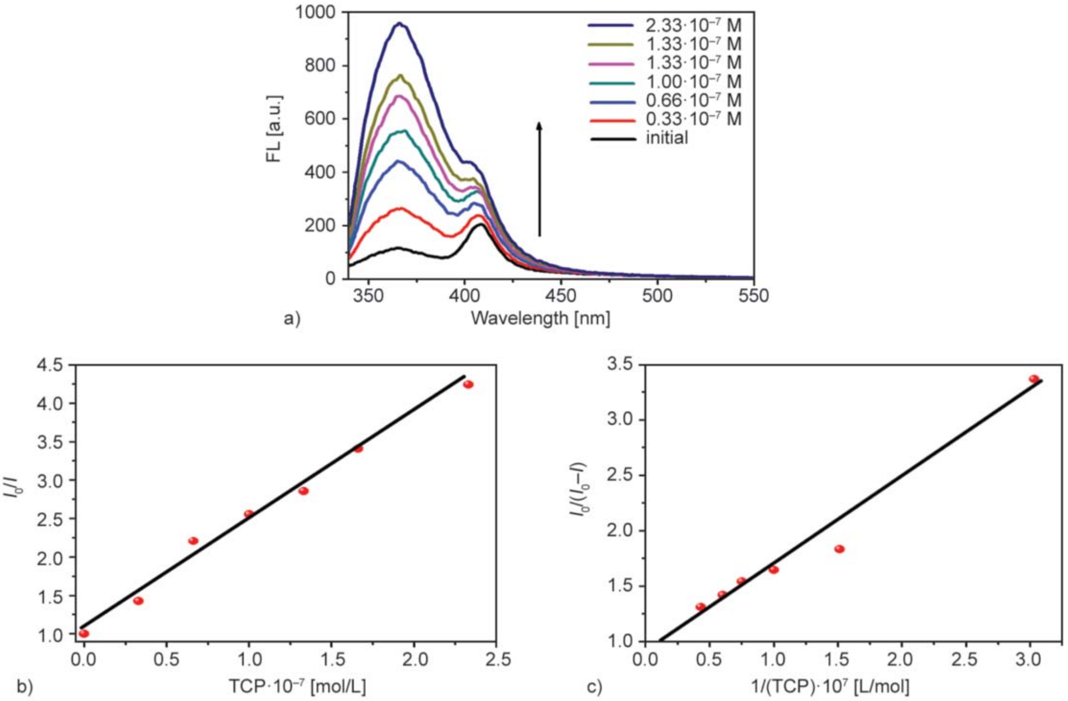

Figure 12. Influence of TCP on the fluorescence intensity of SiQDs (a); Stern-Volmer plot (b) and modified Stern-Volmer plot (c) showing the concentration effect of TCP

opens new opportunities to develop complex, high resolution imaging/sensing systems designed to increase anticancer therapy efficiency.

5. Conclusions

This work describes the sensing properties of a nanocomposite obtained by microwaves-assisted Wurtz coupling of methyldichlorosilane with diphenyldichlorosilane. The material is a solid powder containing SiQDs dispersed in a polysilane matrix soluble in usual organic solvents. Upon dissolution, indefinitely stable colloidal solutions of SiQDs are obtained. Thin films cast from such solutions were analyzed by TEM, and showed the presence of SiQDs dispersed within the polysilane thin film. The remarkable stability of the NQDs colloidal dispersion has been explained using SAXS. Thus, it was found that the spherical silicon nanoparticles are covered with a thin layer of polymer that prevents their aggregation and sedimentation. Further experiments explored the changes induced to the fluorescence of colloidal SiQDs by the presence of CTP, a potential cytotoxic agent. It was found that the SiQDs strong emission is totally quenched if low amounts of CTP are present. Since CTP has his own fluorescence, its combination with colloidal SiQDs results in a dual channel sensing system activated by a single excitation wavelength. The system could find application in tumour imaging and therapy.

References

[1] Berger C., Song Z., Li T., Li X., Ogbazghi A. Y., Feng R., Dai Z., Marchenkov A. N., Conrad E. H., First P. N., de Heer W. A.: Ultrathin epitaxial graphite: 2D electron gas properties and a route toward graphene-based nanoelectronics. Journal of Physical Chemistry B, **108**, 19912–19916 (2004).
DOI: 10.1021/jp040650f

[2] Banerjee S. K., Register L. F., Tutuc E., Reddy D., MacDonald A. H.: Bilayer pseudospin field-effect transistor (BiSFET): A proposed new logic device. IEEE Electron Device Letters, **30**, 158–160 (2009).
DOI: 10.1109/LED.2008.2009362

[3] Cavin R. K., Zhirnov V. V., Herr D. J. C., Avila A., Hutchby J.: Research directions and challenges in nanoelectronics. Journal of Nanoparticle Research, **8**, 841–858 (2006).
DOI: 10.1007/s11051-006-9123-4

[4] Li L., Deng L.: Random lasers in dye-doped polymer-dispersed liquid crystals containing silver nanoparticles. Physica B: Condensed Matter, **407**, 4826–4830 (2012).
DOI: 10.1016/j.physb.2012.09.023

[5] Skirtach A. G., Dejugnat C., Braun D., Susha A. S., Rogach A. L., Parak W. J., Möhwald H., Sukhorukov G. B.: The role of metal nanoparticles in remote release of encapsulated materials. Nano Letters, **5**, 1371–1377 (2005).
DOI: 10.1021/nl050693n

[6] Li S., Lin M. M., Toprak M. S., Kim D. K., Muhammed M.: Nanocomposites of polymer and inorganic nanoparticles for optical and magnetic applications. Nano Reviews, **1**, 5214/1–5214/19 (2010).
DOI: 10.3402/nano.v1i0.5214

[7] Ahirwal G. K., Mitra C. K.: Direct electrochemistry of horseradish peroxidase-gold nanoparticles conjugate. Sensors, **9**, 881–894 (2009).
DOI: 10.3390/s90200881

[8] Murray R. W.: Nanoelectrochemistry: Metal nanoparticles, nanoelectrodes, and nanopores. Chemical Reviews, **108**, 2688–2720 (2008).
DOI: 10.1021/cr068077e

[9] Gómez-Herrero J., Zamora F.: Coordination polymers for nanoelectronics. Advanced Materials, **23**, 5311–5317 (2011).
DOI: 10.1002/adma.201101952

[10] Han J., Ji Q., Qiu S., Li H., Zhang S., Jin H., Li Q.: A versatile approach to obtain a high-purity semiconducting single-walled carbon nanotube dispersion with conjugated polymers. Chemical Communications, **51**, 4712–4714 (2015).
DOI: 10.1039/C5CC00167F

[11] Gui R., Jin H., Wang Z., Tan L.: Recent advances in synthetic methods and applications of colloidal silver chalcogenide quantum dots. Coordination Chemistry Reviews, **296**, 91–124 (2015).
DOI: 10.1016/j.ccr.2015.03.023

[12] Knoblauch C., Griep M., Friedrich C.: Recent advances in the field of bionanotechnology: An insight into optoelectric bacteriorhodopsin, quantum dots, and noble metal nanoclusters. Sensors, **14**, 19731–19766 (2014).
DOI: 10.3390/s141019731

[13] Kodriano Y., Schmidgall E. R., Benny Y., Gershoni D.: Optical control of single excitons in semiconductor quantum dots. Semiconductor Science and Technology, **29**, 053001/1–053001/24 (2014).
DOI: 10.1088/0268-1242/29/5/053001

[14] Holmström P., Thylén L.: Electro-optic switch based on near-field-coupled quantum dots. Applied Physics A, **115**, 1093–1101 (2014).
DOI: 10.1007/s00339-014-8420-5

[15] Cheng X., Hinde E., Owen D. M., Lowe S. B., Reece P. J., Gaus K., Gooding J. J.: Enhancing quantum dots for bioimaging using advanced surface chemistry and advanced optical microscopy: Application to silicon quantum dots (SiQDs). Advanced Materials, **27**, 6144–6150 (2015).
DOI: 10.1002/adma.201503223

[16] Montalti M., Cantelli A., Battistelli G.: Nanodiamonds and silicon quantum dots: Ultrastable and biocompatible luminescent nanoprobes for long-term bioimaging. Chemical Society Reviews, **44**, 4853–4921 (2015).
DOI: 10.1039/C4CS00486H

[17] Campos B. B., Algarra M., Alonso B., Casado C. M., Jiménez-Jiménez J., Rodríguez-Castellón E., Esteves da Silva J. C. G.: Fluorescent sensor for Cr(VI) based in functionalized silicon quantum dots with dendrimers. Talanta, **144**, 862–867 (2015).
DOI: 10.1016/j.talanta.2015.07.038

[18] Peng X., Long Q., Li H., Zhang Y., Yao S.: 'Turn on-off' fluorescent sensor for protamine and heparin based on label-free silicon quantum dots coupled with gold nanoparticles. Sensors and Actuators B: Chemical, **213**, 131–138 (2015).
DOI: 10.1016/j.snb.2015.02.070

[19] Brus L.: Luminescence of silicon materials: Chains, sheets, nanocrystals, nanowires, microcrystals, and porous silicon. Journal of Physical Chemistry, **98**, 3575–3581 (1994).
DOI: 10.1021/j100065a007

[20] Kitao T., Bracco S., Comotti A., Sozzani P., Naito M., Seki S., Uemura T., Kitagawa S.: Confinement of single polysilane chains in coordination nanospaces. Journal of the American Chemical Society, **137**, 5231–5238 (2015).
DOI: 10.1021/jacs.5b02215

[21] Sacarescu L., Kostromin S., Bronnikov S.: Synthesis and properties of polydiphenylsilane/fullerene C_{60} nanocomposites. Materials Chemistry and Physics, **149–150**, 430–436 (2015).
DOI: 10.1016/j.matchemphys.2014.10.041

[22] Okazaki A., Akita S., Nakayama Y.: Nanolithography of organic polysilane films using carbon nanotube tips – Application to the etching process. Physica B: Condensed Matter, **323**, 151–152 (2002).
DOI: 10.1016/S0921-4526(02)00884-0

[23] Srinivasan R.: Ablation of polymers and biological tissue by ultraviolet lasers. Science, **234**, 559–565 (1986).
DOI: 10.1126/science.3764428

[24] Miller R. D., Wallraff G. M., Clecak N., Sooriyakumaran R., Michl J., Karatsu T., McKinley A. J., Klingensmith K. A., Downing J.: Polysilanes: Photochemistry and deep UV lithography. Polymer Engineering and Science, **29**, 882–886 (1989).
DOI: 10.1002/pen.760291311

[25] Hasegawa T., Iwasa Y., Sunamura H., Koda T., Tokura Y., Tachibana H., Matsumoto M., Abe S.: Nonlinear optical spectroscopy on one-dimensional excitons in silicon polymer, polysilane. Physical Review Letters, **69**, 668–671 (1992).
DOI: 10.1103/PhysRevLett.69.668

[26] Tang H., Liu Y., Huang B., Qin J., Fuentes-Hernandez C., Kippelen B., Li S., Ye C.: Synthesis and optical properties of a series of chromophore functionalized polysilanes. Journal of Materials Chemistry, **15**, 778–784 (2005).
DOI: 10.1039/B413016B

[27] Tsukuda S., Seki S., Saeki A., Kozawa T., Tagawa S., Sugimoto M., Idesaki A., Tanaka S.: Precise control of nanowire formation based on polysilane for photoelectronic device application. Japanese Journal of Applied Physics, **43**, 3810–3814 (2004).
DOI: 10.1143/JJAP.43.3810

[28] Ardeleanu R., Mangalagiu I., Sacarescu G., Simionescu M., Sacarescu L.: Polysilane-cycloimmonium salts: New materials for organic semiconductors. Macromolecular Rapid Communications, **25**, 1231–1235 (2004).
DOI: 10.1002/marc.200400115

[29] Masuda T., Matsuki Y., Shimoda T.: Pyrolytic transformation from polydihydrosilane to hydrogenated amorphous silicon film. Thin Solid Films, **520**, 6603–6607 (2012).
DOI: 10.1016/j.tsf.2012.07.028

[30] Iyer G. R. S., Hobbie E. K., Guruvenket S., Hoey J. M., Anderson K. J., Lovaasen J., Gette C., Schulz D. L., Swenson O. F., Elangovan A., Boudjouk P.: Solution-based synthesis of crystalline silicon from liquid silane through laser and chemical annealing. ACS Applied Materials and Interfaces, **4**, 2680–2685 (2012).
DOI: 10.1021/am300334p

[31] Shimoda T., Matsuki Y., Furusawa M., Aoki T., Yudasaka I., Tanaka H., Iwasaki H., Wang D., Miyasaka M., Takeuchi Y.: Solution-processed silicon films and transistors. Nature, **440**, 783–786 (2006).
DOI: 10.1038/nature04613

[32] Sacarescu G., Sacarescu L., Ardeleanu R., Kurcok P., Jedliński Z.: Si–H functional polysilanes via a homogeneous reductive coupling reaction. Macromolecular Rapid Communications, **22**, 405–408 (2001).
DOI: 10.1002/1521-3927(20010301)22:6<405::AID-MARC405>3.0.CO;2-N

[33] Sacarescu L., Ardeleanu R., Sacarescu G., Simionescu M., Hurduc N.: Polydiphenylsilanes bearing photosensitive azocrown groups. Chemical Communications, **2006**, 788–789 (2006).
DOI: 10.1039/B514161C

[34] Sacarescu L., Ardeleanu R., Sacarescu G., Simionescu M., Mangalagiu I.: Polysilane–metal complexes for organic semiconductors. High Performance Polymers, **19**, 501–509 (2007).
DOI: 10.1177/0954008306081193

[35] Sacarescu L., Siokou A., Ardeleanu R., Sacarescu G., Simionescu M.: Low-temperature restructuring processes in polyhydrosilanes. Macromolecular Rapid Communications, **27**, 1054–1059 (2006).
DOI: 10.1002/marc.200600192

[36] Sacarescu L., Bockholt A., Siokou A., Simionescu M., Sacarescu G.: Structural and optical properties of polyhydrosilanes. Macromolecular Chemistry and Physics, **210**, 2015–2021 (2009).
DOI: 10.1002/macp.200900384

[37] Roman G.: Generation of a structurally diverse library through alkylation and ring closure reactions using 3-dimethylamino-1-(thiophen-2-yl)propan-1-one hydrochloride. Acta Chimica Slovenica, **60**, 70–80 (2013).

[38] Sacarescu G., Simionescu M., Harabagiu V., Sacarescu L.: Microwave-assisted Wurtz coupling of methylphenyldichlorosilane in solvent-free conditions. e-Polymers **12**, 145–150 (2012).
DOI: 10.1515/epoly.2012.12.1.145

[39] Sacarescu L., Siokou A., Sacarescu G., Simionescu M., Mangalagiu I.: Methylhydrosilyl chemostructural effects in polyhydrosilanes. Macromolecules, **41**, 1019–1024 (2008).
DOI: 10.1021/ma071853f

[40] Konarev P. V., Volkov V. V., Sokolova A. V., Koch M. H. J., Svergun D. I.: PRIMUS: a Windows PC-based system for small-angle scattering data analysis. Journal of Applied Crystallography, **36**, 1277–1282 (2003).
DOI: 10.1107/S0021889803012779

[41] Glatter O., Kratky O.: Small angle X-ray scattering. Academic Press, London (1982).

[42] Guinier A., Fournet G.: Small-angle scattering of X-rays. Wiley, New York (1955).

[43] Lindner P., Zemb T.: Neutrons, X-rays and light. Scattering methods applied to soft condensed matter. Elsevier, Amsterdam (2002).

[44] Kim D. S. H. L., Ashendel C. L., Zhou Q., Chang C-T., Lee E-S., Chang C-J.: Novel protein kinase C inhibitors: α-terthiophene derivatives. Bioorganic and Medicinal Chemistry Letters, **8**, 2695–2698 (1988).
DOI: 10.1016/S0960-894X(98)00468-5

[45] Zhao L-X., Kim T. S., Ahn S-H., Kim T-H., Kim E-K., Cho W-J., Choi H., Lee C-S., Kim J-A., Jeong T. C., Chang C-J., Lee E-S.: Synthesis, topoisomerase I inhibition and antitumor cytotoxicity of 2,2′:6′,2″-, 2,2′:6′,3″- and 2,2′:6′,4″-terpyridine derivatives. Bioorganic and Medicinal Chemistry Letters, **11**, 2659–2662 (2001).
DOI: 10.1016/S0960-894X(01)00531-5

[46] Zhao L-X., Moon Y-S., Basnet A., Kim E-K., Jahng Y., Park J. G., Jeong T. C., Cho W-J., Choi S-U., Lee C. O., Lee S-Y., Lee C-S., Lee E-S.: Synthesis, topoisomerase I inhibition and structure–activity relationship study of 2,4,6-trisubstituted pyridine derivatives. Bioorganic and Medicinal Chemistry Letters, **14**, 1333–1337 (2004).
DOI: 10.1016/j.bmcl.2003.11.084

[47] Zhao L-X., Sherchan J., Park J. K., Jahng Y., Jeong B-S., Jeong T. C., Lee C-S., Lee E-S.: Synthesis, cytotoxicity and structure-activity relationship study of terpyridines. Archives of Pharmacal Research, **29**, 1091–1095 (2006).
DOI: 10.1007/BF02969297

[48] Basnet A., Thapa P., Karki R., Na Y., Jahng Y., Jeong B-S., Jeong T. C., Lee C-S., Lee E-S.: 2,4,6-Trisubstituted pyridines: Synthesis, topoisomerase I and II inhibitory activity, cytotoxicity, and structure–activity relationship. Bioorganic and Medicinal Chemistry, **15**, 4351–4359 (2007).
DOI: 10.1016/j.bmc.2007.04.047

[49] Tarabukina E., Krasova A., Filippov A., Sacarescu L., Simionescu M., Sacarescu G., Soroceanu M., Harabagiu V.: Hydrodynamic and molecular characteristics of organosilane copolymers of low molecular weight. High Performance Polymers, **25**, 79–86 (2013).
DOI: 10.1177/0954008312456890

[50] Baldwin R. K., Pettigrew K. A., Ratai E., Augustine M. P., Kauzlarich S. M.: Solution reduction synthesis of surface stabilized silicon nanoparticles. Chemical Communications, **2002**, 1822–1823 (2002).
DOI: 10.1039/B205301B

[51] Kim T-Y., Park N-M., Kim K-H., Sung G. Y., Ok Y-W., Seong T-Y., Choi C-J.: Quantum confinement effect of silicon nanocrystals *in situ* grown in silicon nitride films. Applied Physics Letters, **85**, 5355–5357 (2004).
DOI: 10.1063/1.1814429

[52] Sacarescu L., Simionescu M., Sacarescu G., Hitruc E. G.: Photocatalytic synthesis of silver nanoparticles using polysilane initiator. Journal of Nanoparticle Research, **13**, 997–1005 (2010).
DOI: 10.1007/s11051-010-0120-2

[53] Lakowicz J. R.: Principles of fluorescence spectroscopy. Springer, New York (2006).

[54] Zhang H., Wang Y., Fei Z., Wu L., Zhou Q.: Characterization of the interaction between Fe(III)-2,9,16,23-tetracarboxyphthalocyanine and blood proteins. Dyes and Pigments, **78**, 239–247 (2008).
DOI: 10.1016/j.dyepig.2007.12.011

[55] Ware W. R.: Oxygen quenching of fluorescence in solution: An experimental study of the diffusion process. Journal of Physical Chemistry B, **66**, 445–458 (1962).
DOI: 10.1021/j100809a020

eXPRESS Polymer Letters Vol.10, No.12 (2016) 1003–1015
Available online at www.expresspolymlett.com
DOI: 10.3144/expresspolymlett.2016.93

Printing continuously graded interpenetrating polymer networks of acrylate/epoxy by manipulating cationic network formation during stereolithography

W. Li[1], M. Bakhtiary Noodeh[1], N. Delpouve[2], J.-M. Saiter[3], L. Tan[1], M. Negahban[1*]

[1]Mechanical & Materials Engineering, University of Nebraska-Lincoln, NE 68588-0526, USA
[2]AMME-LECAP International Lab, University of Rouen, France
[3]Institute for Materials Research, University of Rouen, France

Received 3 May 2016; accepted in revised form 20 July 2016

Abstract. Ultra-violet (UV) laser assisted stereolithography is used to print graded interpenetrating polymer networks (IPNs) by controlling network formation. Unlike the traditional process where structural change in IPNs is achieved by varying the feeding ratio of monomers or polymer precursors, in this demonstration property is changed by controlled termination of network formation. A photo-initiated process is used to construct IPNs by a combination of radical and cationic network formation in an acrylate/epoxy system. The extent of the cationic network formation is used to control the final properties of the system. Rapid-Scan Fourier Transformation Infrared Spectroscopy (RS-FTIR) is used to track the curing kinetics of the two networks and identify key parameters to control the final properties. Atomic force microscopy (AFM) and differential scanning calorimetry (DSC) confirm the formation of homogenous IPNs, whereas nano-indentation indicates that properties vary with the extent of cationic network formation. The curing characteristics are used to design and demonstrate printing of graded IPNs that show two orders of magnitude variation in mechanical properties in the millimeter scale.

Keywords: *polymer blends and alloys, interpenetrating polymer networks, functionally graded materials, mechanical properties, photo curing*

1. Introduction

The control of material properties, and in particular the development of functionally graded materials (FGMs), is one of the frontiers of current design and manufacturing [1, 2]. Nature, through the process of evolution, normally selects materials that better fit their application and frequently arrives at designs that perform their task through grading. This, for example, is how a soft-bodied squid can manipulate a hard beak [3]. The use of FGMs in nature is more the norm than the exception and is seen in practically every system, such as in plant stems, shells, teeth, and bone [4]. Similar advantages can be achieved in manufactured parts if one can manufacture functionally designed graded properties. In mechanical systems, such as composites, grading can be used to remove discrete interfaces and result in the distribution of stresses [5, 6]. This can help to reduce stress concentration at critical locations and suppress the onset of permanent (plastic) deformation, damage, or cracking [7–10]. Smooth transitions in composition across an interface can also improve interfacial bonding between dissimilar materials [4, 11–13]. To design and manufacture FGM parts, one needs a flexible platform to create controlled grading without introducing discrete interfaces.

One way to control properties in a macromolecular system is to use interpenetrating polymer networks

---

[*]Corresponding author, e-mail: mnegahban@unl.edu

(IPNs). IPNs have already been used in many applications [14–18]. IPNs are polymer systems that are formed from two or more networks in close proximity in a manner to achieve modulation of their physical properties by interpenetration of their individual networks [19, 20]. The same networks can produce IPNs with different properties by changing the fraction of each network in the system [14, 18]. Thus, a spatial variation of the fraction of the networks in IPNs can be used to create grading [1, 21, 22].

IPNs normally expresses characteristics that are between those of the individual constructing networks [23]. By properly selecting the mixture (i.e., the ratio and type) of the components constructing IPNs, one can make different IPNs that can have properties ranging from a soft rubber to a hard glassy material [24, 25]. This suggests that one can get large grading in IPNs by selecting appropriate networks and by varying their ratio in space. One can achieve this, for example, by selecting long acrylate and short epoxy cross-linking oligomers to build the respective networks [26].

Polymer networks can be constructed by different curing methods such as thermal and photo curing [27]. Photo curing is typically fast and also controllable [28, 29], and has been the basis of numerous conventional applications in coatings, adhesives, inks, printing plates, optical wave guides, microelectronics and 3D printing [30]. Many IPNs, including acrylate/epoxy based IPNs, have been made by such a process [31–33].

The main mechanisms for photo curing of polymers are free-radical and ionic polymerization [30]. Typically, radical photo polymerization is fast and controllable as the radicals can be rapidly initiated by light and rapidly terminate in its absence. On the other hand, ionic photo polymerization is a living process that is slower and typically only terminates with the lack of availability of the monomer/crosslinker [34]. Acrylate is known to follow a radical process and epoxy a cationic process [27, 32, 35] and show a difference between their curing rates [36, 37]. A mixture containing acrylate and epoxy components during photo polymerization will have the networks growing concurrently, which should give simultaneous IPNs that typically are a more homogenous material and has better properties compared to sequential IPNs [20, 33, 38, 39].

The cationic process during photo polymerization is subject to continued curing after the termination of light exposure (dark curing) and continues as long as there is availability of the uncured component [40, 41]. The dark curing of a component that is following cationic polymerization, such as that for epoxy, can be controlled and terminated by changing the availability of the uncured fraction by a process such as washing with a solvent [42, 43]. The premature termination of the network formation of the cationic component in IPNs will result in a material with different properties [43, 44]. Spatial variation of the time of termination of the cationic component may result in one way to control the grading of IPNs.

An acrylate/epoxy system is considered for making graded IPNs by photo polymerization in a printer. The kinetics of IPNs formation are studied by Rapid-Scan Fourier Transformation Infrared Spectroscopy (RS-FTIR), and the characteristics of the IPNs are evaluated by optical microscopy, Differential Scanning Calorimetry (DSC), Atomic Force Microscopy (AFM), and nano-indentation. A printing process for making graded IPNs based on controlling the extent of dark curing is designed and implemented in a 3D printer, and the resulting grading is evaluated by nano-indentation.

2. Materials and methods

IPNs were prepared using a mixture of two photo initiated cross-linking components. Bisphenol A ethoxylate dimethacrylate (acrylate) and the photo initiator 2-Hydroxy-2-methylpropiophenone formed the component that follows radical polymerization. Bisphenol A diglycidyl ether (BADGE) and Triarylsulfonium hexafluoroantimonate salts, mixed 50 wt% in propylene carbonate, as the photo initiator are the component that follows cationic polymerization. All components were supplied by Sigma-Aldrich Co., USA. Figure 1 presents the chemicals that form the IPNs and their associated photo initiators. The acrylate oligomer used in this study has the repetition unit length of $n = m = 15$, and its molecular weight is $M_n \approx 1700$ g/mol.

The solution used for this study was made of 1 wt% of cationic initiator in solvent (propylene carbonate), 0.25 wt% of radical initiator, 49.375 wt% each of acrylate and BADGE. For simplicity, this is termed the 50/50 acrylate/BADGE mixture as it contains

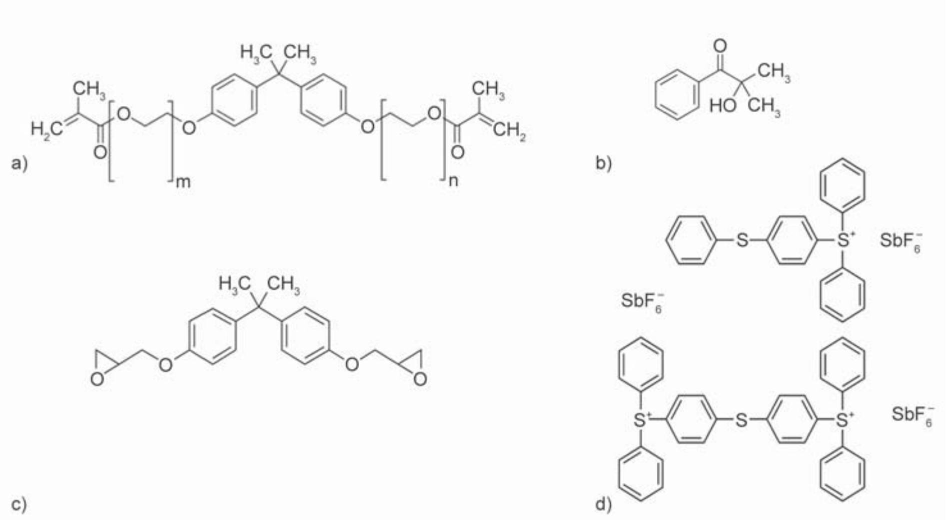

Figure 1. Chemical structures of (a) Bisphenol A ethoxylate dimethacrylate (b) 2-Hydroxy-2-methylpropiophenone, (c) Bisphenol A diglycidyl ether, and (d) Triarylsulfonium hexafluoroantimonate salts

equal part of the two monomers (oligomers). The components were mixed together by mechanical stirring (VWR, VMS C7 S1) at 2000 rpm for approximately 40 min under vacuum and kept under an inert Argon environment at 50±1 °C before photo polymerization.

The light attenuation of the system was evaluated by measuring the transmission of 322 nm light, produced by a tunable laser (Opotek, HE 355 LD, USA), through different thicknesses of the sample. The samples were put in cylindrical rings of different thickness that were set on a fused silica glass of 25 mm thickness. The power transmission was measured by a light power meter (Ophir thermal sensor, USA).

The curing kinetics of the mixtures was studied by Rapid-Scan FTIR (Agilent technologies, Cary 670) on a temperature-controlled Attenuated Total Reflectance (ATR; GladiATR, PIKE, USA) set, at 85±1 °C. As shown in Figure 2, a cylindrical container ring was used to hold the sample, of approximate film thickness of $h = 200\pm5$ μm, on the diamond sensor of the ATR. Photo curing was initiated under a controlled Argon atmosphere from the top of the sample by a collimated light. The light was produced by a tunable laser (Opotek, HE 355 LD, USA) set at 322 nm, which was connected by a UV optical fiber to a collimator aligned perpendicular to the top of the sample. The characteristic of the collimated beam was evaluated with a power meter and beam profile camera (Ophir thermal sensor, Ophir Spiricon camera). The laser was connected to the system by a fiber optic cable connected to a collimator that produced a uniform power distribution. The power distribution out of the collimator was measured by a

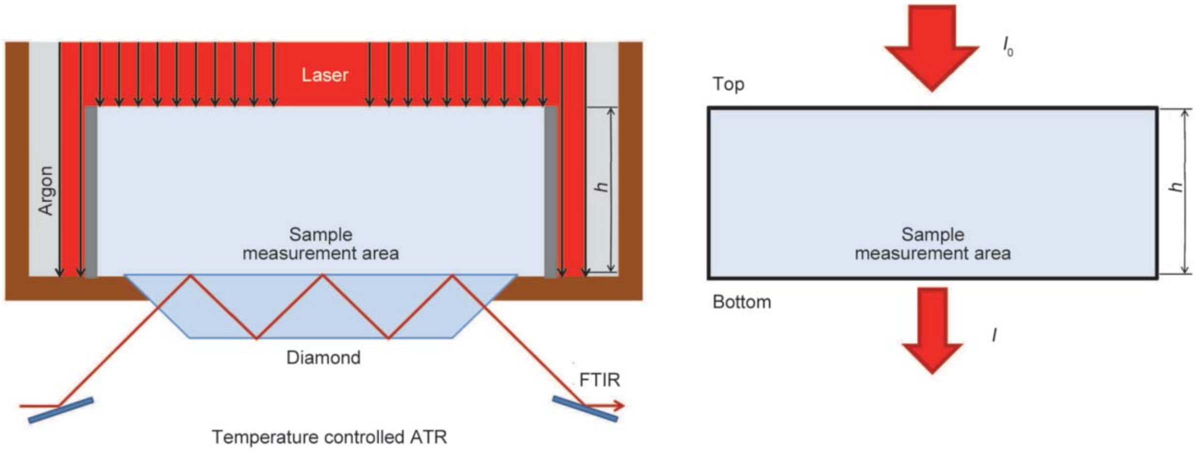

Figure 2. Schematic illumination of sample on environmentally controlled ATR setup for FTIR evaluation of curing kinetics at the bottom surface. The power of the collimated laser beam is I_0 at the top of the sample and is attenuated to I at the bottom where the measurement is done.

power meter (Ophir, USA). The FTIR used the MCT detector to analyze the material at the bottom of the sample (directly adjacent to the diamond of the ATR) over the range of 400–4000 cm^{-1} at a rate of 0.5 or 1 spectra per second with a spectra resolution of 4 cm^{-1}. The Beer-Lambert law was used to calculate the attenuation of the light power through the sample thickness to calculate the power intensity at the surface of the diamond (bottom of the sample) where the FTIR measurements were taken from.

The kinetics of curing for our system was evaluated from the FTIR spectra measured at the bottom sample surface, as shown in Figure 2, by monitoring the respective intensities of the different peaks. Typical initial and intermediate FTIR spectra during the curing are shown in Figure 3. The variable peaks at 1638 cm^{-1} (C=C) and 778 cm^{-1} (△) are, respectively, associated with the conversion of acrylate and BADGE [31]. Conversion of each component was calculated using the peak-height method based on the ratio of the height of the variable peak to the reference peak at 1607 cm^{-1}. This peak is one of the three reference peaks at 1510, 1580 and 1607 cm^{-1} of –C=C–H aromatic [45, 46].

Optical micrographs of the samples were taken using a Nikon Optiphot-2 Polarized Optical Microscope (POM) equipped with the Nikon Nis Elements D software. The pictures were obtained in both reflection and transmission modes, allowing picturing homogeneity of the material from the surface to the bulk.

Due to the small size of the samples prepared on the Rapid-San FTIR, DSC was performed on the cured samples using a twin-type power-compensation fast scanning chip calorimeter (Flash DSC 1, Mettler-Toledo, Switzerland). Micro-gram sized samples, including the full cross section, were taken from the center of the cured sample before post curing and were analyzed on MultiSTAR UFS 1 MEMS chip sensors. The positioning of the sample in the middle of the sensor was ensured using a Leica® optical microscopy tool. A Huber TC100 immersion cooler was used to cool samples to –80 °C before any measurement. Nitrogen purge gas (99.9% purity) was used at a flow rate of 20 mL·min^{-1} to avoid condensation of water from the environment. The Flash DSC analyses were carried after conditioning of the sensor at a heating rate β_h = 1500 K·s^{-1} from –70 to 250 °C.

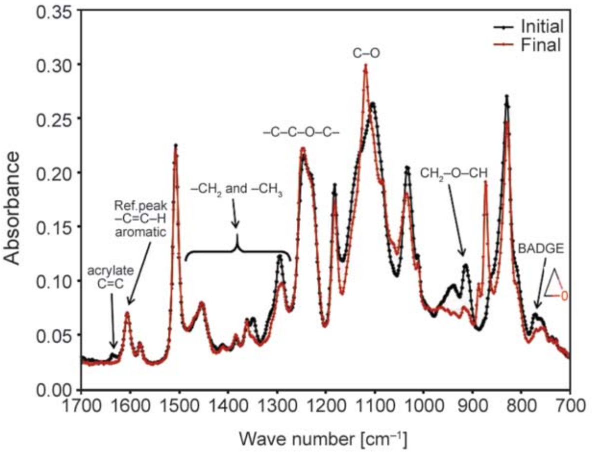

Figure 3. Typical initial and intermediate FTIR spectra from 700 to 1700 cm^{-1} of the acrylate/BADGE mixture

The mechanical property of each sample after the curing process was evaluated using nano-indentation (Hysitron, TI-950 Triboindenter, USA). The samples made on the ATR during Rapid-Scan FTIR were each evaluated at two points on the lower surface using each time nine measurements on a 3×3 grid of dimensions 0.7 by 0.5 mm. For the printed samples, 50 µm of the surface was removed before testing to avoid any surface-specific characteristics. This was done by first using 600 Grit sandpaper to roughly polish away around 50 µm (600 Grit ~30 µm), then synthetic velvet cloth and de-agglomerated alumina (300 nm) dispersion (BUEHLER) was applied to fine polish the surface. For the printed samples, measurements were taken on the centerline of the path of the traveling beam. Four measurements were made in each case on a 4×4 square grid of dimension 10 µm. The results were analyzed using standard analysis [47] for a conical tip (Ti-0093) in displacement control mode with maximum displacement of 500 nm. AFM (Anasys instrument, USA) was used in contact mode to study topology and phase angle in some samples.

The graded sample was made in a 3D printer. In the 3D printing machine, the printing head was installed with a focus lenses, which was connected with a silica UV optical fiber (1 mm diameter) to the same laser source and settings. A thermal heater was used on the sample platform to allowed vertical adjustment under the printer head. The temperature of the mixture on the platform was monitored by an IR beam thermometer. The 3D printing machine was controlled through G-code. The entire printing area was kept under an Argon atmosphere. The details of the printing process are described in the grading design included in the Discussion and Demonstration section.

3. Uniform curing results and discussion

Photo curing on the FTIR-ATR system and the later demonstration of graded curing required knowledge of the attenuation of light as it passes through the mixture. The attenuation of light in a homogeneous system is given by the Beer-Lambert law $I = I_0 \cdot \exp(-\xi h)$ [48, 49], where I is the transmitted power, I_0 is the incident power, ξ is the attenuation coefficient, and h is the thickness of material the light is transmitting through. The system used was a mixture of monomers (oligomers) and photo initiators as described above. For a homogeneous mixture, we can calculate the attenuation coefficient from Equation (1):

$$\xi = \sum_{i=1}^{n} x_i \xi_i \qquad (1)$$

where for n components, x_i is the concentration of component i, and ξ_i is its respective attenuation coefficient. The attenuation coefficients for the components of our mixture were evaluated by direct power transmission through a sequence of fixed thicknesses for each pair of monomer (oligomer) and photo initiator. The results are shown in Figure 4. The initial attenuation coefficients for the acrylate, radical photo initiator, epoxy, and cationic initiator (including solvent) where respectively evaluated as 0.12, 132.5, 0.09, and 1666 mm^{-1} by fitting linear regression lines to the data. For the final mixture used (respectively 1 and 0.25 wt% cationic and radical initiators), this gives the attenuation coefficient of the total system as $\xi = 17.1\ mm^{-1}$. This attenuation increases with the curing of the systems to about $\xi = 18.1\ mm^{-1}$ after 60 s.

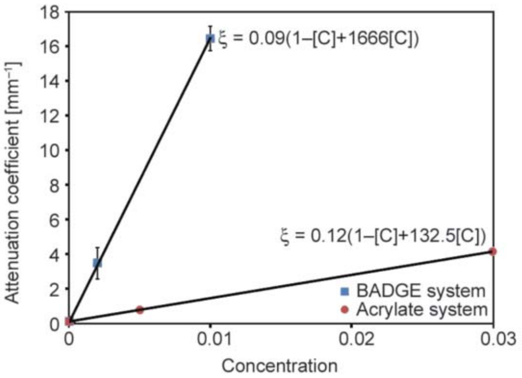

Figure 4. Attenuation coefficient of light as a function of concentration of initiators

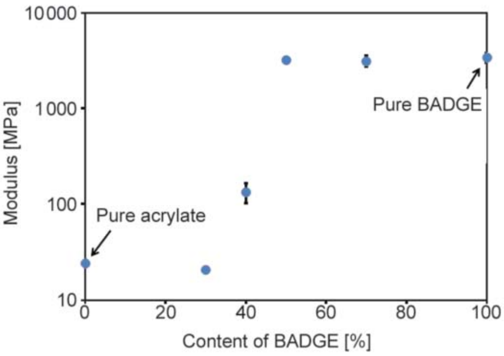

Figure 5. The dependence of modulus on the concentration of BADGE for a polychromatically cured system

Before the start of this work, the characteristics of the acrylate/BADGE system was studied by preparing and curing, under a polychromatic lamp, samples with different concentrations of BADGE. The modulus for these concentrations was evaluated by nanoindentation and indicated a lack of sensitivity of the modulus to changes in the concentration of BADGE above 50%, shown in Figure 5. This suggested use of the 50/50 acrylate/BADGE system selected here as it could provide both a high modulus and the modulus would be sensitive to reduction in BADGE content.

The effect of the duration of light exposure was studied for the 50/50 acrylate/BADGE mixture on a temperature controlled ATR attached to a rapid-scan FTIR as shown in Figure 2. The samples were exposed to light from 50 to 2400 s in an Argon atmosphere. Using the Beer-Lambert law, the power at the bottom of the sample, where the FTIR spectra are evaluated from, was calculated to initially be 0.245 mW/cm^2, which decreases with curing. There is an increase of attenuation during curing that was directly measured for the two separate systems. A rough estimate, based on curing of the individual systems, indicates that the power can reduce in the order of 25% in the first 60 s. For each sample, in addition to evaluating the curing under light, curing after the end of light exposure (dark curing) was also evaluated up to 2400 s. The results of this study are shown in Figure 6. As can be seen, for these conditions the conversion process of both the acrylate and BADGE are unaffected by light exposures longer than 60 s.

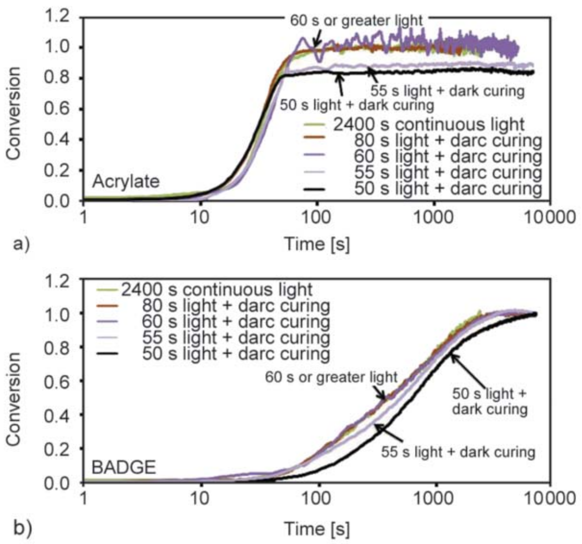

Figure 6. Effect of different durations of light exposure followed by dark curing for the 50/50 acrylate/BADGE mixture: Conversion of (a) acrylate component and (b) BADGE component.

Figure 6a indicates that the acrylate reaches the plateau of full conversion after approximately 60 s of light exposure. For exposures below this minimum required exposure, the acrylate does not fully cure. Figure 6b shows that the epoxy component continues to cure for over 40 min, but is not affected by light exposure after the minimum light exposure time for activation of all the cationic initiators, which was approximately 60 s. As can be seen, full curing of the BADGE still occurs for shorter exposer times (e.g., 50 and 55 s), but the time to reach full curing is longer. In these cases there is a possible change in the final structure of the cross-linked polymer and its properties [43, 44]. For the experimental conditions, full initiation of the BADGE should happen between 55 and 60 s. As shown in the figure, light exposure after 60 s did not have any effect on the curing process as the acrylate was fully converted and the cationic initiators for the BADGE monomer (oligomer) were fully initiated. We denote this as a fully initiated system, after which dark curing in the system (for the BADGE component) occurs unaffected by light exposure.

An experimental study of the effect of the extent of dark curing was done to establish if the extent of dark curing could be used to control final material properties. From Figure 6b, four curing times of 300, 700, 900, and 2400 s (fully cured) were selected for the main study. Samples of the 50/50 acrylate/BADGE system were prepared and allowed to cure to these respectively selected curing times using the same conditions described above, after which the samples were removed and put in acetone [42] for 24 hours to remove any uncured BADGE monomers (oligomers). This was done to terminate any further curing

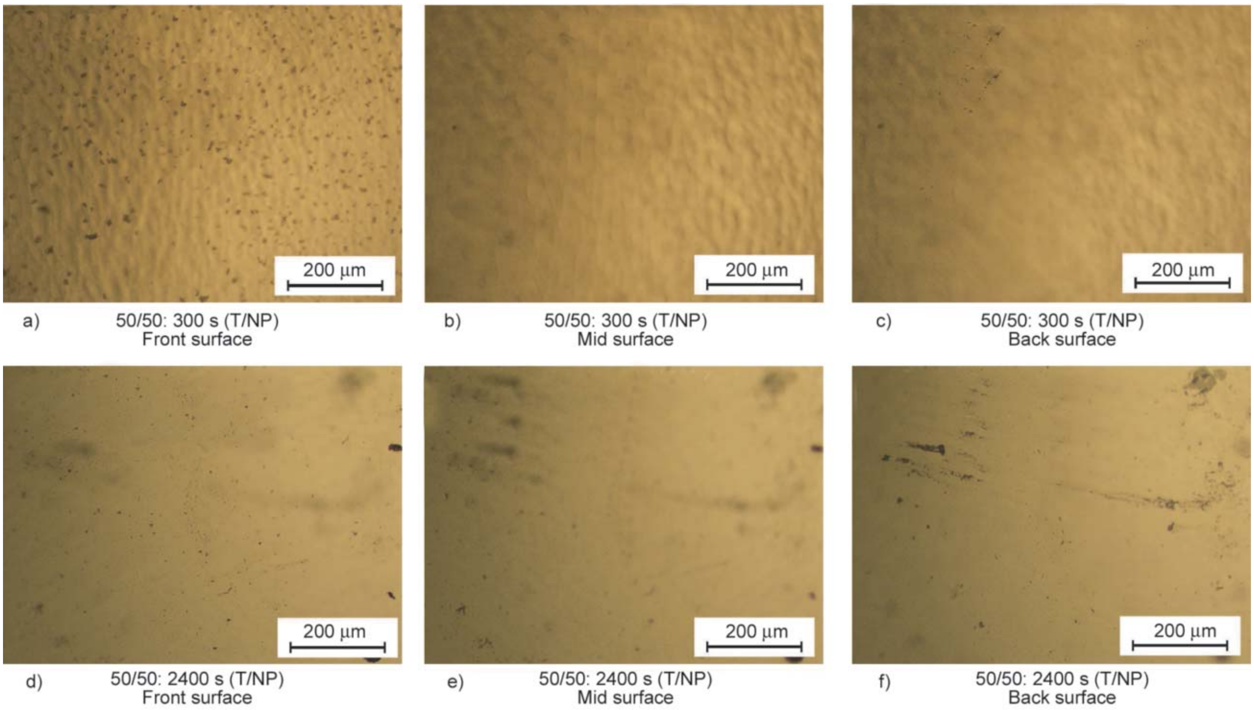

a) 50/50: 300 s (T/NP) Front surface
b) 50/50: 300 s (T/NP) Mid surface
c) 50/50: 300 s (T/NP) Back surface
d) 50/50: 2400 s (T/NP) Front surface
e) 50/50: 2400 s (T/NP) Mid surface
f) 50/50: 2400 s (T/NP) Back surface

Figure 7. Transmission optical microscopy of the top (left), middle (center), bottom (left) focus depths for the 300 s (top) and 2400 s (bottom) cure times (200 µm scale shown)

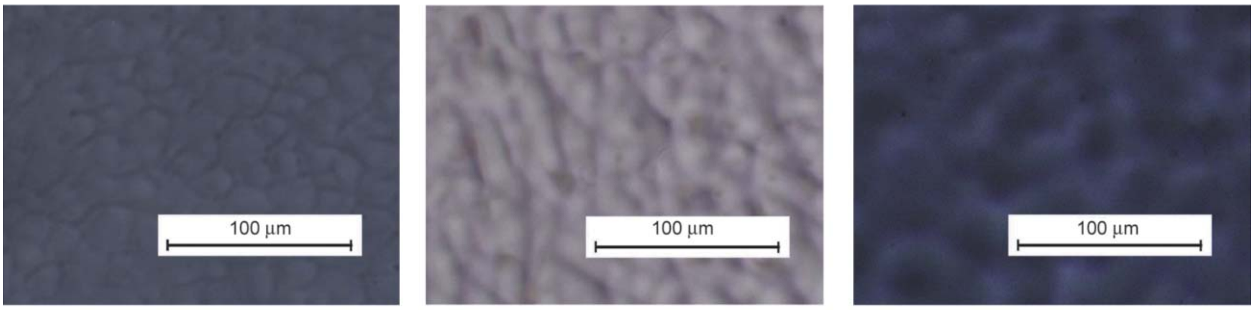

a) Acrylate (T/NP) b) 50/50: 300 s (T/NP) c) 50/50: 700 s (T/NP)

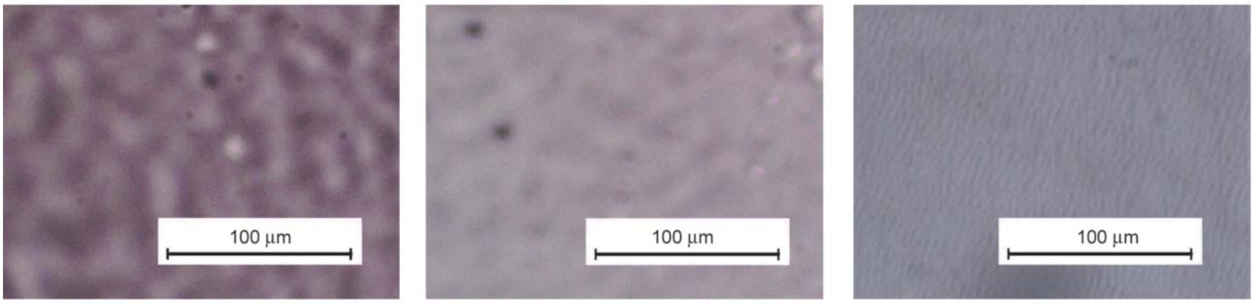

d) 50/50: 900 s (T/NP) e) 50/50: 2400 s (T/NP) f) BADGE (T/NP)

Figure 8. Optical transmission microscopy focused in the center of the thickness for (a) pure acrylate, (b, c, d, e) for 50/50 acrylate/BADGE mixture with 300 to 2400 s of curing, and (f) pure epoxy (100 μm scale shown)

of the BADGE network. For reference, samples of pure acrylate and pure BADGE, using their respective initiators, were prepared and cured under the same conditions.

Figure 7 shows transmission optical microscopy of the 300 and 2400 s cured 50/50 acrylate/BADGE system. The picture is focused on the top (front), middle, and bottom (back) surfaces. Optical spectroscopy provides a picture of density variations in the samples. The 300 s dark cured system shows micrometer sized variations throughout the system, while the fully cured system (2400 s curing) shows no noticeable variation on this scale. Figure 8 shows a comparison of the different extents of curing in comparison to that of pure acrylate and pure BADGE. As can be seen, the pure acrylate shows density variations on the scale of 20–30 micrometer, while the pure BADGE shows variation at a scale of 3–5 micrometer. As can be seen for the 50/50 mixtures, all show density variations that are similar to that of pure acrylate. This variation is showing more diffused characteristics with the increase of the dark curing time, possibly an indication of the increasing formation of the BADGE network.

Figure 9 shows Atomic-Force microscopy (AFM) of the surface of the 50/50 fully cured acrylate/BADGE system. As can be seen from Figure 9a, there is a pattern of approximately 60 nanometer circular indentations of 4 to 10 nanometer depth. The phase angle,

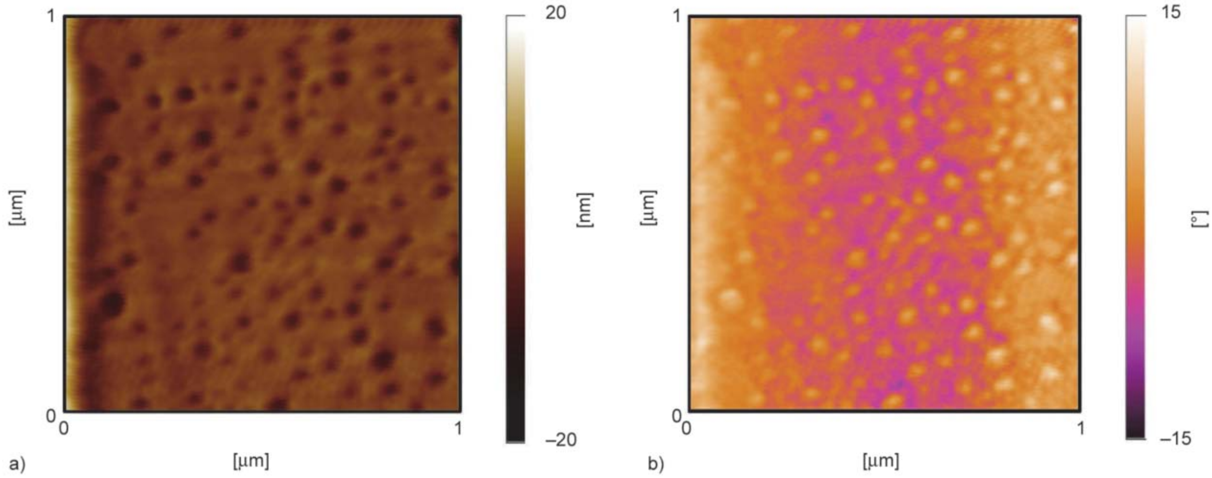

Figure 9. AFM micrographs for (a) height and (b) phase angle of the 50/50 fully cure acrylate/BADGE system

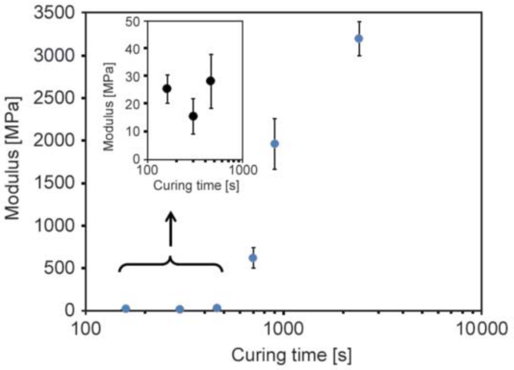

Figure 10. Mechanical property of samples evaluated by nano-indentation after the total time of curing indicated. In each case, 60 s of initial light exposure was followed by dark curing to the final curing time indicated.

shown in Figure 9b, indicate a small phase difference of less than 10 degrees between adjacent locations, indicating similarity of material properties for the holes and their surrounding material.

Figure 10 shows the change in mechanical properties of the 50/50 mixture after different extents of curing. The modulus was evaluated by nano-indentation on the samples after post curing for 1 hour at 150 °C. Shown is curing times starting from 160 to 2400 s that correspond to dark curing times from 100 to 2340 s. As above, in each case the conversion of the BADGE component was terminated by washing the sample after the dark curing. As can be seen, for curing times below 400 s, the modulus of the system is identical to pure acrylate, while after this time the modulus gradually increases to that of pure BADGE.

Figure 11 shows the heat flow signal obtained by Flash DSC for pure acrylate, pure epoxy, and the 50/50 acrylate/BADGE system for different amount of curing time. As above, the 50/50 systems were exposed with the laser for 60 s and then dark cured until the indicated total curing times. This produced circular samples under the laser spot of approximately 1–2 mg size with 200 µm thickness and approximately 2–3 mm diameter, which is smaller than the 5–10 mg sample size recommended for regular DSC. From these, 0.5–10 µg samples were cut from the center of the circular disk, including the full cross-section, and placed at the center of the Flash DSC sensor. For each sample, the figure includes an optical picture of the segment cut from the central portion of the circular sample and a strip cut from this and rotated to show the cross section. The DSC sample was cut from this strip. In each case, other than for pure acrylate, the samples were post cured in the Flash DSC for 5 minutes at 170 °C. For pure acrylate, which had a glass transition (T_g) around –30 °C, the sample was post cured at 70 °C. In every case both the heating signal and the cooling signal after post curing was repeatable, showing no further changes even after multiple cycles of heating and cooling. The figure shows the heat flow during heating from –80 °C at a rate of 100 °C/s. As the mass is not known for the Flash DSC samples, the signals shown have been scaled, shifted and rotated to allow clear observation of the glass transition. As can be seen in Table 1, the T_g of the 50/50 acrylate/BADGE system varies between that of pure acrylate and pure BADGE. We observed a single T_g for the mixture with no other observable transitions. A single observed T_g is evidence of the formation of homogeneous IPNs [50, 51]. It should be noted that the T_g seen during Flash DSC is typically 10–20 °C higher than that seen in regular DSC. This is due to the higher heating speeds in the Flash DSC.

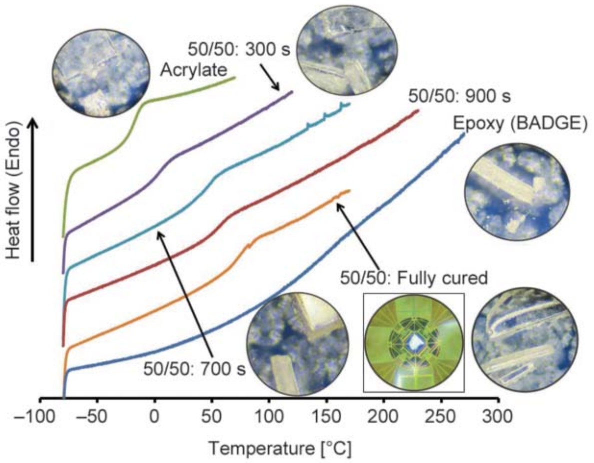

Figure 11. Flash DSC thermograms of the cured systems for pure acrylate, pure BADGE and the 50/50 acrylate/BADGE IPNs under different curing times (300–2400 s). Heat flow is scaled and shifted to visually separate the signals.

Table 1. Glass transition temperatures at 100 °C/s for pure acrylate and BADGE and the partially dark cured 50/50 mixtures

Pure acrylate	50/50 acrylate/BADGE mixture				Pure BADGE
	300 s	700 s	900 s	Fully cured	
–17±2 °C	5±2 °C	46±2 °C	57±2 °C	74±2 °C	140±5 °C

Changing the properties of IPNs is typically achieved by changing the ratio of the two or more components that will construct the networks of the IPNs. As shown in Figure 10, one can achieve two orders of magnitude variation in mechanical modulus even when starting from the same 50/50 acrylate/BADGE mixture by prematurely terminating the formation of the BADGE network through controlling the extent of dark curing. As shown in Figure 11, this premature termination of network formation still produces homogenous IPNs, which is evidenced by a single observed T_g and no other observed transitions [50, 51].

4. Graded printing design and demonstration

The main goal of this work is to demonstrate the ability to print graded IPNs entirely based on knowledge of the curing kinetics and, in particular, to achieve this from the same initial mixture. As was demonstrated in the last section, properties can be changed for the same initial mixture by controlling the extent of the dark curing of the cationic (epoxy) component. This information is used to design and demonstrate a printing process for constructing graded IPNs.

A 3D printer was used to construct a graded sample based on the observed kinetics for the 50/50 acrylate/BADGE system. The printer was connected by a fiber optic cable to the same laser source used for the results shown in Figure 5–11. Unlike the conditions on the ATR, shown in Figure 2, the printer head produced a light beam that was focused in the curing system. As a result, the beam was not collimated. In addition, the beam spot in the printer moves so that it produces a substantially more complex light exposure (see [52]). In addition to light attenuation in the solution, at least three other factors need to be considered to allow adaptation of the results obtained from curing on the ATR, which is under a stationary and columnar lighting source. In particular, the laser beam in the printer is focused, the power distribution in the cross section of the beam is not uniform, and the beam moves, which makes the exposure at the centerline of the beam path vastly different from its outer edges. These facts are described in Figure 12. The power distribution of the beam at the focal point of the light is shown in Figure 12b, which when moved produces an exposure distribution that resemble that shown in Figure 12c, having a decreasing exposure from the center line of the beam path to its edges. For the conical power distribution measured in Figure 12b, the exposer takes the form shown in Figure 12e (normalized to the central intensity) for the points identified in the beam profile shown in Figure 12d, and results in the total energy exposures shown in Figure 12f. As a result, the light exposure varies substantially at different positions under the moving light beam. To simplify the demonstration, we focused our attention on the centerline of the traveling beam line, which is exposed to a triangular energy profile. In addition, we know that the kinetics of radical curing of the acrylate changes with the square root of the light power, while the initiation of the cationic initiators are a linear function of power [53, 54]. Therefore, over exposing a point will result in faster formation of the acrylate network, while will have only a small effect on the formation of the BADGE network. Assuming the earlier formation of the acrylate network relative to the BADGE network will not have a substantial effect on the final proper-

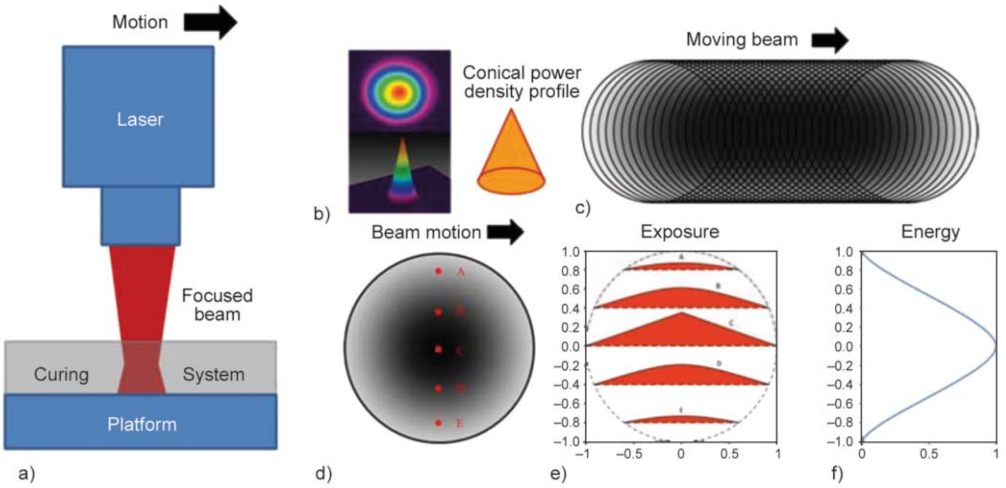

Figure 12. Schematic of laser beam profile, motion, and exposure for moving printer head

ties of the system, conditions were selected that over-expose the system as the light source traveled over the mixture.

The demonstration of grading was done by placing the 50/50 acrylate/BADGE mixture in a sandwiched mold that included 250 µm thick polycarbonate (PC) container (spacer) that was placed on a 2 mm thick PC slide and covered with a 1mm fused silica cover. The sample and mold were put on the hot plate of the 3D printer and kept in an Argon controlled atmosphere at 85 °C. The laser beam from the printing head was focused at 200 µm sample depth from the top surface, with a light spot diameter of 2 mm. The peak of the power intensity of the laser at this location was 2.6 mW/cm^2 taking into account the attenuation using the Beer-Lambert law. The printing head was programmed to move 25 mm from the left to the right in a straight line along the sample cavity with a velocity of 0.01 mm/s. Immediately after scanning the sample with the laser, the mold was immersed in an acetone solution to separate the PC parts of the mold and was left in the acetone for 24 hours to extract the uncured components from the sample [42]. The sample remained connected to the fused silica. After this extraction, the sample was post cured for one hour at 150 °C. The sample was then polished to remove about 50 µm from the bottom surface before characterization by nano-indentation.

For the selected exposure conditions and sample thickness of the curing system, as the traveling beam passes over a point, the centerline of the traveling beam should fully cure the acrylate and fully initiate the cationic initiator to start curing the BADGE. Thus, the elapsed time from when the beam passes a point should approximately be the dark curing time for the formation of the BADGE network.

The insert of Figure 13 shows the printed sample and the graph shows the modulus measured along the centerline of the beam using nano-indentation. In this case, the beam travels from left to right, so the sample at the left was exposed first and thus had the longest dark curing time. As the sample was washed in acetone immediately after completing the exposure, the dark curing time in the sample linearly decreased from left to right. As can be seen, in this demonstration the modulus varies from 3,300 MPa to 24 MPa over a distance of about 10 mm. In addition, the sample shows a color variation that goes from a slight yellowish color, sometimes seen in epoxy curing, on the left to being clear, characteristic of acrylate, on the right. The printing was repeated twice and both repetitions show similar grading. The authors believe that this is the first time that grading of the modulus has been demonstrated in IPNs that are made by starting from a uniform mixture and for which the dark curing time is used to achieve a two order of magnitude change in properties.

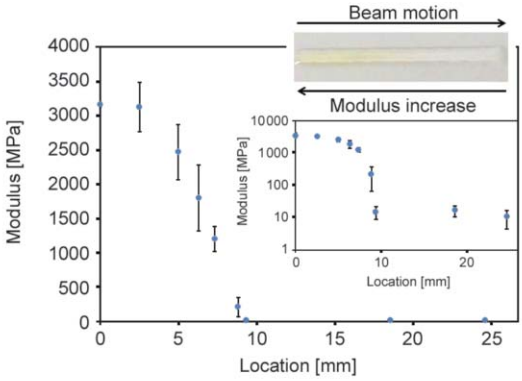

Figure 13. Mechanical property of the printed IPNs measured by nano-indentation on the centerline of the sample

5. Conclusions

IPNs have traditionally been used to get several orders of magnitude change in mechanical properties through varying the ratio of the components in the initial mixture used to obtain the IPNs. This is possible when starting with components that have vastly different properties so that the ratio of the components can results in behavior varying from a rubber to a rigid glass by mixing different amounts of each component and then curing the system. The current work demonstrates that one can also obtain IPNs with similar variations even when starting from a single ratio of components. This was done for an acrylate/epoxy system that was photo initiated. The acrylate in this system follows a radical, while the epoxy followed a cationic network formation. As a result, the epoxy continued to form its network even after light exposure had ended. Control of this dark curing time was used to construct samples with vastly different properties, yet still obtaining IPNs. It is believed that this is the first time that the dark curing time has been demonstrated as a tool to obtain IPNs of vastly different properties from the same initial mixture.

In addition, it was demonstrated that the dark curing time of the cationic component can be used to print a grading that gradually varies several orders of magnitude in the modulus over the millimeter length scale. Since the system is forming IPNs, the grading should be scalable down to the nanometer length scale, and may have potential in nano-printing of graded properties. It is believed that this is the first time that graded IPNs have been constructed from a single mixture based on controlling the dark curing time.

Acknowledgements

The authors would like to acknowledge the help of and thank Mr. Evan Schwahn for the implementation of the printing design in the 3D printer, Mr. Xavier Monnier for aiding with the optical microscopy, and Ms. Nagihan Varol and Mr. Walker Dimon for completing the Flash-DSC.

References

[1] Claussen K. U., Scheibel T., Schmidt H-W., Giesa R.: Polymer gradient materials: Can nature teach us new tricks? Macromolecular Materials and Engineering, **297**, 938–957 (2012).
DOI: 10.1002/mame.201200032

[2] Suresh S., Mortensen A.: Fundamentals of functionally graded materials. IOM, London (1998).

[3] Miserez A., Schneberk T., Sun C., Zok F. W., Waite J. H.: The transition from stiff to compliant materials in squid beaks. Science, **319**, 1816–1819 (2008).
DOI: 10.1126/science.1154117

[4] Suresh S.: Graded materials for resistance to contact deformation and damage. Science, **292**, 2447–2451 (2001).
DOI: 10.1126/science.1059716

[5] Hirano T., Wakashima K.: Mathematical modeling and design. MRS Bulletin, **20**, 40–42 (1995).
DOI: 10.1557/S0883769400048922

[6] Koizumi A.: Recent progress of functionally gradient materials in Japan. in 'Proceedings of the 16th annual conference on composites and advanced ceramic materials: Ceramic engineering and science proceedings' (ed.: Wachtman J. B.) Wiley, Hoboken, 332–347 (2008).
DOI: 10.1002/9780470313954.ch33

[7] Erdogan F., Kaya A. C., Joseph P. F.: The crack problem in bonded nonhomogeneous materials. Journal of Applied Mechanics, **58**, 410–418 (1991).
DOI: 10.1115/1.2897201

[8] Williamson R. L., Rabin B. H., Drake J. T.: Finite element analysis of thermal residual stresses at graded ceramic-metal interfaces. Part I. Model description and geometrical effects. Journal of Applied Physics, **74**, 1310–1320 (1993).
DOI: 10.1063/1.354910

[9] Erdogan F.: Fracture mechanics of functionally graded materials. Composites Engineering, **5**, 753–770 (1995).
DOI: 10.1016/0961-9526(95)00029-M

[10] Giannakopoulos A. E., Suresh S., Finot M., Olsson M.: Elastoplastic analysis of thermal cycling: Layered materials with compositional gradients. Acta Metallurgica et Materialia, **43**, 1335–1354 (1995).
DOI: 10.1016/0956-7151(94)00360-T

[11] Kim A. S., Suresh S., Shih C. F.: Plasticity effects on fracture normal to interfaces with homogeneous and graded compositions. International Journal of Solids and Structures, **34**, 3415–3432 (1997).
DOI: 10.1016/S0020-7683(96)00225-9

[12] Kim A. S., Besson J., Pineau A.: Global and local approaches to fracture normal to interfaces. International Journal of Solids and Structures, **36**, 1845–1864 (1999).
DOI: 10.1016/S0020-7683(98)00062-6

[13] Prasad A., Dao M., Suresh S.: Steady-state frictional sliding contact on surfaces of plastically graded materials. Acta Materialia, **57**, 511–524 (2009).
DOI: 10.1016/j.actamat.2008.09.036

[14] Gupta N., Srivastava A. K.: Interpenetrating polymer networks: A review on synthesis and properties. Polymer International, **35**, 109–118 (1994).
DOI: 10.1002/pi.1994.210350201

[15] Lipatov Y. S., Karabanova L. V., Sergeeva L. M.: Thermodynamic state of reinforced interpenetrating polymer networks. Polymer International, **34**, 7–13 (1994).
DOI: 10.1002/pi.1994.210340102

[16] Kim S. C., Sperling L. H.: IPNs around the world: Science and engineering. Wiley, Chichester (1997).

[17] Karabanova L. V., Mikhalovska S. V., Sergeeva L. M., Meikle S. T., Helias M., Lloyd W.: Semi-interpenetrating polymer networks based on polyurethane and poly (vinyl pyrrolidone) obtained by photopolymerization: Structure-property relationships and bacterial adhesion. Polymer Engineering and Science, **44**, 940–947 (2004).
DOI: 10.1002/pen.20085

[18] Sperling L. H., Hu R.: Interpenetrating polymer networks. in 'Polymer blends handbook' (eds.: Utracki L. A., Wilkie C. A.) Springer, Dordrecht, 677–724 (2014).
DOI: 10.1007/978-94-007-6064-6_8

[19] Frisch H. L., Klempner D., Frisch K. C.: A topologically interpenetrating elastomeric network. Journal of Polymer Science Part B: Polymer Letters, **7**, 775–779 (1969).
DOI: 10.1002/pol.1969.110071104

[20] Myung D., Waters D., Wiseman M., Duhamel P-E., Noolandi J., Ta C. N., Frank C. W.: Progress in the development of interpenetrating polymer network hydrogels. Polymers for Advanced Technologies, **19**, 647–657 (2008).
DOI: 10.1002/pat.1134

[21] Akovali G.: Studies with gradient polymers of polystyrene and poly(methyl acrylate). Journal of Applied Polymer Science, **73**, 1721–1725 (1999).
DOI: 10.1002/(SICI)1097-4628(19990829)73:9<1721::AID-APP12>3.0.CO;2-U

[22] Lv X., Huang Z., Huang C., Shi M., Gao G., Gao Q.: Damping properties and the morphology analysis of the polyurethane/epoxy continuous gradient IPN materials. Composites Part B: Engineering, **88**, 139–149 (2016). DOI: 10.1016/j.compositesb.2015.10.040

[23] Frisch H. L., Frisch K. C., Klempner D.: Glass transitions of topologically interpenetrating polymer networks. Polymer Engineering and Science, **14**, 646–650 (1974). DOI: 10.1002/pen.760140910

[24] Sorathia U. A., Yeager W. L., Dapp T. L.: Polyurethane-epoxy interpenetrating polymer network acoustic damping material. US 5331062 A, U.S. Patent, USA (1994).

[25] Sperling L. H.: Interpenetrating polymer networks. in 'Encyclopedia of polymer science and technology' (ed.: Mark H. F.) Wiley, New York, 272–311 (2002). DOI: 10.1002/0471440264.pst170

[26] Touhsaent R. E., Thomas D. A., Sperling L. H.: Epoxy/acrylic simultaneous interpenetrating networks. Journal of Polymer Science: Polymer Symposia, **46**, 175–190 (1974). DOI: 10.1002/polc.5070460115

[27] Morancho J. M., Cadenato A., Ramis X., Fernández-Francos X., Salla J. M.: Thermal curing and photocuring of an epoxy resin modified with a hyperbranched polymer. Thermochimica Acta, **510**, 1–8 (2010). DOI: 10.1016/j.tca.2010.05.008

[28] Chen J., Soucek M. D.: Ultraviolet curing kinetics of cycloaliphatic epoxide with real-time fourier transform infrared spectroscopy. Journal of Applied Polymer Science, **90**, 2485–2499 (2003). DOI: 10.1002/app.12898

[29] Yagci Y., Jockusch S., Turro N. J.: Photoinitiated polymerization: Advances, challenges, and opportunities. Macromolecules, **43**, 6245–6260 (2010). DOI: 10.1021/ma1007545

[30] Crivello J. V., Reichmanis E.: Photopolymer materials and processes for advanced technologies. Chemistry of Materials, **26**, 533–548 (2014). DOI: 10.1021/cm402262g

[31] Fouassier J. P., Lalevée J.: Photochemical production of interpenetrating polymer networks; Simultaneous initiation of radical and cationic polymerization reactions. Polymers, **6**, 2588–2610 (2014). DOI: 10.3390/polym6102588

[32] Decker C.: Photoinitiated crosslinking polymerisation. Progress in Polymer Science, **21**, 593–650 (1996). DOI: 10.1016/0079-6700(95)00027-5

[33] Decker C., Nguyen Thi Viet T., Decker D., Weber-Koehl E.: UV-radiation curing of acrylate/epoxide systems. Polymer, **42**, 5531–5541 (2001). DOI: 10.1016/S0032-3861(01)00065-9

[34] Hoyle C. E.: Photocurable coatings. in 'Radiation curing of polymeric materials' (eds.: Hoyle C. E., Kinstle J. F.) American Chemical Society, Dallas, Vol 417, 1–16 (1990). DOI: 10.1021/bk-1990-0417.ch001

[35] Barner-Kowollik C.: Acrylate free radical polymerization: From mechanism to polymer design. Macromolecular Rapid Communications, **30**, 1961–1963 (2009). DOI: 10.1002/marc.200900676

[36] Lipatov Y. S., Semenovitch G. M., Skiba S. I., Karabanova L. V., Sergeeva L. M.: The kinetic peculiarities of interpenetrating polymer network formation. Polymer, **33**, 361–364 (1992). DOI: 10.1016/0032-3861(92)90994-8

[37] Karabanova L., Pissis P., Kanapitsas A., Lutsyk E.: Thermodynamic state, temperature transitions, and broadband dielectric relaxation behavior in gradient interpenetrating polymer networks. Journal of Applied Polymer Science, **68**, 161–171 (1998). DOI: 10.1002/(SICI)1097-4628(19980404)68:1<161::AID-APP18>3.0.CO;2-3

[38] Lee S. J., Kim S. S., Lee Y. M.: Interpenetrating polymer network hydrogels based on poly(ethylene glycol) macromer and chitosan. Carbohydrate Polymers, **41**, 197–205 (2000). DOI: 10.1016/S0144-8617(99)00088-0

[39] Ramis X., Cadenato A., Morancho J. M., Salla J. M.: Polyurethane–unsaturated polyester interpenetrating polymer networks: Thermal and dynamic mechanical thermal behaviour. Polymer, **42**, 9469–9479 (2001). DOI: 10.1016/S0032-3861(01)00492-X

[40] Lee L-H.: Mechanisms of thermal degradation of phenolic condensation polymers. III. Cleavage of phenolic segments during the thermal degradation of uncured epoxy resins. Journal of Applied Polymer Science, **9**, 1981–1989 (1965). DOI: 10.1002/app.1965.070090529

[41] Golaz B., Michaud V., Leterrier Y., Månson J. A. E.: UV intensity, temperature and dark-curing effects in cationic photo-polymerization of a cycloaliphatic epoxy resin. Polymer, **53**, 2038–2048 (2012). DOI: 10.1016/j.polymer.2012.03.025

[42] Sipani V., Scranton A. B.: Dark-cure studies of cationic photopolymerizations of epoxides: Characterization of the active center lifetime and kinetic rate constants. Journal of Polymer Science Part A: Polymer Chemistry, **41**, 2064–2072 (2003). DOI: 10.1002/pola.10750

[43] Sipani V., Kirsch A., Scranton A. B.: Dark cure studies of cationic photopolymerizations of epoxides: Characterization of kinetic rate constants at high conversions. Journal of Polymer Science Part A: Polymer Chemistry, **42**, 4409–4416 (2004). DOI: 10.1002/pola.20209

[44] Mark H. F.: Encyclopedia of polymer science and technology, concise. Wiley, Hoboken (2013).

[45] Ramírez C., Rico M., Torres A., Barral L., López J., Montero B.: Epoxy/POSS organic–inorganic hybrids: ATR-FTIR and DSC studies. European Polymer Journal, **44**, 3035–3045 (2008). DOI: 10.1016/j.eurpolymj.2008.07.024

[46] Nikolic G., Zlatkovic S., Cakic M., Cakic S., Lacnjevac C., Rajic Z.: Fast fourier transform IR characterization of epoxy GY systems crosslinked with aliphatic and cycloaliphatic EH polyamine adducts. Sensors, **10**, 684–696 (2010).
DOI: 10.3390/s100100684

[47] Fischer-Cripps A. C.: Critical review of analysis and interpretation of nanoindentation test data. Surface and Coatings Technology, **200**, 4153–4165 (2006).
DOI: 10.1016/j.surfcoat.2005.03.018

[48] Beer A.: Bestimmung der Absorption des rothen Lichts in farbigen Flüssigkeiten. Annalen der Physik, **162**, 78–87 (1852).
DOI: 10.1002/andp.18521620505

[49] Emami N., Sjödahl M., Söderholm K-J. M.: How filler properties, filler fraction, sample thickness and light source affect light attenuation in particulate filled resin composites. Dental Materials, **21**, 721–730 (2005).
DOI: 10.1016/j.dental.2005.01.002

[50] Fainleib A., Novikova T., Shantaly T., Sergeeva L.: Synthesis, structure, and some properties of the polycyanurate-polyurethane semi-IPNs. Polymeric Materials: Science and Engineering, **66**, 131–132 (1992).

[51] Bartolotta A., Di Marco G., Lanza M., Carini G., D'Angelo G., Tripodo G., Fainleib A., Slinchenko E., Privalko V.: Molecular mobility in semi-IPNs of linear polyurethane and heterocyclic polymer networks. The Journal of Adhesion, **64**, 269–286 (1997).
DOI: 10.1080/00218469708010543

[52] Jacobs P. F.: Rapid prototyping and manufacturing: Fundamentals of stereolithography. Society of Manufacturing Engineers, Dearborn (1992).

[53] Gibson I., Rosen D. W., Stucker B.: Additive manufacturing technologies: Rapid prototyping to direct digital manufacturing. Springer, New York (2010).
DOI: 10.1007/978-1-4419-1120-9

[54] Beaman J. J., Barlow J. W., Bourell D. L., Crawford R. H., Marcus H. L., McAlea K. P.: Solid freeform fabrication: A new direction in manufacturing. Springer, New York (1997).

eXPRESS Polymer Letters Vol.10, No.12 (2016) 1016–1025
Available online at www.expresspolymlett.com
DOI: 10.3144/expresspolymlett.2016.94

Mechanical properties of reactively flame retarded cyanate ester/epoxy resin blends and their carbon fibre reinforced composites

A. Toldy[1*], *P. Niedermann*[1], *G. Szebényi*[1,2], *B. Szolnoki*[3]

[1]Department of Polymer Engineering, Faculty of Mechanical Engineering, Budapest University of Technology and Economics, H-1111 Budapest, Műegyetem rkp. 3, Hungary
[2]MTA–BME Research Group for Composite Science and Technology, H-1111 Budapest, Műegyetem rkp. 3., Hungary
[3]Department of Organic Chemistry and Technology, Faculty of Chemical Technology and Biotechnology, Budapest University of Technology and Economics, H-1111 Budapest, Budafoki út 8.

Received 8 June 2016; accepted in revised form 25 July 2016

Abstract. Cyanate ester/epoxy resin (CE/EP) carbon fibre reinforced composites consisting of diglycidyl ether of bisphenol A (DGEBA) and novolac type cyanate ester (CE) were prepared and reactively flame retarded using epoxy functional adduct of DGEBA and 9,10-dihydro-9-oxa-10-phosphaphenanthrene-10-oxide (DOPO). Effect of cyanate ester and flame retardant (FR) ratio was determined on matrix viscosity, matrix and composite glass transition temperature (T_g), as well as composite mechanical properties including storage modulus, tensile, bending, interlaminar shear and Charpy impact properties. Although the epoxy resin (EP) and FR decreased the T_g, even the flame retarded CE/EP blends had at least 22 °C higher T_g than the benchmark DGEBA composite. As for the mechanical properties, as a result of higher interlaminar shear strength suggesting better fibre-matrix adhesion, the CE/EP blends managed to over-perform the reference CE in most cases: The 2% phosphorus (P)-containing CE/EP composite had 25% higher tensile strength than the CE reference. The bending strength of the blends remained in the same range as the reference, while the impact resistance significantly increased in comparison to CE, especially in flame retarded composites.

Keywords: *mechanical properties, flame retardancy, cyanate ester, epoxy resin, carbon fibre reinforced composites*

1. Introduction

Even in case of high performance thermosetting polymer materials as cyanate esters and epoxy resins the flame retardancy is still an issue to be solved, particularly in advanced sectors with strict safety requirements as electrical and aeronautical industry. However, the addition of flame retardants usually decreases the glass transition temperature and mechanical properties of the polymers [1]. One possibility to minimize these effects is to apply reactive flame retardants, which can be chemically incorporated into the polymer structure. This approach offers further advantages: as the flame retardant does not migrate to the surface of the matrix either during high temperature processing or application, it provides more stable effect compared to additive flame retardants and lower ratio is sufficient to achieve the same level of flame retardancy [2]. The increasing focus on the health and environmental compatibility of flame retardants also facilitated the headway of this reactive approach, in particular many organophosphorus reactive flame retardants were developed in the recent years [3–6]. Another way to compensate the effect of flame retardants is to form blends with another polymer possessing high glass transition temperature, thermally stable backbone and outstanding me-

---

[*]Corresponding author, e-mail: atoldy@mail.bme.hu

chanical properties. Again, instead of simple blend formation reactive blending resulting in primary chemical bonds between the polymers is preferred. For these reasons epoxy resins are often blended with cyanate esters [7–10], which can be applied instead of the commonly applied amine or anhydride type hardeners. This way cyanate esters can be used as multifunctional reactive modifiers increasing the glass transition temperature, and improving the thermal stability and mechanical properties of flame retarded epoxy resins.

In CE/EP systems either the EP [11, 12] or the CE component [13–15] can contain the phosphorus (P) -containing flame retardant unit, but separate P-containing reactive modifiers (mostly with –OH [16] and $–NH_2$ functions [17]) can be applied as well. These articles studied the flame retardancy results of P-containing CE/EP or CE, along with the effect on glass transition temperature and in some cases on modulus only in polymer matrices. To the extent of our knowledge, no articles have been published yet on the effects of phosphorus flame retardants on glass transition temperature and mechanical properties in CE/EP fibre reinforced composites, therefore our current study aims at filling in this gap.

In particular, in this work the EP component, DGEBA was pre-reacted with DOPO in order to obtain an epoxy functional reactive flame retardant, and a novolac type, high glass transition temperature CE was blended with it. As the flame retardants generally decrease the glass transition temperature of EPs, the hybrid system consisting of CE, EP and reactive flame retardant was made in order to reach higher glass transition temperature than in case of flame retarded EP alone.

Based on flame retardancy results of these CE/EP systems (published previously by the authors [18]), the best performing blends were chosen, and the effect of CE and flame retardant ratio was determined on viscosity, glass transition temperature (T_g) and dynamic mechanical properties. From these best performing blends also reactively flame retarded CE/EP carbon fibre reinforced composites were made and their dynamic mechanical, tensile, bending, interlaminar shear strength and Charpy impact properties were tested and compared to CE and EP benchmarks.

2. Materials and methods

2.1. Materials

Novolac type cyanate ester (Primaset PT-30) was acquired from Lonza Ltd. (Basel, Switzerland).

Diglycidyl ether of bisphenol A (DGEBA, Ipox ER 1010) with 188 g/eq epoxy equivalent weight was obtained from IPOX Chemicals Ltd. (Budapest, Hungary).

As reactive flame retardant 9,10-dihydro-9-oxa-10-phosphaphenanthrene-10-oxide (DOPO, Struktol Polydis 3710, properties: molecular mass: 216.17 g/mol, melting point: 116 °C) was used supplied by Struktol Gmbh (Hamburg, Germany).

In order to form a phosphorus-containing epoxy component, DOPO was reacted with DGEBA in 1:1 molar ratio. Before the reaction DOPO was kept at 85 °C for 12 h, in order to eliminate the traces of moisture. DGEBA was kept under vacuum at 110 °C to remove air and traces of moisture, and after adding DOPO, the mixture was stirred at 160 °C for 5 h. After cooling to room temperature a solid adduct was obtained. This synthesis, based on the method of Wang and Lin [19], was published by the authors previously [18]. The main advantage of the adduct formation is, that this way the highly intensive reaction between DOPO and PT-30, furthermore carbamate and consequent CO_2 formation from CE due to water traces present in DOPO (despite careful drying) can be avoided. Due to controlled reaction conditions and stoichiometry, an oxirane functional adduct is formed, which reacts the same way as DGEBA with PT-30 (main reactions: trimerization of cyanates, insertion of oxiranes into the cyanurate, isomerization of alkyl-substituted triazines and formation of oxalidinones from isocyanurates and glycidyl ethers [20]).

As hardener methyl-tetrahydrophthalic-anhydride (Aradur 917 – AR917) was applied with 1-methylimidazole (DY070) accelerator by Huntsman Advanced Materials (Basel, Switzerland). The equivalent mass of the anhydride type curing agent, calculated from its molecular mass, was 160 g/eq. The accelerator was applied in 2 mass% related to the mass of DGEBA.

The chemical structures of the used polymer components are shown in Figure 1.

As fibre reinforcement Zoltek Panex 35 type unidirectional carbon weave with 300 g/m^2 areal weight provided by Zoltek Ltd. (Nyergesújfalu, Hungary) was applied.

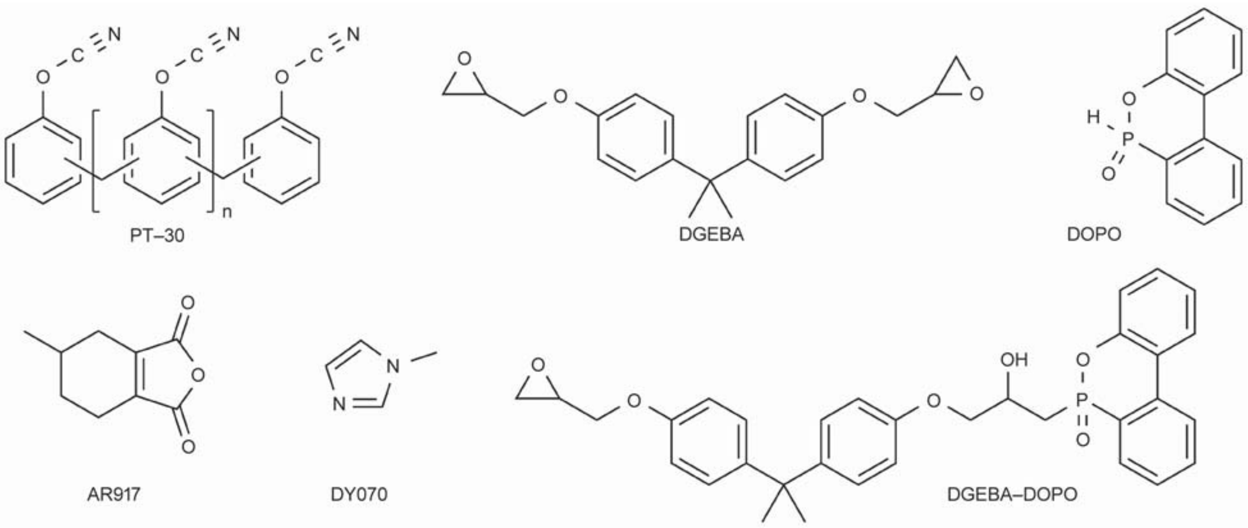

Figure 1. Chemical structures of the used polymer components

2.2. Methods

2.2.1. Sample preparation

Besides the reference CE, EP and CE/EP matrices, flame retarded CE/EP matrices with 2 and 3 mass% phosphorus were prepared using the synthesized DGEBA – DOPO adduct. The composition of the composite matrices is summarized in Table 1.

Polymer matrix specimens for the mechanical investigations were made by resin moulding with a vertical moulding tool. For the preparation of matrix specimens for flame retardancy testing heat resistant silicone moulds were used of appropriate size. The composite laminates were made by hand lamination followed by press moulding. Each carbon weave layer was separately impregnated, in case of high viscosity matrices the polymer and the mould were heated to 80 °C. The prepared laminates were put under compression with 25 bar pressure in T30 type platen press (Metal Fluid Engineering s. r. l., Verdello Zingonia, Italy) to achieve high and uniform fibre content in the composites. For flame retardancy measurements 4 mm thick specimens were made using $[0]_{10}$ of carbon weave, while for mechanical tests 2 mm thick laminates were made with $[0]_5$ layup. The heat treatment was carried out during pressing. Samples containing PT-30 were cured 1 h at 150 °C, 3 h at 200 °C and 1 h 260 °C according to the suggestion of CE supplier. In case of DGEBA the heat treatment consisted of a 1 h 80 °C and 3 h 140 °C isothermal step. The measured fibre content of the composites was in the range of 50–55 mass%.

2.2.2. Parallel plate rheometry

Viscosity was determined by parallel plate rheometry using AR2000 device from TA Instruments (New Castle, DE, USA) in the range of 25–80 °C, with 5 °C/min temperature ramp, applying 40 mm diameter plate and 150 μm gap between the plates.

2.2.3. Flame retardant characterization

The fire behaviour of the reference and flame retarded systems was characterized by limiting oxygen

Table 1. Composition of the CE, EP and CE/EP composite matrices

	Sample composition [mass%]				
	PT-30	**DGEBA**	**DOPO**	**AR917**	**DY070**
Reference samples					
PT-30	100	–	–	–	–
DGEBA	–	52.3	–	47.1	0.6
20% PT-30 - 80% DGEBA	20	80	–	–	–
40% PT-30 - 60% DGEBA	40	60	–	–	–
Flame retarded samples					
40% PT-30 - DGEBA – DOPO 2% P	40	46.1	13.9	–	–
40% PT-30 - DGEBA – DOPO 3% P	40	39.1	20.9	–	–

index measurements (LOI, according to ASTM D-2863). The LOI value expresses the minimum volume fraction of oxygen in a mixture of oxygen and nitrogen that supports flaming combustion of a material under specified test conditions.

Standard UL-94 flammability tests (according to ASTM D3081 and ASTM D-635, respectively) were also carried out in order to classify the samples based on their flammability in horizontal and vertical test setups.

Mass loss calorimeter tests were carried out by an instrument made by FTT Inc. (East Grinstead, UK) according to ISO 13927 standard method. Specimens (100×100×4 mm) were exposed to a constant heat flux of 50 kW/m^2 and ignited. Heat release values and mass reduction were continuously recorded during burning.

2.2.4. Dynamic mechanical analysis (DMA)

For the investigations of the dynamic mechanical properties and for the determination of the glass transition temperature (T_g) values DMA tests were carried out in three point bending setup with TA Q800 device of TA Instruments (New Castle, DE, USA). The temperature range was 0–260 °C (in case of pure CE samples 0–400 °C) with 3 °C/min heat rate. The frequency was 1 Hz. The size of the specimens was 55×10×2 mm (length × width × thickness), and the support span was 50 mm. The amplitude was strain controlled with 0.1% relative strain. From the results glass transition temperature based on the tanδ peaks (T_g) and storage modulus (E') values at 25 and 75 °C were determined by the software of the DMA device (TA Instruments Universal Analysis 2000 4.7A version).

2.2.5. Tensile test

Tensile tests were carried out to determine the composites tensile strength and tensile modulus values (E_m) by a Zwick Z250 (Ulm, Germany) type computer controlled universal tester, equipped with a 20 kN capacity load cell. Based on EN ISO 527 the specimen size was 140×10×2 mm (length × width × thickness). The test speed was 2 mm/min, and the initial test length was 80 mm. During the test, force and displacement values were recorded and the tensile parameters were calculated according to the standard. In each case 5 parallel tests were carried out.

2.2.6. Bending test

Bending tests were carried out in three point bending setup to determine the composites flexural strength and flexural modulus values by a Zwick Z250 (Ulm, Germany) type computer controlled universal tester, equipped with a 20 kN capacity load cell with standard three point bending fixtures. The size of the specimens, based on EN ISO 14125 was 100×10×2 mm (length × width × thickness). The test speed was 5 mm/min, and the span length was 80 mm. During the test, force and deflection values were recorded and the bending parameters were calculated according to the standard. In each case 5 parallel tests were carried out.

2.2.7. Interlaminar shear test

According to EN ISO 14130 interlaminar shear tests were carried out on 5–5 specimens with 20×10×2 mm size (length x width x thickness) by a Zwick Z020 (Ulm, Germany) universal tester. The support span was 10 mm and the test speed was 1 mm/min. From the registered force-deflection results apparent interlaminar shear strength was calculated and compared.

2.2.8. Charpy impact test

Charpy impact tests were carried out according to EN ISO 179-1 by a normal impact on unnotched specimens of 80 mm length, 10 mm width and 2 mm thick with a Ceast Resil Impactor Junior (Torino, Italy) instrumented pendulum equipped with a 2 J hammer using 2.9 m/s impact velocity, with 150° starting angle and 62 mm support span on 5–5 specimens from each sample. The force–time curves were registered by a Ceast DAS 8000 data acquisition unit and the Charpy impact energy was calculated and compared.

3. Results and discussion

3.1. Viscosity of polymer matrices

One major aspect of the processing of resin systems is their viscosity, therefore prior to composite preparation viscosity of the polymer matrices was determined in the function of temperature. According to Hay [21] for resin injection 100–300 mPa·s, for pultrusion 400–800 mPa·s, while for filament winding viscosity of 800–2000 mPa·s is recommended. Cyanate esters are often processed by filament winding, where the filaments are immersed into a heat-

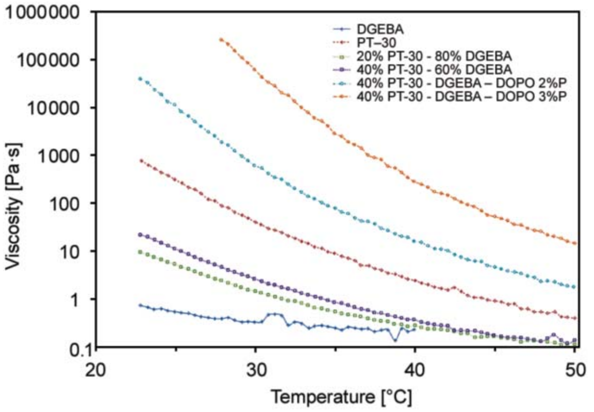

Figure 2. Viscosity of the CE and EP references and CE/EP blends in the temperature range of 25–80 °C

able resin bath allowing the reduction of the matrix viscosity by increasing its temperature. The viscosity of the CE and EP references and CE/EP blends in the temperature range of 25–80 °C can be seen in Figure 2.

By increasing the amount of CE in the blends, the viscosity increased, as expected. Furthermore, the addition of solid DOPO-DGEBA adduct significantly increased the viscosity as well. By increasing the temperature the viscosity of the matrices showed a monotone decreasing tendency.

According to the viscosity values at 80 °C (Table 2) the samples containing 3 mass% phosphorus can be rather processed by hot pressing, Blends containing 2 mass% phosphorus are suitable for filament winding as well.

Table 2. Viscosity of the CE and EP references and CE/EP blends at 80 °C

Sample	Viscosity [mPa·s]
PT-30	400
DGEBA	233*
20% PT-30 - 80% DGEBA	107
40% PT-30 - 60% DGEBA	113
40% PT-30 - DGEBA – DOPO 2%P	1 623
40% PT-30 - DGEBA – DOPO 3%P	14 780

*at 60 °C-on due to lower gel time

Based on these results hand lamination followed by hot pressing was chosen as composite preparation method, as it provides high fibre content and excellent reproducibility.

3.2. Flame retardancy of polymer matrices and composites

In order to be able to judge the overall performance of the CE/EP systems, their LOI, UL-94 and most important mass loss calorimetry results were summarized in Table 3. The flame retardancy results of the CE/EP matrices itself along with the results of polymer composites made thereof are discussed in detail elsewhere [18].

The addition of CE to EP significantly increased the LOI value, however it was not sufficient to improve the HB UL-94 rate of the samples. All blends consisting of EP, CE and phosphorus-containing flame retardant reached the V-0 UL-94 classification and

Table 3. LOI, UL-94 and mass loss calorimetry results of the composites made of CE and EP references and their blends

	LOI [V/V%]	UL-94*	TTI [s]	pHRR [kW/m^2]	THR [MJ/m^2]	Residue [mass%]
Matrix sample						
PT-30	30	HB	26	156	15.5	48
DGEBA	23	HB (17.1±2)	40	743	91.0	0
20% PT-30 - 80% DGEBA	33	HB	50	471	59.6	0
40% PT-30 - 60% DGEBA	28	HB	50	238	55.1	14
40% PT-30 - DGEBA – DOPO 2%P	43	V-0	53	195	36.3	23
40% PT-30 - DGEBA – DOPO 3%P	45	V-0	44	234	47.5	22
Composite sample						
PT-30	58	V-0	80	84	9.8	81
DGEBA	33	HB	55	176	37.9	50
20% PT-30 - 80% DGEBA	41	HB	51	162	29.9	61
40% PT-30 - 60% DGEBA	42	V-0	87	134	21.8	70
40% PT-30 - DGEBA – DOPO 2%P	46	V-0	72	101	20.1	67
40% PT-30 - DGEBA – DOPO 3%P	48	V-0	70	84	18.7	67

*in parenthesis the horizontal burning rate is showed, where measurable
LOI: limiting oxygen index, TTI: time to ignition, pHRR: peak of heat release rate, THR: total heat released
Flame retarded samples are highlighted in grey (2%P) and dark grey (3%P)

exhibited intensive intumescent charring and increased residual mass. Although the carbon fibre reinforcement plies hinder the solid phase intumescent mechanism of the phosphorus flame retardant [22], as the reinforcement itself is inflammable under the conditions of the flame retardancy tests, the composite specimens showed even better flame retardant properties than the polymer matrices alone. In composite specimens 40 mass% of PT-30 alone was sufficient to reach the V-0 UL-94 rate. By increasing the amount of CE and DOPO, the LOI increased and the pHRR values showed further decrease. The 40% PT-30 - DGEBA – DOPO 3%P composite had the same pHRR value, 84 kW/m^2 as the PT-30 reference composite.

3.3. Dynamic mechanical analysis of polymer matrices and composites

Storage modulus curves of the CE and EP references and CE/EP blends are displayed in Figure 3, while that of the composites can be seen in Figure 4. Glass transition temperature based on the tanδ peaks (T_g) and storage modulus (E') values at 25 and 75 °C are shown in Table 4.

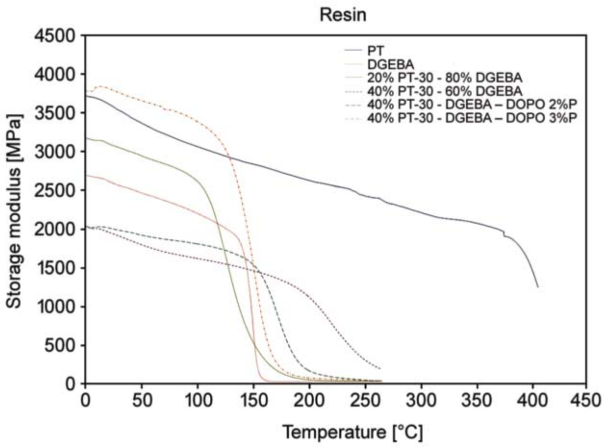

Figure 3. Storage modulus of the CE and EP references and CE/EP blends in the temperature range of 25–260 °C (in case of pure CE 25–400 °C)

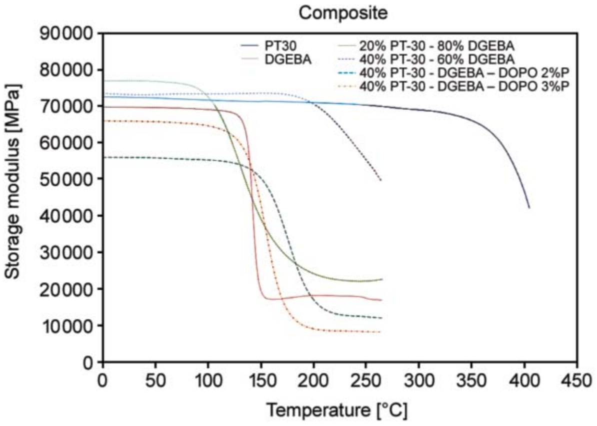

Figure 4. Storage modulus of the CE and EP reference and CE/EP blend composites in the temperature range of 25–260 °C (in case of pure CE 25–400 °C)

In case of resin samples by increasing the temperature the storage moduli showed a decreasing tendency, while in case of composite samples it remained in the same range at least up to 75 °C. As for the CE/EP resin blends, the 20% PT-30 - 80% DGEBA had higher storage modulus up to 115 °C, while the 40% PT-30 - 60% DGEBA blend showed better properties than DGEBA only above 140 °C, similarly to its flame retarded version with 2%P. However, the 40% PT-30 - DGEBA – DOPO 3%P matrix sample performed better than DGEBA in the whole temperature range, and had even higher storage modulus than CE up to 125 °C, which may be explained by the relative stoichiometric excess of PT-30 (related to the amount of oxirane groups present in DGEBA and DOPO-DGEBA components in the sample). In case of composite samples the 20% PT-30 - 80% DGEBA blend had higher storage modulus than CE up to 90 °C and higher than DGEBA up to 105 °C. The 40% PT-30 - 60% DGEBA composite per-

Table 4. Glass transition temperature (T_g) and storage modulus values at 25 and 75 °C of CE/EP matrices and composites determined by DMA

	Glass transition temperature [°C]		Storage modulus at 25 °C [MPa]		Storage modulus at 75 °C [MPa]	
Sample	**Matrix**	**Composite**	**Matrix**	**Composite**	**Matrix**	**Composite**
PT-30	401	394	3572	72 407	3196	71 908
DGEBA	155	145	2585	69 691	2343	69 407
20% PT-30 - 80% DGEBA	172	145	3071	92 311	2815	91 420
40% PT-30 - 60% DGEBA	247	249	1932	73 150	1686	73 360
40% PT-30 - DGEBA – DOPO 2%P	188	187	1995	55 967	1856	55 537
40% PT-30 - DGEBA – DOPO 3%P	165	167	3784	65 882	3534	65 378

formed similarly as CE up to 200 °C and outperformed DGEBA in the whole temperature range. The flame retarded composites showed somewhat lower storage modulus than DGEBA (except the 140–165 °C range in case of 40% PT-30 - DGEBA – DOPO 3%P composite, and the 140–190 °C range in case of 40% PT-30 - DGEBA – DOPO 2%P), most probably due to lower fibre-matrix adhesion (see the interlaminar shear properties in chapter 3.4.).

As for the glass transition temperatures (Table 4), in case of resin samples the T_g of the blends increased with increasing amount of CE. Compared to 40% PT-30 - 60% DGEBA sample, the inclusion of flame retardants decreased the T_g, most probably due to lower crosslinking density, however it was still above the T_g of DGEBA. In case of composite samples the T_g decreased in CE and EP reference samples and in 20% PT-30 - 80% DGEBA sample, while in 40% PT-30 containing composites, including the flame retarded ones, practically it remained the same value as in case of the matrix samples. Compared to DGEBA, the 40% PT-30 - DGEBA – DOPO 2%P composite showed 42 °C increase, while the 40% PT-30 - DGEBA – DOPO 3%P composite had still 22 °C higher T_g.

3.4. Tensile, bending, interlaminar shear and Charpy impact properties of polymer composites

Tensile properties of the CE and EP reference composites and CE/EP blend composites are shown in Table 5. According to the tensile test results, the inclusion of EP significantly increased the tensile strength of the rigid CE. More surprisingly, by adding DOPO-DGEBA adduct to the 40% PT-30 - 60% DGEBA matrix, the tensile strength of the 2% P-containing composite increased even further, and in case of 3% P-containing sample it still remained over the value of the CE reference. This amelioration may be attributed to better fibre-matrix adhesion and to the reactive nature of the flame retardant: by incorporating it by primary chemical bonds to the matrix itself, it does not migrate to the matrix surface either during high temperature processing or application. The strain at break increased to some extent in all blends containing DGEBA in comparison to the reference CE, decreasing the rigidity of it. The highest tensile modulus was reached in case of 20% PT-30 - 80% DGEBA, higher than the moduli of the blend components themselves. By adding DOPO-DGEBA adduct to the system, the tensile modulus slightly decreased.

Flexural properties of the CE and EP reference composites and CE/EP blend composites are shown in Table 6. According to the results the addition of EP into CE resulted in slightly higher flexural strength than in case of the reference CE and EP itself. The inclusion of DOPO-DGEBA adduct decreased the flexural strength and modulus, and increased the deformation at break, however taking into account the standard deviation values, the flexural strength and modulus of 40% PT-30 - DGEBA – DOPO 3% re-

Table 5. Tensile properties of the CE and EP reference composites and CE/EP blend composites

Composite sample	Tensile strength [MPa]	Strain at break [%]	Tensile modulus [GPa]
PT-30	689.2±100.9	4.43±0.60	27.7±0.7
DGEBA	912.6±45.7	5.35±0.43	26.8±2.4
20% PT-30 - 80% DGEBA	1040.9±43.0	5.66±0.22	28.8±0.2
40% PT-30 - 60% DGEBA	844.1±40.3	5.06±0.16	25.1±2.1
40% PT-30 - DGEBA – DOPO 2%P	861.2±54.7	5.73±0.47	24.9±0.4
40% PT-30 - DGEBA – DOPO 3%P	715.2±32.4	5.06±0.19	23.4±0.2

Table 6. Flexural properties of the CE and EP reference composites and CE/EP blend composites

Composite sample	Flexural strength [MPa]	Deformation at break [%]	Flexural modulus [GPa]
PT-30	1227.0±271.1	1.36±0.03	103.2±19.5
DGEBA	1203.0±115.9	1.36±0.09	98.2±4.3
20% PT-30 - 80% DGEBA	1240.1±114.3	1.36±0.04	100.1±10.9
40% PT-30 - 60% DGEBA	1238.5±79.2	1.37±0.04	98.2±8.8
40% PT-30 - DGEBA – DOPO 2%P	1056.2±54.1	1.43±0.02	79.5±5.0
40% PT-30 - DGEBA – DOPO 3%P	1149.0±96.7	1.45±0.09	96.0±10.9

mained in the same range as in case of CE and EP references.

In order to find an explanation for the tensile and flexural properties, the interlaminar shear strength of the composites was determined (Table 7). In accordance with the tensile and bending properties, the interlaminar shear strength values of the CE/EP blends were higher than in case of the CE and EP references. The inclusion of the polar phosphorus-containing flame retardant decreased the interlaminar shear strength, however these values were still well above the value of the reference CE composite.

Charpy impact test is suitable for comparing the impact resistance of the composites. The results of the instrumented Charpy unnotched impact measurements are given in Table 8. The impact strength of the 20% PT-30 - 80% DGEBA blend was practically the same as in case of DGEBA, however, the 40% PT-30 - 60% DGEBA blend had even higher impact strength than CE. By increasing the amount of flame retardants, the fracture toughness showed further increase in comparison to CE, meaning that the flame retarded composites are less brittle than the CE/EP blends and CE, EP references.

Table 7. Interlaminar shear strength of the CE and EP reference composites and CE/EP blend composites

Sample	Interlaminar shear strength [MPa]
PT-30	40.0±1.3
DGEBA	61.3±1.9
20% PT-30 - 80% DGEBA	66.8±3.1
40% PT-30 - 60% DGEBA	68.3±3.6
40% PT-30 - DGEBA – DOPO 2%P	53.4±2.0
40% PT-30 - DGEBA – DOPO 3%P	47.9±2.1

Table 8. Charpy impact strength of the CE and EP reference composites and CE/EP blend composites

Sample	Charpy impact strength [J/mm^2]
PT-30	90.1±8.0
DGEBA	84.3±5.2
20% PT-30 - 80% DGEBA	84.6±2.9
40% PT-30 - 60% DGEBA	98.3±32.0
40% PT-30 - DGEBA – DOPO 2%P	99.1±15.1
40% PT-30 - DGEBA – DOPO 3%P	113.7±14.0

4. Conclusions

Reactively flame retarded cyanate ester/epoxy resin (CE/EP) carbon fibre reinforced composites consisting of diglycidyl ether of bisphenol A (DGEBA), novolac type cyanate ester (CE) and an epoxy functional adduct of DGEBA and 9,10-dihydro-9-oxa-10-phosphaphenanthrene-10-oxide (DOPO) were prepared and tested. Influence of cyanate ester and flame retardant addition was determined on matrix viscosity, matrix and composite glass transition temperature (T_g), as well as composite mechanical properties.

From the tested CE/EP composites, the overall performance of V-0 UL-94 rated ones is summarized in Table 9. As expected, the T_g of the CE composite was the highest, however even the flame retarded CE/EP blends had at least 22 °C higher T_g than the benchmark DGEBA composite. As for the mechanical properties, the CE/EP blends outperformed the CE composite in most cases: The addition of EP considerably increased the tensile strength of the rigid CE, more unexpectedly, by adding DOPO-DGEBA adduct to the 40% PT-30 - 60% DGEBA matrix, the tensile strength of the 2% P-containing composite reached a 25% increase compared to the CE composite. The inclusion of EP into CE also resulted in slightly higher flexural strength than in case of the reference CE and EP itself, which was somewhat decreased by the DOPO-DGEBA adduct. These results may be interpreted by the better fibre-matrix adhesion: the interlaminar shear strength of the 40% PT-30 - 60% DGEBA blend was 70% higher than in case of the CE reference. Although the inclusion of the polar phosphorus-containing flame retardant decreased the interlaminar shear strength, their values were still high above the value of the CE composite. The impact strength also increased in comparison to

Table 9. Overall performance of UL-94 V-0 rated CE/EP composite samples (best achieved values are highlighted in bold)

Composite sample	Glass transition temperature [°C]	Tensile strength [MPa]	Flexural strength [MPa]	Interlaminar shear strength [MPa]	Charpy impact strength [J/mm^2]
PT-30	**394**	689.2±100.9	1227.0±271.1	40.0±1.3	90.1±8.0
40% PT-30 - 60% DGEBA	249	844.1±40.3	**1238.5±79.2**	**68.3±3.6**	98.3±32.0
40% PT-30 - DGEBA – DOPO 2%P	187	**861.2±54.7**	1056.2±54.1	53.4±2.0	99.1±15.1
40% PT-30 - DGEBA – DOPO 3%P	167	715.2±32.4	1149.0±96.7	47.9±2.1	**113.7±14.0**

CE, from all composites the flame retarded ones were the less brittle.

Acknowledgements

This work is connected to the scientific program of the 'Development of quality-oriented and harmonized R+D+I strategy and functional model at BME' project. The work reported in this paper has been developed in the framework of the project 'Talent care and cultivation in the scientific workshops of BME' project. Andrea Toldy and Gábor Szebényi acknowledge the financial support received through János Bolyai Scholarship of the Hungarian Academy of Science.

References

[1] Rakotomalala M., Wagner S., Döring M.: Recent developments in halogen free flame retardants for epoxy resins for electrical and electronic applications. Materials, **3**, 4300–4327 (2010).
DOI: 10.3390/ma3084300

[2] Toldy A.: Chemically modified flame retardant polymers. Express Polymer Letters, **3**, 267 (2009).
DOI: 10.3144/expresspolymlett.2009.33

[3] Levchik S. V., Camino G., Luda M. P., Costa L., Muller G., Costes B., Henry Y.: Epoxy resins cured with aminophenylmethylphosphine oxide 1: Combustion performance. Polymers for Advanced Technologies, **7**, 823–830 (1996).
DOI: 10.1002/(SICI)1099-1581(199611)7:11<823::AID-PAT498>3.0.CO;2-X

[4] Artner J., Ciesielski M., Walter O., Döring M., Perez R. M., Sandler J. K. W., Altstädt V., Schartel B.: A novel DOPO-based diamine as hardener and flame retardant for epoxy resin systems. Macromolecular Materials and Engineering, **293**, 503–514 (2008).
DOI: 10.1002/mame.200700287

[5] Hergenrother P. M., Thompson C. M., Smith J. G., Connell J. W., Hinkley J. A., Lyon R. E., Moulton R.: Flame retardant aircraft epoxy resins containing phosphorus. Polymer, **46**, 5012–5024 (2005).
DOI: 10.1016/j.polymer.2005.04.025

[6] Gérard C., Fontaine G., Bourbigot S.: New trends in reaction and resistance to fire of fire-retardant epoxies. Materials, **3**, 4476–4499 (2010).
DOI: 10.3390/ma3084476

[7] Walters R. N., Lyon R. E.: Fire-resistant cyanate ester–epoxy blends. Fire and Materials, **27**, 183–194 (2003).
DOI: 10.1002/fam.827

[8] Hamerton I., Hay J. N.: Recent developments in the chemistry of cyanate esters. Polymer International, **47**, 465–473 (1998).
DOI: 10.1002/(SICI)1097-0126(199812)47:4<465::AID-PI88>3.0.CO;2-S

[9] Martin M. D., Ormaetxea M., Harismendy I., Remiro P. M., Mondragon I.: Cure chemo-rheology of mixtures based on epoxy resins and ester cyanates. European Polymer Journal, **35**, 57–68 (1999).
DOI: 10.1016/S0014-3057(98)00095-0

[10] Toldy A.: Cyanate ester resins – 'Old newcomers' among high performance composite materials. Express Polymer Letters, **7**, 722 (2013).
DOI: 10.3144/expresspolymlett.2013.69

[11] Ho T-H., Hwang H-J., Shieh J-Y., Chung M-C.: Thermal and physical properties of flame-retardant epoxy resins containing 2-(6-oxido-6*H*-dibenz <*c*,*e*> <1,2> oxaphosphorin-6-yl)-1,4-naphthalenediol and cured with dicyanate ester. Polymer Degradation and Stability, **93**, 2077–2083 (2008).
DOI: 10.1016/j.polymdegradstab.2008.09.002

[12] Ho T-H., Hwang H-J., Shieh J-Y., Chung M-C.: Thermal, physical and flame-retardant properties of phosphorus-containing epoxy cured with cyanate ester. Reactive and Functional Polymers, **69**, 176–182 (2009).
DOI: 10.1016/j.reactfunctpolym.2008.12.019

[13] Lin C. H., Lin H. T., Tian Y. W., Dai S. A., Su W. C.: Preparation of phosphinated bisphenol from acid-fragmentation of 1,1,1-tris(4-hydroxyphenyl)ethane and its application in high-performance cyanate esters. Journal of Polymer Science Part A: Polymer Chemistry, **49**, 4851–4860 (2011).
DOI: 10.1002/pola.24936

[14] Lin C. H.: Synthesis of novel phosphorus-containing cyanate esters and their curing reaction with epoxy resin. Polymer, **45**, 7911–7926 (2004).
DOI: 10.1016/j.polymer.2004.09.023

[15] Chen X., Liang G., Gu A., Yuan L.: Flame retarding cyanate ester resin with low curing temperature, high thermal resistance, outstanding dielectric property, and low water absorption for high frequency and high speed printed circuit broads. Industrial and Engineering Chemistry Research, **54**, 1806–1815 (2015).
DOI: 10.1021/ie504333f

[16] Chang H. C., Lin H. T., Lin C. H.: Benzoxazine-based phosphinated bisphenols and their application in preparing flame-retardant, low dielectric cyanate ester thermosets. Polymer Chemistry, **3**, 970–978 (2012).
DOI: 10.1039/c2py00528j

[17] Krishnadevi K., Nirmala Grace A., Alagar M., Selvaraj V.: Development of hexa (aminophenyl)cyclotriphosphazene-modified cyanate ester composites for high-temperature applications. High Performance Polymers, **26**, 89–96 (2014).
DOI: 10.1177/0954008313500058

[18] Toldy A., Szlancsik Á., Szolnoki B.: Reactive flame retardancy of cyanate ester/epoxy resin blends and their carbon fibre reinforced composites. Polymer Degradation and Stability, **128**, 29–38 (2016).
DOI: 10.1016/j.polymdegradstab.2016.02.015

[19] Wang C. S., Lin C. H.: Synthesis and properties of phosphorus-containing epoxy resins by novel method. Journal of Polymer Science Part A: Polymer Chemistry, **37**, 3903–3909 (1999).
DOI: 10.1002/(SICI)1099-0518(19991101)37:21<3903::AID-POLA4>3.0.CO;2-X

[20] Bauer M., Bauer J.: *Co*-reactions of cyanate esters with epoxies. in 'Chemistry and technology of cyanate ester resins' (ed.: Hamerton I.) Chapman and Hall, London, 77–82 (1994).

[21] Hay J. N.: Processing and cure schedules for cyanate ester resins. in 'Chemistry and technology of cyanate ester resins' (ed.: Hamerton I.) Chapman and Hall, London, 151–192 (1994).

[22] Toldy A., Szolnoki B., Marosi Gy.: Flame retardancy of fibre-reinforced epoxy resin composites for aerospace applications. Polymer Degradation and Stability, **96**, 371–376 (2011).
DOI: 10.1016/j.polymdegradstab.2010.03.021

eXPRESS Polymer Letters Vol.10, No.12 (2016) 1026–1033
Available online at www.expresspolymlett.com
DOI: 10.3144/expresspolymlett.2016.95

Copolymerization of 4-methyl-1-pentene with α,ω-alkenols

W. Wang[*]*, L. Hou, J. Sheng, M. Ren, Y. Tang*

Institute of Materials Science, Beijing Research Institute of Chemical Industry (BRICI), Sinopec, No. 14 Beisanhuan Donglu, Chao Yang District, 100013 Beijing, China

Received 16 June 2016; accepted in revised form 25 July 2016

Abstract. Copolymerization of 4-methyl-1-pentene (4M1P) with 9-decen-1-ol (9D1O) or 4-penten-1-ol (4P1O) was conducted by using metallocene catalysts. The activity could be improved under the higher polymerization temperature. The dyad distribution of poly(4M1P-*co*-4P1O) was presented. The results showed that 4P1O was uniformly distributed in the copolymer chain. The melting temperature (T_m) of the copolymer was lower than that of poly(4M1P), and was decreased with the increase of the incorporation of comonomer. T_m of poly(4M1P-*co*-4P1O) was determined as 185 °C, even the incorporation of 4P1O was high as 15.0 mol%. WAXD (wide-angle X-ray diffraction) results showed that the poly(4M1P) was observed as crystalline form II, and turned to form I when the incorporation of α,ω-alkenols were high. Some new peaks, which were never observed in the previous researches, appeared in the X-ray diffraction profiles for poly(4M1P-*co*-4P1O). It is inferred that the similar chain length of 4P1O and 4M1P may be the key factor.

Keywords: *polymer synthesis, molecular engineering, 4-methyl-1-pentene, α,ω-alkenols, copolymerization*

1. Introduction

The synthesis of polyolefin with functional groups was considered as an important and pioneering area, due to the unique and excellent properties of the modified polymer superior to the traditional material [1]. The incorporation of polar groups into the polyolefin chain is believed to provide a polymer with improved surface properties [2]. Such material is desired because it combines the polarity and non-polarity into an integral whole. It could be utilized extensively as the modifier of a polymer to improve the property; furthermore, it could be hopefully used in the areas of energy, information and environmental protection [3]. Direct copolymerization of olefin monomer with vinyl comonomer with a polar group(s) by using Ziegler-Natta polymerization is straightforward and efficient to obtain these functional polyolefin materials. Polyethylene and polypropylene are the polyolefin resins with the largest commercial scale. It follows then that most researches on the synthesis of the functional polyolefin concern ethylene [4–13] and propylene [14–18] copolymerization. The investigation on the copolymerization of higher α-olefin with functional monomer was rather rare.

Studies on the polymerization of higher α-olefin have drawn considerable attention for long years. Polymerization of either linear or branched α-olefin has been fully explored by using various catalyst systems, including the traditional Ziegler-Natta catalyst [19, 20], metallocene catalyst [21–24], non-metallocene single-site catalyst [25] and later transition metal catalyst [26, 27]. Properties of poly(α-olefin) could be improved by incorporating the second monomer with a functional group, but the successful examples were limited so far [28, 29].

Previously, we reported the synthesis of the copolymer of ethylene with the hydroxyl-ended vinyl mono-

---

[*] Corresponding author, e-mail: wangw.bjhy@sinopec.com

mers by using half titanocene catalysts [12, 13]. In those works, we gave the detailed ^{13}C-NMR (nuclear magnetic resonance) analysis and the sequence distribution of the copolymer of ethylene with α,ω-alkenols for the first time. Furthermore, we found the influence of the functional group of the comonomer on the structure of the resulted copolymer could be reduced by the methylene spacers between the vinyl bond and the functional group. Because of the lack of research on the copolymerization of higher α-olefin and the functional comonomer, we have the interest to set foot in this subject. In the present work, we would introduce the copolymerization of 4-methyl-1-pentene (4M1P) with 4-penten-1-ol (4P1O) and 9-decen-1-ol (9D1O).

2. Experimental section

All experiments were carried out under a nitrogen atmosphere in a Vacuum Atmospheres drybox or using standard Schlenk techniques, unless otherwise specified. All chemicals used were of reagent grade and were purified by the standard purification procedures. Toluene was distilled in the presence of sodium and benzophenone under a nitrogen atmosphere, and was stored in a Schlenk tube in the drybox over molecular sieves. Metallocene catalysts, *rac*-$Me_2Si(2\text{-}Me\text{-}Ind)_2ZrCl_2$ (99%) was purchased from Boulder Scientific Company (CO, USA), and *rac*-$Me_2Si(2\text{-}Me\text{-}4\text{-}Ph\text{-}Ind)_2ZrCl_2$ (99%) from APAC Pharmaceutical (MD, USA). MAO (Methylaluminoxane) solution in toluene (10 wt%) was purchased from Albemarle (LA, USA), 4-methyl-1-pentene (4M1P, 98+%), 9-decen-1-ol (9D1O, 99%) and 4-penten-1-ol (4P1O, 99%) from TCI (Japan), and were used as received.

Polymerization was conducted in toluene in a 100 mL glass reactor with an oil bath. The glass reactor was purged with nitrogen and charged with a nitrogen atmosphere. For example run 1 in Table 1, keeping the oil bath at 25 °C, toluene (5 mL), 4M1P (3.0 mL, 23.7 mmol) were introduced. And then MAO solution (6 mL, 10 mmol) and *rac*-$Me_2Si(2\text{-}Me\text{-}Ind)_2ZrCl_2$ solution in toluene (1 mL, 10 μmol) were injected to start the polymerization. The mixture was stirred magnetically for 20 hours. Subsequently, the mixture was poured into ethanol containing concentrated hydrochloric acid and stirred for 6 hours. The resultant polymer was gathered on a filter paper by filtration, and washed thoroughly with EtOH, and was then dried in vacuo under 60 °C for 24 hours. 1.56 g of polymer was obtained.

The molecular weight was determined by using gel permeation chromatography (GPC, polystyrene calibration) on a Waters Alliance GPCV2000 at 150 °C with 1, 2, 4-trichlorobenzene as the eluent, and the infrared (IR) as the detector.

The melting temperature of the polymer was determined on TAQ 100. Approximately 2 mg of polymer sample was heated from room temperature to 240 °C with a heating rate of 10 °C per minute, under a nitrogen atmosphere. After keeping the temperature for 1 minute, the sample was cooled down to room temperature, and kept the temperature for 1 minute again. Then sample was heated to 240 °C with a heating rate of 10 °C per minute and the data was recorded.

Solution ^{13}C-NMR experiments were performed on a Bruker AVANCEIII-400 MHz spectrometer with a 10 mm PASEX $^{13}C\text{-}^{1}H/D$ Z-GRD probe. Sample solutions were prepared with approximately 250 mg of the polymer material dissolved in 2.5 ml of d_4-o-dichrolobenzene (ODCB-d_4) in a 10 mm tube at 130 °C. All ^{13}C-NMR experiments were carried out at 125 °C, 20 Hz spinning rate, 90° pulse angle, continuous Waltz-16 decoupling, 120 ppm spectral width, 5 s acquisition time, and 10 s relaxation delay.

Wide Angle X-ray Diffraction (WAXD) experiment was carried out on a Bruker D8 DISCOVER 2D X-ray diffractometer. The X-ray was generated using IS micro Focus X-ray source incorporating a 50 W sealed-tube X-ray generator with Cu target. The wavelength was 0.1542 nm. The power of the generator used for measurement was 45 kV and 0.9 mA. The X-ray intensities were recorded on a VÅNTEC-500 2D detector system with a pixel size of 68×68 μm^2. The distance from the sample to detector was 198 mm. The spot size of the beam was 0.5 mm. The exposure time was 2 min. Polymer powder was used as generated without other treatment.

3. Results and discussion

Copolymerization of 4M1P with 9D1O or 4P1O were conducted by using *rac*-$Me_2Si(2\text{-}Me\text{-}Ind)_2ZrCl_2$/MAO as the catalyst system, and the results were summarized in Table 1.

For both the homopolymerization and copolymerization, the higher was the polymerization tempera-

Table 1. Copolymerization of 4M1P with 4P1O or 9D1O[a]

Run	Cat [µmol]	Al/Zr	Comono. [mmol]	*T* [°C]	*t*	Act.[b]	M_w[c] [k]	*pdi*[c]	T_m[d] [°C]	Incorp.[e] [mol%]
1	10	1000	–	25	20 hrs	7.8	17.1	2.2	222	–
2	10	1000	–	50	3 hrs	36.0	10.0	2.0	211	–
3	50	400	9D1O, 2.80	25	2 hrs	8.3	8.4	1.8	n.d.[f]	–[g]
4	50	400	9D1O, 2.80	50	20 min	51.0	5.7	1.7	n.d.[f]	8.8
5	20	1000	9D1O, 0.56	50	20 min	96.0	8.2	1.8	183	3.9
6	20	1000	9D1O, 1.68	50	20 min	79.5	8.0	1.7	171	7.9
7	20	1000	9D1O, 2.80	50	20 min	57.0	7.3	1.6	n.d.[f]	–[g]
8	20	750	4P1O, 1.94	25	20 hrs	1.8	18.5	2.1	223	1.2

[a]Polymerization conditions: catalyst *rac*-$Me_2Si(2\text{-}Me\text{-}Ind)_2ZrCl_2$, MAO cocatalyst, 4M1P 23.7 mmol, in toluene, total volume 15 mL; [b]Activity in kg-polymer/mol-Zr/hr; [c]GPC data; [d]Melting temperature, determined by DSC; [e]Comonomer incorporation, estimated by ^{13}C-NMR; [f]No melting point; [g]Not determined.

ture, the higher was the activity. Introduction of 9D1O into the polymerization system increased the activity. Analogous result was often observed in the olefin copolymerization [30]. The activity decreased while the 9D1O feeding amount increased (run 5–7). The so-called 'comonomer effect' has been observed in several manners for the ethylene copolymerization with α-olefin [30, 31]. The incorporation of 9D1O into the polymer chain improved the solubility of the resulteding polymer in the reaction mixture; therefore the resistance of the mass and heat transfer would be reduced, leading to the increased activity. On the other hand, because the lone pair electrons on the oxygen atom would coordinate to the catalytic centre and kill the active species, the higher concentration of 9D1O would depress the activity, although the effect of long chain monomer could be reduced by the methylene spacers [13]. 4P1O possesses less methylene spacers, with the consequence that the activity was much lower than the homopolymerization of 4M1P and the copolymerization of 4M1P and 9D1O.

All polymer samples were obtained with narrow molecular weight distribution. The molecular weight was not high. It was lower at higher polymerization temperature, because the chain transfer reaction would be more drastic at high temperature. When the comonomer feeding concentration increased, the molecular weight of the resulted polymer also became lower. The high concentration of comonomer probably resulted in a larger probability of the terminal reaction due to the coordination of the oxygen atom to the active species, which followed by the lowered molecular weight of the polymer.

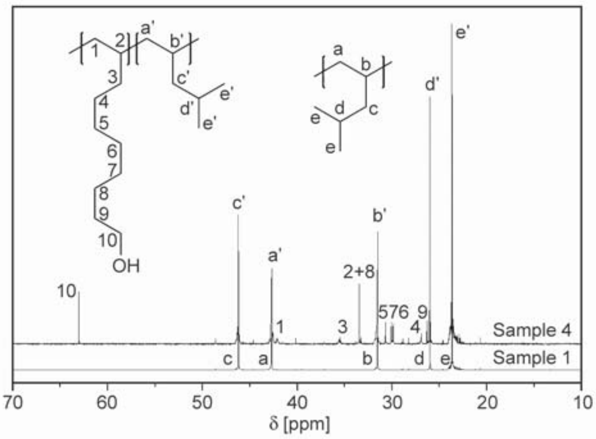

Figure 1. ^{13}C-NMR spectra of sample 1 and sample 4

The ^{13}C-NMR spectrum of sample was shown in Figure 1. Five main peaks were observed in δ = 46.2, 42.7, 31.5, 26.0, 23.7 ppm, corresponding to the five carbon atoms of 4M1P [24]. ^{13}C-NMR spectrum of sample 4 was also shown in Figure 1. Besides the similar peaks to that of sample 1, other some resonances appeared in the spectrum. The peak at 63.0 ppm is the typical resonance of the carbon atom adjacent to the hydroxyl group of 9D1O [9, 13]. Other resonances, δ = 42.1, 35.5, 33.4, 30.7, 30.0, 29.8, 26.9, 26.3 ppm, are assigned to the other carbon atoms of 9D1O. Calculation according to the integrated intensity showed that 8.8 mol% of 9D1O was incorporated into the copolymer. The incorporation of 9D1O in samples 5 and 6 was calculated as 3.9 and 7.9 mol%, respectively. By using the similar calculation method, the incorporation of 4P1O of sample 8 was found as 1.2 mol%.

The melting point (T_m) of the homopolymer of 4M1P produced at 25 °C was determined as 222 °C, and higher polymerization temperature gave a polymer with the lower T_m. The results tallied with the previously reported values [24].

T_ms of the copolymer of 4M1P with 9D1O were lower than that of the homopolymer of 4M1P, and when the feeding amount of 9D1O increased, T_m decreased (see Figure 2). Furthermore, whereas sample 1 displayed a single melting endotherm, samples 2, 5, and 6 exhibited a shoulder peak or multiple melting endotherms in the DSC curves. This phenomenon was observed in the stereoregular polymer produced by the less stereospecific catalyst systems [32]. The broadened melting range of sample 2 indicated that the isospecificity of the catalyst was weakened under the higher polymerization temperature. On the other hand, incorporation of comonomers would interrupt the successive insertion of the crystallizable monomer unit, resulting in the decreased melting point and the inhomogeneity of the crystallizable segment. The multiple melting endotherm in the DSC curve could be attributed to the process of melting, recrystallization and remelting: metastable crystallites are recrystallized into a more perfect form following the initial melting [24, 32].

While the T_ms of the copolymers of 4M1P and 9D1O were lower than that of the homopolymer of 4M1P, and decreased with the increase of the 9D1O incorporation, it was surprisingly found that the T_m of the copolymer of 4M1P with 4P1O was almost equal to or a little bit higher than that of the homopolymer of 4M1P.

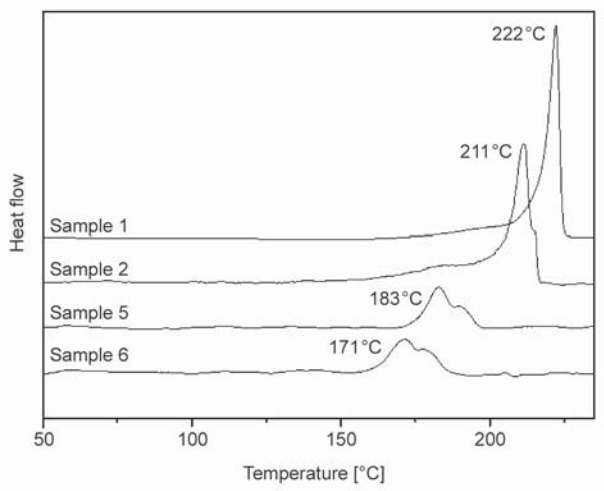

Figure 2. DSC curves of the copolymers of 4M1P with 9D1O

To some extent, the comonomer 4P1O is different from the other one 9D1O. The chain length of 4P1O is much shorter than 9D1O; more importantly, the chain length is closer to that of 4M1P. It is attractive enough to inspire us to explore more details of this copolymerization.

Another metallocene, *rac*-Me$_2$Si(2-Me-4-Ph-Ind)$_2$ZrCl$_2$, was used as the catalyst for copolymerization of 4M1P and 4P1O, and the results were summarized in Table 2. The experiments were designed for producing the copolymer with the high incorporation of 4P1O. Although the catalyst, *rac*-Me$_2$Si(2-Me-4-Ph-Ind)$_2$ZrCl$_2$, exhibited high activity and offered the polymer with the high molecular weight in propylene polymerization [33], the activity for the copolymerization of 4M1P was pretty low, and the molecular weight of the resulted polymer was also low.

The ^{13}C-NMR spectrum of the copolymer of 4M1P with 4P1O (sample 9) was given in Figure 3, in comparison to that of sample 1. The carbon atoms of 4M1P unit gave the nearly identical resonances with the homopolymer. In addition, peaks at $\delta = 63.53$ and 30.45 ppm were corresponding to the two carbon atoms adjacent to the hydroxyl group of 4P1O. The resonance of the branched carbon atom appeared at 33.05 ppm. The signals at the range of 41.3~42.7 ppm would be assigned to the [αα] structure. The resonance of the carbon atom closed to the branch should be overlapped by the backbone carbon of 4M1P. All assignments were depicted in Figure 3, as well as summarized in Table 3. 'P' and 'O' are used to represent 4M1P and 4P1O monomer unit respectively. The dyad sequence distributions for all copolymer of 4M1P and 4P1O were presented in Table 4. The products of the reactive ratios, r_Pr_O, were calculated as 1.22 and 1.38 for samples 9 and 10, respectively. It

Table 2. Copolymerization of 4M1P with 4P1O[a]

Run	4M1P [mmol]	4P1O [mmol]	Act.[b]	M_w[c] [k]	*pdi*[c]	T_m[d] [°C]	Incorp.[e] [mol%]
9	6.32	1.94	0.77	4.9	1.7	199	9.7
10	4.74	3.87	0.48	4.0	1.5	185	15.0

[a]Polymerization conditions: catalyst *rac*-Me$_2$Si(2-Me-4-Ph-Ind)$_2$ZrCl$_2$, 20 µmol, MAO cocatalyst 10 mmol, Al/Zr = 500, in toluene, total volume 15 mL, 25 °C, 24 hrs; [b]Activity in kg-polymer/mol-Zr/hr; [c]GPC data; [d]Melting temperature, determined by DSC; [e]Comonomer incorporation, estimated by ^{13}C-NMR.

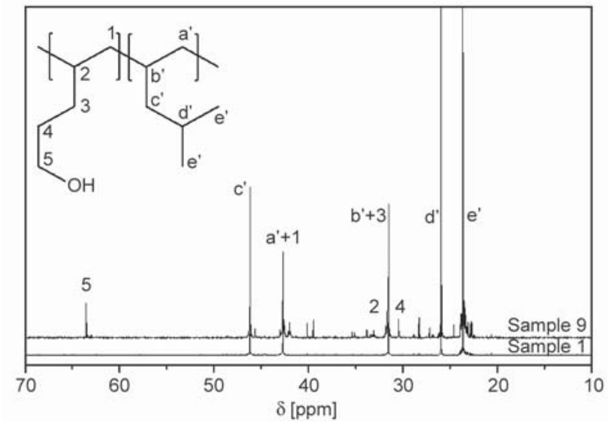

Figure 3. ^{13}C-NMR spectra of sample 1 and sample 9

means that the structure of the copolymer is still random. Another parameter RMD (Relative Monomer Dispersity) [34], developed on the base of Hsieh and Randall's work [35], was also calculated. All RMD for the three copolymer samples were obtained as 100% or thereabouts, indicating that the comonomer, 4P1O, is uniformly distributed in the polymer chain. This coincides that we concluded from the analysis of the products of reactive ratios.

It is worth noting that even in the copolymer (sample 10) containing a high 4P1O unit fraction of 15.0 mol%, the T_m of the polymer was still high as 185 °C. The results echoed the high T_m of the sample with the low 4P1O incorporation (sample 8). The performance is distinct from the observation of the copolymer of 4M1P with 9D1O. To search to the bottom, the reason probably lies in the chain length of the functional monomer.

Table 3. ^{13}C-NMR assignments of copolymer of 4M1P with 4P1O

Carbon	Sequence	Main Peak
B(–CH$_2$–OH)	[O]	63.53
3B(P)	[P]	46.16
$\alpha_P\alpha_P$	[PP]	42.67
$\alpha_P\alpha_O$	[PO]	41.98
$\alpha_O\alpha_O$	[OO]	41.31
CH(O)	[O]	33.05
CH(P)+3B(O)	[P]+[O]	31.49
2B(O)	[O]	30.45
2B(P)	[P]	25.94
1B(P)	2[P]	23.60

Table 4. Sequence distributions of Poly(4M1P-*co*-4P1O)

Run	[P]	[O]	[PO]	[PP]	[OO]	$r_P r_O$	RMD [%]
8	98.8	1.2	2.4	97.6	0	0	101.2
9	90.3	9.7	17.2	81.7	1.1	1.22	98.4
10	85.0	15.0	24.3	72.9	2.8	1.38	95.4

As we can summarize the data in references, for olefin copolymer, for example propylene copolymer with higher α-olefin, the melting temperature is always lower than that of homopolypropylene. It is natural because the incorporation of a comonomer would interrupt the crystallization of the successive propylene unit, therefore reduce the lamellar crystal. However, if the chain length of the comonomer is closer to the main monomer, the impact would become weak. The change of the melting temperature of the propylene copolymer with 1-butene [36], 1-hexene [37, 38], 1-octene [37] and 1-decene [37] showed that, the incorporation of the shorter comonomer would be less efficient to decrease the melting temperature of the copolymer. Previous research revealed that 1-butene was more inclined to be incorporated into the crystalline phase than ethylene, 1-hexene and 1-octene for propylene copolymers [39]. It could be probably concluded that, if the length of the comonomer was extremely close to the main monomer, the melting temperature of the copolymer would not decrease, without consideration of the polarity of the monomers.

It is difficult to find or design such a comonomer for ethylene or propylene copolymerization, but is possible for the copolymerization of higher α-olefin. The unusual melting temperature of the copolymer of 4M1P with 4P1O, especially the example with the high incorporation, gave evidence for the above-mentioned deduction. Because of the parallel chain lengths, the major monomer (4M1P) unit tolerates the incorporation of the minor comonomer (4P1O) into the lamella, although the loss of the lamellar thickness is unavoidable. Apart from this, the additional adhesion provided by the hydrogen bond of the hydroxyl group of 4P1O increases the thermal consumption in the melting process; therefore increases the melting temperature.

X-ray powder diffraction was used to characterize the crystal structure of the polymer samples (see Figure 4). The homopolymer of 4M1P, sample 2, was affirmed as crystalline form II, according to the literature [40]. Polymer sample with low 9D1O incorporation (sample 5, 9D1O 3.7 mol%) gave a similar profile, implying that few changes occurred in the

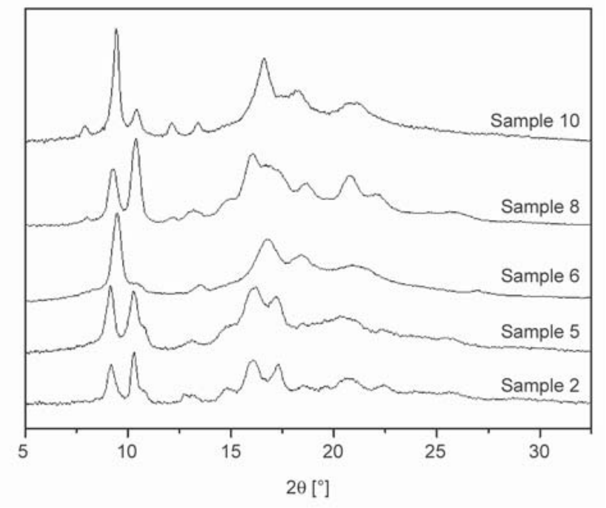

Figure 4. X-ray powder diffraction profiles of polymer samples

crystal structure. High 9D1O incorporation brought significant change to the crystal structure. When the incorporation of 9D1O was 7.9 mol%, the X-ray profile indicated that the crystalline was detected as form I of poly(4M1P) [40]. Polymer sample 8, with the low 4P1O incorporation, gave the small but important changes in the X-ray profile. The peaks between 12~14° had the tendency of splitting. The most important is that a new peak appeared at 2θ = 7.9°, which was never observed in all the five crystalline forms of poly(4-methyl-1-pentene) found. [40, 41] While the incorporation of 4P1O was high as 15.0 mol%, the new appeared peak at 2θ = 7.9° was distinctly observed, and the peak between 12~14° evidently split at 2θ = 12.2 and 13.4°. Comparing the patterns of samples 6 and 10, it could be found that the pattern of the latter is similar to the former, besides the peaks at 2θ = 7.9 and 12.2°. It is supposed that there are the mixed crystal forms in sample 10, including the form I of poly(4-methyl-1-pentene) and an unidentified one. It may be concluded that the high incorporation of α,ω-alkenol, either 9D1O or 4P1O, turns the crystalline from form II to form I. Because all samples for WAXD were directly generated from the polymerization without any treatment, it may be reasonably inferred that the high incorporation of α,ω-alkenol changed the crystallization process of the copolymer. The reason for the new peaks could be ascribed to the incorporation of 4P1O, no matter how much it was incorporated. Because such result could not be observed in the case of copolymerization of 9D1O, the difference of the chain length of the α,ω-alkenol may play the important role.

4. Conclusions

We have described the copolymerization of 4M1P with α,ω-alkenol, namely 9D1O and 4P1O, by using the metallocene catalysts. T_m of polymer decreased with the increase of the incorporation of comonomers. While T_m of the copolymer of 9D1O sharply decreased with the incorporation of 9D1O, T_m of 4P1O maintained the high level, even the incorporation was high as 15.0 mol%. Results of WAXD indicate the high incorporation of α,ω-alkenol would result in the transformation of the crystalline of the polymer from the form II to form I. Furthermore, the incorporation of 4P1O led to the appearance of new peaks in the X-ray diffraction patterns. The unique observation may be ascribed to the comparable length of 4M1P and 4P1O.

References

[1] Boffa L. S., Novak B. M.: Copolymerization of polar monomers with olefins using transition-metal complexes. Chemical Reviews, **100**, 1479–1494 (2000). DOI: 10.1021/cr990251u

[2] Ittel S. D., Johnson L. K., Brookhart M.: Late-metal catalysts for ethylene homo- and copolymerization. Chemical Reviews, **100**, 1169–1204 (2000). DOI: 10.1021/cr9804644

[3] Chung T. C. M.: Functional polyolefins for energy applications. Macromolecules, **46**, 6671–6698 (2013). DOI: 10.1021/ma401244t

[4] Younkin T. R., Connor E. F., Henderson J. I., Friedlich S. K., Grubbs R. H., Bansleben D. A.: Neutral, single-component nickel(II) polyolefin catalysts that tolerate heteroatoms. Science, **287**, 460–462 (2000). DOI: 10.1126/science.287.5452.460

[5] Luo S., Vela J., Lief G. R., Jordan R. F.: Copolymerization of ethylene and alkyl vinyl ethers by a (phosphine-sulfonate)PdMe catalyst. Journal of the American Chemical Society, **129**, 8946–8947 (2007). DOI: 10.1021/ja072562p

[6] Daigle J-C., Piche L., Arnold A., Claverie J. P.: Probing the regiochemistry of acrylate catalytic insertion polymerization via cyclocopolymerization of allyl acrylate and ethylene. ACS Macro Letters, **1**, 343–346 (2012). DOI: 10.1021/mz200242j

[7] Wucher P., Goldbach V., Mecking S.: Electronic influences in phosphinesulfonato palladium(II) polymerization catalysts. Organometallics, **32**, 4516–4522 (2013). DOI: 10.1021/om400297x

[8] Daigle J-C., Piche L., Claverie J. P.: Preparation of functional polyethylenes by catalytic copolymerization. Macromolecules, **44**, 1760–1762 (2011).
DOI: 10.1021/ma200131e

[9] Xu B-C., Hu T., Wu J-Q,, Hu N-H., Li Y-S.: Novel vanadium(III) complexes with bidentate *N,N*-chelating iminopyrrolide ligands: Synthesis, characterization and catalytic behaviour of ethylene polymerization and copolymerization with 10-undecen-1-ol. Dalton Transactions, **38**, 8854–8863 (2009).
DOI: 10.1039/B909495D

[10] Mu J-S., Liu J-Y., Liu S-R., Li Y-S.: Copolymerizations of ethylene with α-olefin-ω-ols by highly active vanadium(III) catalysts bearing [N,O] bidentate chelated ligands. Polymer, **50**, 5059–5064 (2009).
DOI: 10.1016/j.polymer.2009.09.003

[11] Yang X-H., Liu C-R., Wang C., Sun X-L., Guo Y-H., Yang X-K., Yang Z., Xie Z., Tang Y.: $[\text{O}^{-}\text{NS}^{\text{R}}]\text{TiCl}_3$-catalyzed copolymerization of ethylene with functionalized olefins. Angewandte Chemie, International Edition, **48**, 8099–8102 (2009).
DOI: 10.1002/anie.200903334

[12] Wang W., Hou L., Luo S., Zheng G., Wang H.: Synthesis and ^{13}C NMR spectroscopy analysis of ethylene copolymer with high content of 4-penten-1-ol. Macromolecular Chemistry and Physics, **214**, 2245–2249 (2013).
DOI: 10.1002/macp.201300350

[13] Hou L., Wang W., Sheng J., Liu C.: Synthesis and ^{13}C-NMR analysis of an ethylene copolymer with 9-decen-1-ol. RSC Advances, **5**, 98929–98933 (2015).
DOI: 10.1039/C5RA20007E

[14] Nakano R., Nozaki K.: Copolymerization of propylene and polar monomers using Pd/IzQO catalysts. Journal of the American Chemical Society, **137**, 10934–10937 (2015).
DOI: 10.1021/jacs.5b06948

[15] Zhang G., Li H., Antensteiner M., Chung T. C. M.: Synthesis of functional polypropylene containing hindered phenol stabilizers and applications in metallized polymer film capacitors. Macromolecules, **48**, 2925–2934 (2015).
DOI: 10.1021/acs.macromol.5b00439

[16] Wang X., Wang Y., Shi X., Liu J., Chen C., Li Y.: Syntheses of well-defined functional isotactic polypropylenes via efficient copolymerization of propylene with ω-halo-α-alkenes by post-metallocene hafnium catalyst. Macromolecules, **47**, 552–559 (2014).
DOI: 10.1021/ma4022696

[17] Sahre K., Schulze U., Eichhorn K-J., Voit B.: Kinetic studies of metallocene-catalyzed copolymerization of propene with 10-undecene-1-ol using in-line FTIR spectroscopy. Macromolecular Chemistry and Physics, **208**, 1265–1273 (2007).
DOI: 10.1002/macp.200700145

[18] Zhao P., Shpasser D., Eisen M. S.: Copolymerizations of propylene with functionalized long-chain α-olefins using group 4 organometallic catalysts and their membrane application. Journal of Polymer Science Part A: Polymer Chemistry, **50**, 523–533 (2012).
DOI: 10.1002/pola.25060

[19] Buono A., Talarico G., de Rosa C., Thierry A., Lotz B.: Crystal polymorphism and crystal transformations of isotactic poly(5-methylhexene-1). Macromolecules, **46**, 4872–4881 (2013).
DOI: 10.1021/ma4005296

[20] Ricci G., Leone G., Rapallo A., Biagini P., Guglielmetti G., Porri L.: Syndiospecific oligomerization and polymerization of norbornene with titanium catalysts. Polymer, **52**, 5708–5716 (2011).
DOI: 10.1016/j.polymer.2011.10.029

[21] Galland G. B., Da Silva L. F., Nicolini A.: Tacticity of poly-α-olefins from poly-1-hexene to poly-1-octadecene. Journal of Polymer Science Part A: Polymer Chemistry, **43**, 4744–4753 (2005).
DOI: 10.1002/pola.20989

[22] Park J. H., Jang Y. E., Jeon J. Y., Go M. J., Lee J., Kim S. K., Lee S., Lee B. Y.: Preparation of *ansa*-metallocenes for production of poly(α-olefin) lubricants. Dalton Transactions, **43**, 10132–10138 (2014).
DOI: 10.1039/C4DT00997E

[23] Hu W., Hagihara H., Miyoshi T.: Microstructure and thermal property of isotactic poly(3-methyl-1-butene) obtained using the C_2-symmetrical zirconocene/MAO catalyst system. Macromolecules, **40**, 1763–1766 (2007).
DOI: 10.1021/ma062121a

[24] Descour C., Duchateau R., Mosia M. R., Gruter J-G. M., Severn J. R., Rastogi S.: Catalyst behaviour for 1-pentene and 4-methyl-1-pentene polymerisation for C_2-, C_s- and C_1-symmetric zirconocenes. Polymer Chemistry, **2**, 2261–2272 (2011).
DOI: 10.1039/C1PY00257K

[25] Steelman D. K., Xiong S., Pletcher P. D., Smith E., Switzer J. M., Medvedev G. A., Delgass D. N., Caruthers J. M., Abu-Omar M. M.: Effects of pendant ligand binding affinity on chain transfer for 1-hexene polymerization catalyzed by single-site zirconium amine bis-phenolate complexes. Journal of the American Chemical Society, **135**, 6280–6288 (2013).
DOI: 10.1021/ja401474v

[26] Liu J., Chen D., Wu H., Xiao Z., Gao H., Zhu F., Wu Q.: Polymerization of α-olefins using a camphyl α-diimine nickel catalyst at elevated temperature. Macromolecules, **47**, 3325–3331 (2014).
DOI: 10.1021/ma5004634

[27] Azoulay J. D., Schneider Y., Galland G. B., Bazan G. C.: Living polymerization of ethylene and α-olefins using a nickel α-keto-β-diimine initiator. Chemical Communications, **2009**, 6177–6179 (2009).
DOI: 10.1039/B912743G

[28] Stehling U. M., Stein K. M., Fischer D., Waymouth R. M.: Metallocene/borate-catalyzed copolymerization of 5-*N*,*N*-diisopropylamino-1-pentene with 1-hexene or 4-methyl-1-pentene. Macromolecules, **32**, 14–20 (1999). DOI: 10.1021/ma980856c

[29] Kisun'ko D. A., Lemenovskii D. A., Aladyshev A. M.: Synthesis of isotactic copolymers of 4-methyl-1-pentene by living polymerization catalyzed by zirconium non-metallocene complexes. Polymer Science Series A, **48**, 1227–1231 (2006). DOI: 10.1134/S0965545X06120017

[30] Wang W., Fan Z-Q., Feng L-X., Li C-H.: Substituent effect of bisindenyl zirconene catalyst on ethylene/1-hexene copolymerization and propylene polymerization. European Polymer Journal, **41**, 83–89 (2005). DOI: 10.1016/j.eurpolymj.2004.08.002

[31] Quijada R., Narváez R. A., Rojas R., Rabagliati F. M., Galland G. B., Mauler R. S., Benavente R., Pérez E., Pereña J. M., Bello A.: Synthesis and characterization of copolymers of ethylene and 1-octadecene using the *rac*-$Et(Ind)_2ZrCl_2$/MAO catalyst system. Macromolecular Chemistry and Physics, **200**, 1306–1310 (1999). DOI: 10.1002/(SICI)1521-3935(19990601)200:6<1306::AID-MACP1306>3.0.CO;2-4

[32] Bassett D. C., Patel D.: Isothermal lamellar thickening and the distribution of thermal stability in spherulitic isotactic poly(4-methylpentene-1). Polymer, **35**, 1855–1962 (1994). DOI: 10.1016/0032-3861(94)90974-1

[33] Spaleck W., Küber F., Winter A., Rohrmann J., Bachmann B., Antberg M., Dolle M., Paulus E.: The influence of aromatic substituents on the polymerization behavior of bridged zirconocene catalysts. Organometallics, **13**, 954–963 (1994). DOI: 10.1021/om00015a032

[34] Wharry S. M.: Randomness in Ziegler–Natta olefin copolymerizations as determined by ^{13}C-NMR spectroscopy – The influence of chain heterogeneity. Polymer, **45**, 2985–2989 (2005). DOI: 10.1016/j.polymer.2004.02.067

[35] Hsieh E. T., Randall J. C.: Monomer sequence distributions in ethylene-1-hexene copolymers. Macromolecules, **15**, 1402–1406 (1982). DOI: 10.1021/ma00233a036

[36] De Rosa C., Auriemma F., de Ballesteros O. R., Resconi L., Camurati L.: Crystallization behavior of isotactic propylene–ethylene and propylene–butene copolymers: Effect of comonomers versus stereodefects on crystallization properties of isotactic polypropylene. Macromolecules, **40**, 6600–6616 (2007). DOI: 10.1021/ma070409+

[37] Hosoda S., Hori H., Yada K-I., Nakahara S-Y., Tsuji M.: Degree of comonomer inclusion into lamella crystal for propylene/olefin copolymers. Polymer, **43**, 7451–7460 (2002). DOI: 10.1016/S0032-3861(02)00680-8

[38] Schwerdtfeger E. D., Miller S. A.: Intrinsic branching effects in syndiotactic copolymers of propylene and higher α-olefins. Macromolecules, **40**, 5662–5668 (2007). DOI: 10.1021/ma070060q

[39] De Rosa C., Auriemma F., de Ballesteros O. R., De Luca D., Resconi L.: The double role of comonomers on the crystallization behavior of isotactic polypropylene: Propylene–hexene copolymers. Macromolecules, **41**, 2172–2177 (2008). DOI: 10.1021/ma071753+

[40] De Rosa C., Capitani D., Cosco S.: Solid-state ^{13}C nuclear magnetic resonance spectra of four crystalline forms of isotactic poly(4-methyl-1-pentene). Macromolecules, **30**, 8322–8331 (1997). DOI: 10.1021/ma970706m

[41] Aharoni S. M., Charlet G., Delmas G.: Investigation of solutions and gels of poly(4-methyl-1-pentene) in cyclohexane and decalin by viscosimetry, calorimetry, and X-ray diffraction. A new crystalline form of poly(4-methyl-1-pentane) from gels. Macromolecules, **14**, 1390–1394 (1981). DOI: 10.1021/ma50006a048

eXPRESS Polymer Letters Vol.10, No.12 (2016) 1034–1046
Available online at www.expresspolymlett.com
DOI: 10.3144/expresspolymlett.2016.96

Enhanced protective properties and UV stability of epoxy/graphene nanocomposite coating on stainless steel

H. Alhumade[1], A. Yu[1], A. Elkamel[1], L. Simon[1], A. Abdala[2,3]*

[1]Department of Chemical Engineering, University of Waterloo, Waterloo, Ontario, Canada N2L 3G1
[2]Qatar Environmental and Energy Research Institute (QEERI), Hamad Bin Khalifa University, Qatar Foundation, Doha, Qatar
[3]College of Sciences and Engineering, Hamad Bin Khalifa University, Qatar Foundation, Doha, Qatar

Received 8 June 2016; accepted in revised form 26 July 2016

Abstract. Epoxy-Graphene (E/G) nanocomposites with different loading of graphene were prepared via in situ prepolymerization and evaluated as protective coating for Stainless Steel 304 (SS304). The prepolymer composites were spin coated on SS304 substrates and thermally cured. Transmission Electron Microscopy (TEM) and Scanning Electron Microscopy (SEM) were utilized to examine the dispersion of graphene in the epoxy matrix. Epoxy and E/G nanocomposites were characterized using X-ray diffraction (XRD) and Fourier Transform Infrared (FTIR) techniques and the thermal behavior of the prepared coatings is analyzed using Thermogravimetric analysis (TGA) and Differential scanning calorimetry (DSC). The corrosion protection properties of the prepared coatings were evaluated using Electrochemical Impedance Spectroscopy (EIS) and Cyclic Voltammetry (CV) measurements. In addition to corrosion mitigation properties, the long-term adhesion performance of the coatings was evaluated by measuring the adhesion of the coatings to the SS304 substrate after 60 days of exposure to 3.5 wt% NaCl medium. The effects of graphene loading on the impact resistance, flexibility, and UV stability of the coating are analyzed and discussed. SEM was utilized to evaluate post adhesion and UV stability results. The results indicate that very low graphene loading up to 0.5 wt % significantly enhances the corrosion protection, UV stability, and impact resistance of epoxy coatings.

Keywords: *nanocomposites, graphene, corrosion, coatings, adhesion*

1. Introduction

Damage due to corrosion is one of the most common causes of metal component failures. The lack of mitigation protocols or methods of such electrochemical reactions may result in serious losses in both economy and industry. Although, total elimination of the corrosion process is not possible, there are different techniques that are utilized in various fields such as marine equipment, pipelines and construction in order to attenuate the intensity and severity of corrosion. Anodic or cathodic protection [1], corrosion inhibitors [2] and protective coatings [3] are examples of these techniques. Nevertheless, an increasing number of research studies have been devoted to develop more robust techniques to extend the life cycle of metals in various environments. An effective example of such technique is the use of nanocomposites, hydrophobic and organic-inorganic hybrid materials as anti-corrosion coatings in various corrosive environments [4–7].

Stainless steel already has remarkable corrosion resistance and is expected to perform satisfactorily in different environments. However, stainless steel is susceptible to pitting corrosion in chloride ions rich environments such as the marine atmospheric environment. Pitting corrosion is a galvanic corrosion

---

*Corresponding author, e-mail: aaabdalla@qf.org.qa

process where localized active areas are formed as a result of localized inclusions or breakdown of the protective passive film of chromium oxide. The presence of corrosion agents such as chloride, water and oxygen initiates localized dissolution that penetrates through the metal thickness. This penetration may not be detected until severe damages has occurred and therefore pitting corrosion is considered insidious and more difficult to detect, evaluate and mitigate compared to other more uniform corrosions.

Therefore, additional means of corrosion protection are required to boost the life cycle of stainless steel substrates in chloride ions rich environment. Polymer based composites are perfect examples of protective coatings that can enhance various properties of the coated metal substrates including but not limited to corrosion resistance. A number of polymeric matrices have already been evaluated for corrosion protection purposes; however, the lack of interface adhesion foils the use of most of these polymeric matrices as anticorrosion coatings [8, 9]. Epoxy is an environmental friendly polymeric matrix that combines various remarkable properties such as exceptional thermal stability and low thermal expansion coefficient. These desirable properties in addition to the noble interface adhesion of epoxy with various metal substrates trigger the investigation of epoxy as an anticorrosion coating on SS304 substrates.

The properties of the polymer matrix can be further enhanced by the incorporation of nanofillers. Clay and carbon nanotubes are examples of nanofillers that are incorporated in epoxy matrix to enhance the remarkable properties. However, the lower density, high surface area, and the very high aspect ratio attracted much attention to graphene [10] as a candidate for enhancing the corrosion protection property of epoxy. Graphene nanosheets, graphene nanoplatelets and functionalized graphene are different forms of graphene that have been utilized as fillers in various polymeric matrices to enhance their mechanical, thermal, dielectric, gas barrier, and corrosion resistance properties [11–22]. The incorporation of graphene into the epoxy matrix is expected to prolong the pathway corrosive agents follow to reach the metal substrate. This graphene barrier effect is expected to limit the diffusion of ions and water molecules and consequently extends the life cycle of the coated substrates. To the best of our knowledge, there is no study that investigates the application of epoxy/graphene composites as anticorrosion coating for stainless steel Type 304.

In this study, E/G nanocomposites are developed and used as protective coating for stainless steel. The corrosion protection property of the E/G nanocomposite is evaluated by conducting electrochemical and weight loss measurements in 3.5 wt% Sodium Chloride aqueous solution. The study also examines the effect of graphene loading on the adhesion, impact resistance and flexibility of E/G composite coatings. Furthermore, the long-term performance of the protective coatings is also examined by conducting the adhesion test after exposing the coated substrates to the 3.5 wt % NaCl solution for 60 days. In addition, the influences of the incorporation of graphene on the thermal behavior as well as UV resistance of epoxy are evaluated.

2. Experimental

2.1. Materials

Polished SS304 sheet 99.9% purity (3254K91, McMASTER-CARR, Ohio, USA) was used as substrates., Bisphenol A diglycidyl ether (D3415, BADGE, Sigma Aldrich, Ontario, Canada) and Poly (propylene glycol) bis(2-aminopropyl ether) (406651, B230, Sigma Aldrich, Ontario, Canada) were used as received. Graphene nanosheets (GN1P0005, ACS Material, Massachusetts, USA) were synthesized by thermal exfoliation/reduction of graphite oxide, which was prepared using the modified Hummer method and it has a surface area of 400–1000 m^2/g and electrical resistivity of $\leq 0.3\ \Omega\cdot cm$, as per the supplier specifications.

2.2. Composite preparation, coating, and curing

E/G composites with graphene loading of 0.1 wt% ($E/G_{0.1}$), 0.5 wt% ($E/G_{0.5}$) and 1 wt% (E/G_1) were prepared using *in situ* polymerization approach. The prepolymer\graphene mixture was then spin coated on SS304 substrate before thermal curing. Figure 1, schematically depicts the overall composite preparation, coating and curing process.

As an example, to prepare E/G nanocomposite with 0.1 wt% graphene via situ prepolymerization, graphene (2.1 mg) was dispersed in 0.5 g curing agent (hardener) B230 by stirring and bath sonication

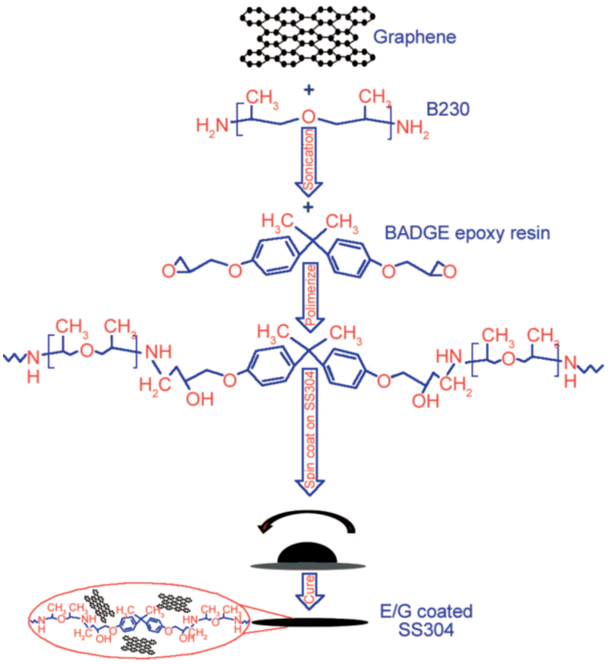

Figure 1. Schematic description of the process for the synthesis of E/G composites using *in situ* polymerization

(FS30H, Fisher Scientific, Ontario, Canada) for an hour each. BADGE (1.5 g) was added to the graphene suspension and the mixture was stirred for 1 h followed by sonication for an additional hour. The mixture was homogenized (125, Fisher Scientific, Ontario, Canada) for 30 min, sonicated for 5 min and spin coated (SC 100, Smart Coater, Missouri, USA) at 400 RPM for 1 min on a clean SS304 substrate. The composite was cured at 50 °C for 4 h to obtain 124±2 μm thick E/$G_{0.1}$ coated SS304 substrate. The same procedure was followed to prepare (E/$G_{0.5}$) and (E/G_1) using 10.1 and 20.3 mg of graphene, respectively.

2.3. Composite characterization

The dispersion of graphene in the epoxy matrix was examined using TEM (Philips CM-10 TEM, Geneva, Switzerland). Samples for the TEM study were prepared by scraping the E/G coating with a sharp knife and the collected E/G composite was dispersed in methanol for 5 min. The sample was then fished using TEM copper grid and allowed to dry under vacuum at room temperature. FTIR (Tensor 27, Bruker, Massachusetts, USA) was used to acquire spectra of epoxy and E/G composites at room temperature. XRD diffraction patterns of epoxy and E/G composites are recorded in the range of $2\theta = 3$ to 90° at 0.24°/min scan rate and 0.02° step size using MiniFlex 600 (Rigaku, Beijing, China).

2.4. Adhesion test

The interfacial adhesion between the coating and the SS304 substrate was measured according to the ASTM-D3359 standard using an adhesion tape kit (PA-2000, Paul N. Gardner Company Inc., Florida, USA) with standard blade (11-teeth with teeth spacing of 1 mm). The Interface adhesion was evaluated before and after exposing the coating to the 3.5 wt% NaCl solution for 60 days in order to examine the long-term durability of the coatings. Post-adhesion tests results were captured using SEM (Zeiss LEO 1550, New York, USA). SEM samples were placed on carbon tape attached to the SEM holder and the sample was further coated with gold via sputtering for 120 s.

2.5. Gravimetric analysis

The weight loss measurements were conducted in 500 mL glass beaker placed in a temperature controlled water bath. Coated and uncoated SS304 substrates were weighted, placed in Teflon holders with 1 cm^2 exposed surface area and immersed in a 3.5 wt% NaCl solution for 60 days at 25 °C. At the end of the exposure period, the samples were removed and washed with double distilled water before a fine brush was used to strip off the corrosion products. The samples were cleaned again by bath sonication in a double distilled water for 10 min to ensure the removal of corrosion residues, dried and weighted. All mass loss measurements were carried out in triplicate and the mean weight and the standard deviation are reported.

2.6. Electrochemical measurements

Electrochemical measurements were conducted at 25 °C in a double-jacketed 1 L corrosion cell covered with a drilled Teflon plate to allow electrodes immersion. A three electrode configuration was used to conduct the measurements, where a Silver/Silver Chloride (Ag/AgCl) electrode was used as the reference electrode (RE), two graphite rods as the auxiliary electrodes (AE) and a 1 cm^2 coated/uncoated SS304 substrate as the working electrode (WE). The WE was washed with acetone and double distilled water, dried and then installed in the sample holder before conducting the tests. 1 L temperature controlled 3.5 wt% NaCl solution was used as the electrolyte. EC-Lab software (Bio-Logic) and VSP-300 workstation (Uniscan instruments Ltd., Claix, France) were used to conduct all electrochemical measurements, where each measurement was repeated three times in order to confirm the reproducibility of the collected raw data.

The potential of the WE was allowed to stabilize for 30 min before conducting the EIS followed by the potentiodynamic measurements. The EIS measurements were conducted at frequency range from 200 kHz to 100 mHz to generate Bode and Nyquist plots. Furthermore, an equivalent circuit was used to fit the raw impedance data and EC-Lab software was used to evaluate the different components of the equivalent circuits. The potentiodynamic measurements were conducted by scanning the potential of the WE from –500 to 500 mV at a rate of 20 mV/min to produce the Tafel plots. These plots were used to extract the corrosion current (I_{corr}) using EC-Lab software by extrapolating the linear portion of the anodic and the cathodic curves.

2.7. Thermal behavior and UV degradation

The thermal stability of the nanocomposite coatings was evaluated using thermal gravimetric analysis (TGA) (TA instruments, Q500, Ontario, Canada) in the temperature range 25–800 °C, while the glass transition temperature was observed using differential scanning calorimetry (DSC) (TA instruments, Q2000, Ontario, Canada) in the temperature range 25–200 °C at 10 °C/min heating rate.

The Resistance of the prepared Epoxy and E/G coatings to UV degradation was assessed using an accelerated weathering tester (QUV, Q-LAB, Florida, USA) according to ASTM-D4587 standard. Testing specimens were continuously exposed to repeated UV cycle at 60±2.5 °C for 8 hours, followed by a condensation cycle at 50±2.5 °C for 4 hours over 30 days followed by SEM examination of the surface morphology of the epoxy and E/G coatings.

2.8. Flexibility and impact resistance

Two different types of tests were carried out to illustrate the influences of graphene loading on the room temperature flexibility and impact resistance of the coatings. In the bending test, the coated substrate was bent over a conical shaped mandrel (MN-301003, Paul N. Gardner Company Inc., Florida, USA) with a diameter ranges from 3.1 to 38 mm to assess the flexibility of the coatings. The test was repeated three times and the mean diameter at which the coatings cracked were reported.

Impact resistance was performed to evaluate the resistance of the prepared coatings to rapid deformation by a falling weight. The test was conducted using a universal impact tester (IM-172RF, Paul N. Gardner Company Inc., Florida, USA) with combined 0.5 inch ball and 2 lb weight indenter according to ASTM D2794 standard. The combined weight and indenter were raised 1 inch in the testing tube and released to drop on the coated substrate and the falling weight test was repeated with 1 inch increments in height until a crack in the coating was observed. The height at which the coating cracks was recorded and the test was repeated slightly above, slightly below and at the recorded height five times each according to the ASTM standard. The elevation at which the coating cracks in all five trials is reported as the impact resistance limit of the coating to rapid deformation.

3. Results and discussion

3.1. Characterization of the E/G composites

The dispersion of graphene in the polymeric matrix for $E/G_{0.1}$ and $E/G_{0.5}$ composites was examined using SEM and TEM as shown in Figure 2. The TEM images, clearly illustrate the influence of graphene loading on the degree of dispersion, where graphene is well dispersed as indicated by thin sheets in the $E/G_{0.1}$ coating, while thick stack of graphene sheets were observed in $E/G_{0.5}$ coating. SEM images, depicts wide degrees of dispersion in both $E/G_{0.1}$ and $E/G_{0.5}$ composites.

FTIR was utilized to characterize both epoxy and E/G composites as depicted in Figure 3. Different characteristic peaks are identified, such as the peaks at 1508 and 1609 cm^{-1} (C–C skeletal stretching), 915 cm^{-1} (epoxide ring) and 3380 cm^{-1} (–OH stretching), which confirms the curing of the epoxy resin. Comparing the epoxy spectrum to the E/G composite spectra revealed that there were no clear dissimilar absorption peaks indicating no chemical linkages between graphene and the epoxy function groups. Epoxy and E/G composites were also characterized

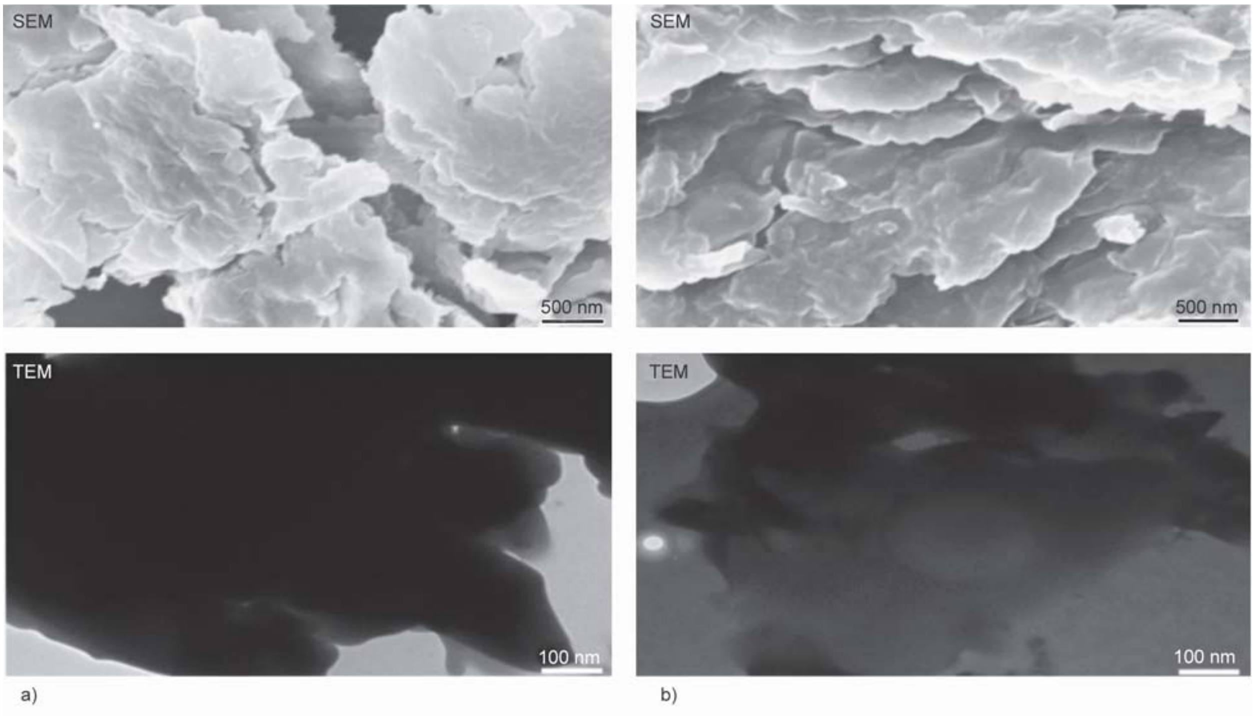

Figure 2. SEM and TEM images for graphene dispersion in (a) $E/G_{0.5}$ and (b) $E/G_{0.1}$

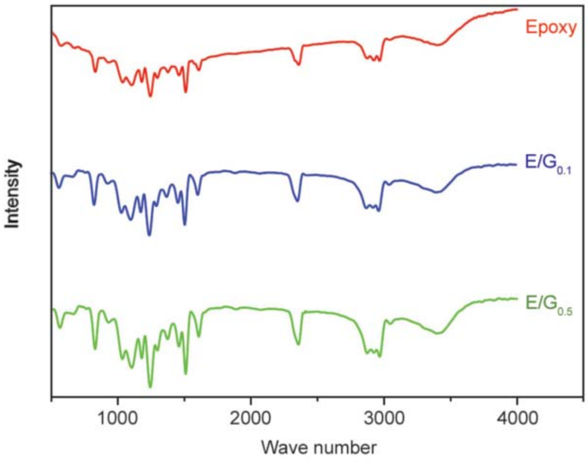

Figure 3. FTIR spectra of neat epoxy and E/G composites

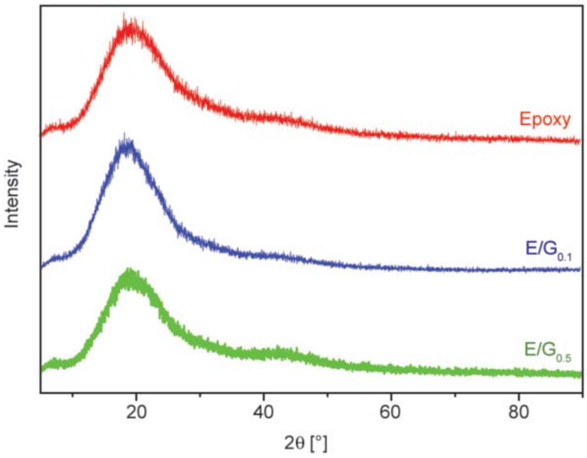

Figure 4. XRD patterns of neat epoxy and E/G composites

using XRD and the diffraction spectrum are depicted in Figure 4. All XRD patterns show broadly amorphous peak appearing around 2θ value between 10 and 30°, which ascribed to the homogeneously amorphous of epoxy. Moreover, the observed XRD patterns indicate that the degree of crystallinity of epoxy is retained after incorporation of graphene.

3.2. Adhesion test

Interface adhesion between the metal substrate and the coating is a significant property that needs to be examined before the coating can be considered protective. Poor interface adhesion may result in the formation of voids between the metal substrate and the coating, where corrosive agents may accumulate and accelerate the corrosion process. Therefore, decent interface adhesion is always desired. The adhesion of E/G coatings to the SS304 substrates were examined and evaluated according to ASTM D3359 adhesion tape standard test. The test was performed on $E/G_{0.1}$ and $E/G_{0.5}$ coatings before and after 60 days of exposure to the 3.5 wt% NaCl solution. The post adhesion test results are presented in Figure 5, where no peelings were observed in any of the coatings and all coatings received 5B rating (0% peeling) according to the ASTM standard.

Moreover, it was interesting to observe the shortcoming of increasing the load of graphene beyond

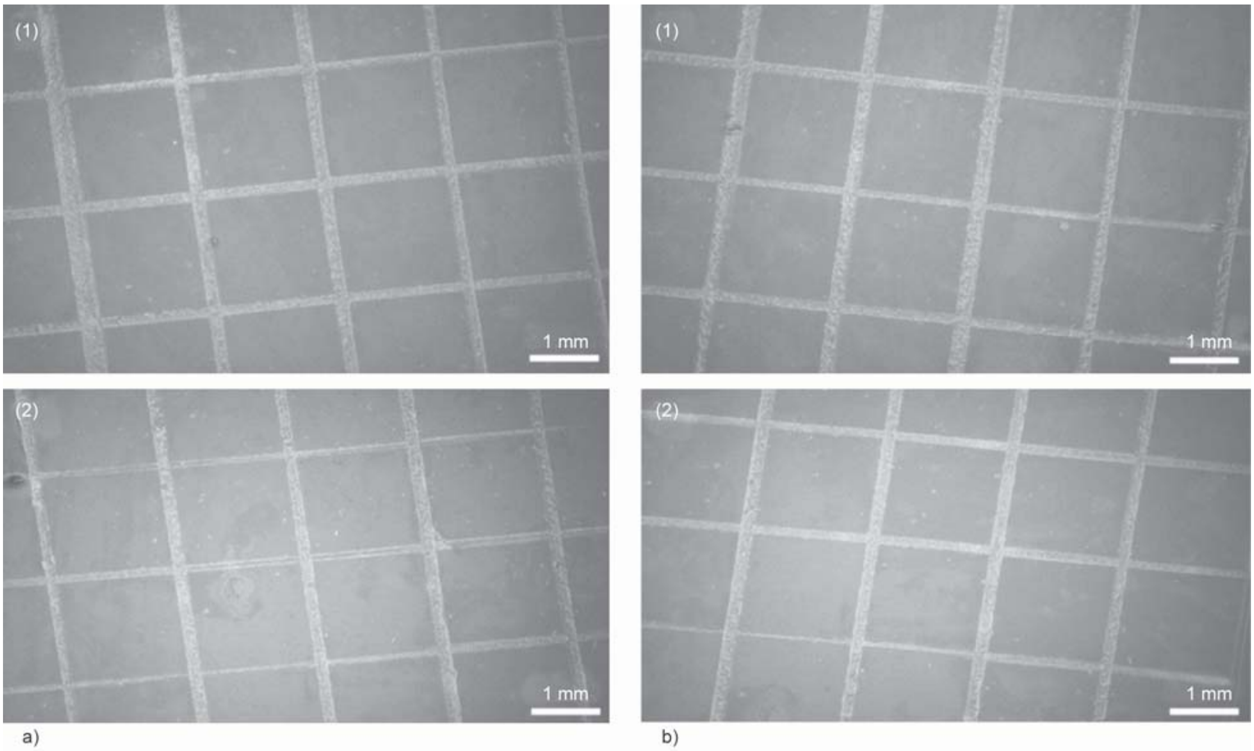

Figure 5. SEM images of post-adhesion tests of (1) E/$G_{0.1}$ and (2) E/$G_{0.5}$ coated SS304 substrates (a) before and (b) after 60 days of exposure to the corrosive medium

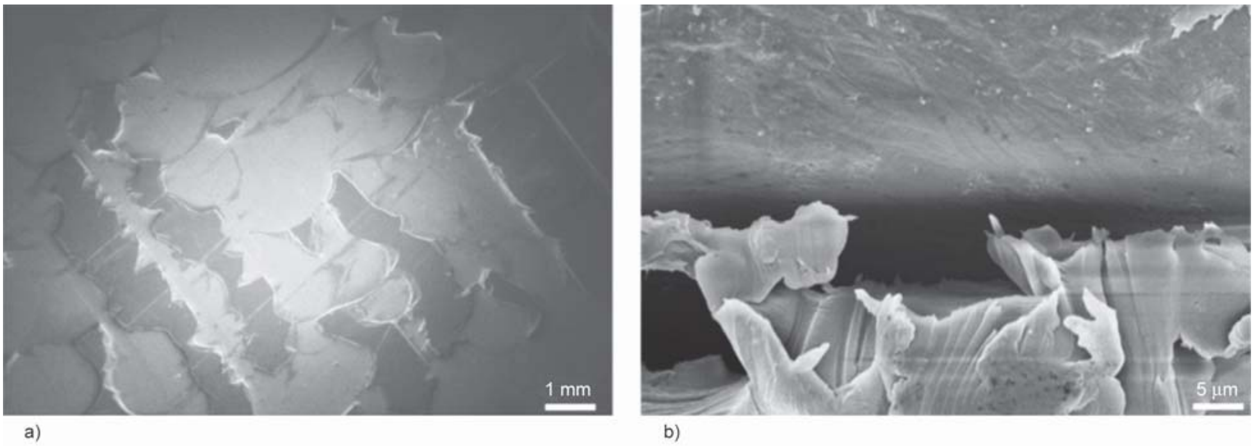

Figure 6. SEM image of (a) post-adhesion test and (b) cross section view of E/G_1 coated SS304 substrate

the percolation loading. The disadvantage of increasing the graphene loading is clearly depicted in Figure 6a, where poor interface adhesion between the E/G_1 coating and SS304 substrate was observed and the coating receives 0B rate (more than 65% peeling) according to the ASTM standard. The observed undesirable influence of the load of graphene on the interface adhesion can be attributed to accumulation of graphene at the interface, which attenuates the contact area between epoxy resin and SS304 substrate as depicted in Figure 6b, where clear gaps can be observed between E/G_1 and the SS304 substrate.

3.3. Weight loss

Weight loss measurements for coated/uncoated SS304 substrate were reported after 60 days of immersion in the 3.5 wt% NaCl solution at 25 °C. These measurements were used to calculate the corrosion rate (R_corr) and the protection efficiency (P_EF) of the different coatings using Equtions (1) and (2):

$$R_\text{corr} = \frac{W_0 - W}{A \cdot t} \tag{1}$$

$$P_\text{EF}[\%] = \left(1 - \frac{R_\text{corr}}{R^\circ_\text{corr}}\right) \cdot 100 \tag{2}$$

Table 1. Weight loss measurements for bare SS304, epoxy, $E/G_{0.1}$ and $E/G_{0.5}$ coated SS304 in a 3.5 wt% NaCl solution

Sample	W_0 [mg]	W [mg]	R_{corr} [mg·cm^{-2}·d^{-1}]	$R_{corr, STD}$ [mg·cm^{-2}·d^{-1}]	P_{EF} [%]
SS304	93.1	66.9	0.440	0.009	–
Epoxy	107.0	101.6	0.090	0.011	79.5
$E/G_{0.1}$	115.9	113.5	0.040	0.008	90.9
$E/G_{0.5}$	122.9	122.0	0.015	0.005	96.6

where A is the exposed surface area (1 cm^2), W_0 and W are the weight [mg] before and after exposure, respectively, t is the immersion time (60 days), R_{corr} and R°_{corr} are the corrosion rate of coated and bare SS304 substrates, respectively. Furthermore, standard deviation of R_{corr} ($R_{corr,\,STD}$) was computed and reported in Table 1 using triplicate weight loss measurements for each sample.

The data reported in Table 1 illustrate that coating SS304 with epoxy may prolong the life cycle of the metal substrate as indicated by the decrease in the corrosion rate. Furthermore, the results demonstrate that the corrosion rate is attenuated and the protection efficiency of epoxy is enhanced by the incorporation of graphene. Moreover, the low values of Rcorr, STD demonstrate the excellent reproducibility of the results.

3.4. Electrochemical impedance measurements

EIS is a widely used technique to investigate electrochemical activity on metal substrates. Here, EIS is utilized to examine the corrosion behavior of bare and coated SS304 substrates. In EIS, an alternating current (AC) is forced through a circuit that may contain insulators, resistors and capacitors or combinations of items resulting in a complex output resistance known as impedance. In corrosion studies, the AC is fed to the system over a range of frequency and the complex output at different frequencies are reported as the impedance of the WE. Furthermore, impedance can be modelled using an equivalent circuit that contain a specific combination of different elements such as resistors and capacitors.

The impedance behavior of bare and coated SS304 substrates is measured in temperature controlled 3.5 wt% NaCl electrolyte using the EC-Lab software after allowing the potential of the WE to stabilize for 30 min. The EC-Lab software was also used to model and fit the raw impedance data using equivalent circuits with specific combinations as shown in Figure 7. In the equivalent circuits, R_s and R_{ch} represent electrolyte and charge transfer resistances, respectively, while C is a double layer capacitor. The magnitudes of the various elements in the equivalent circuit and the frequency of the AC signal (ω) were utilized to fit raw impedance data using Equation (3):

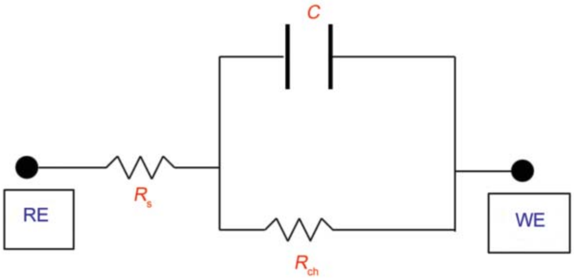

Figure 7. Equivalent circuits used to model the electrochemical impedance data

$$Z = Z' + jZ'' =$$
$$= R_s \frac{R_{ch}}{1+(R_{ch}\cdot C\cdot\omega)^2} + j\frac{R_{ch}^2\cdot C\cdot\omega}{1+(R_{ch}\cdot C\cdot\omega)^2} \qquad (3)$$

Figure 8, depicts Nyquist plots for bare and coated SS304 substrate, where real and imaginary parts of the impedance are presented. The Nyquist plot clearly represents the corrosion protection by the epoxy coating as demonstrated by the increase in the size of the impedance semi-circleindicating annenhancementt in corrosion mitigation and slower corrosion rate for the epoxy coated sample compared to the bare SS304. Nevertheless, this corrosion protection enhancement is further improved by incorporating graphene in the epoxy matrix, where the real resistivity value at the high frequency end has increased

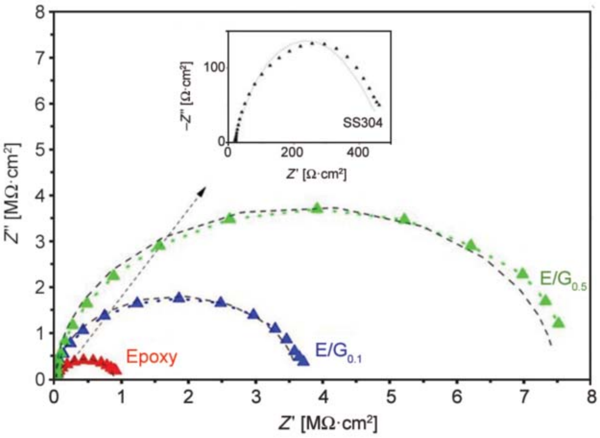

Figure 8. Nyquist plots for bare SS304 (inset), epoxy, $E/G_{0.1}$ and $E/G_{0.5}$ coated SS304 substrates

from $1.0\cdot10^6$ Ω·cm^2 for the epoxy coated sample to $3.8\cdot10^6$ Ω·cm^2 for E/G$_{0.1}$ coated sample and $7.8\cdot10^6$ Ω·cm^2 for E/G$_{0.5}$ coated sample.

In addition to the qualitative analysis, the computed values of the different elements of the equivalent circuits shown in Figure 7 can be used to evaluate the corrosion protection properties of the different coatings. It should be noted that the unique combinations of elements in the presented circuits resulted in the best fitting of raw impedance data. Table 2, represents the values of the various elements in the equivalent circuits and the repeatability of triplicate measurements is illustrated by the small values of $R_{\text{ch, STD}}$. The results clearly illustrate the ability of the epoxy coating to protect the SS304 substrate from corrosion as indicated by the increase in the charge transfer resistance. Moreover, the results illustrate the advantages of incorporating graphene as implied by the significant increase in the charge transfer resistance for E/G$_{0.1}$ and E/G$_{0.5}$.

Table 2. Electrochemical corrosion parameters obtained from equivalent circuit for EIS raw measurements for bare SS304, epoxy, E/G$_{0.1}$ and E/G$_{0.5}$ coated SS304 in 3.5 wt% NaCl solution

Sample	R_S [Ω·cm^2]	C [F]	R_{ch} [Ω·cm^2]	$R_{\text{ch, STD}}$ [Ω·cm^2]
SS304	18.5	$8.5\cdot10^{-6}$	450.5	10
Epoxy	18.0	$1.4\cdot10^{-10}$	$8.7\cdot10^5$	190
E/G$_{0.1}$	18.2	$3.9\cdot10^{-11}$	$3.63\cdot10^6$	380
E/G$_{0.5}$	18.1	$3.9\cdot10^{-11}$	$7.55\cdot10^6$	260

Bode plots are another representation of the corrosion protection ability of the coating. Figure 9a, depicts the Bode plots, where the real part of impedance (Z_{real}) is plotted versus frequency, while Figure 9b depicts the phase plots. Corrosion resistance can also be represented by the Z_{real} values at the lowest recorded frequencies. From Figure 9a, logZ_{real} at the lowest frequencies for bare, epoxy, E/G$_{0.1}$ and E/G$_{0.5}$ coated SS304 are 2.7, 6.0, 6.6 and 6.9 Ω·cm^2, respectively.

EIS results illustrate that epoxy coatings may mitigate the corrosion process on SS304 substrate and prolong the life cycle of the metal. However, the incorporation of graphene would further enhance such a protection characteristic of the epoxy and the degree of enhancement depends on graphene loading. This variation in protection efficiencies can be attributed to the noble barrier property of graphene [16], which attenuate the corrosion rate by prolonging the tortuosity pathway for the corrosive agents to reach the SS304 substrate.

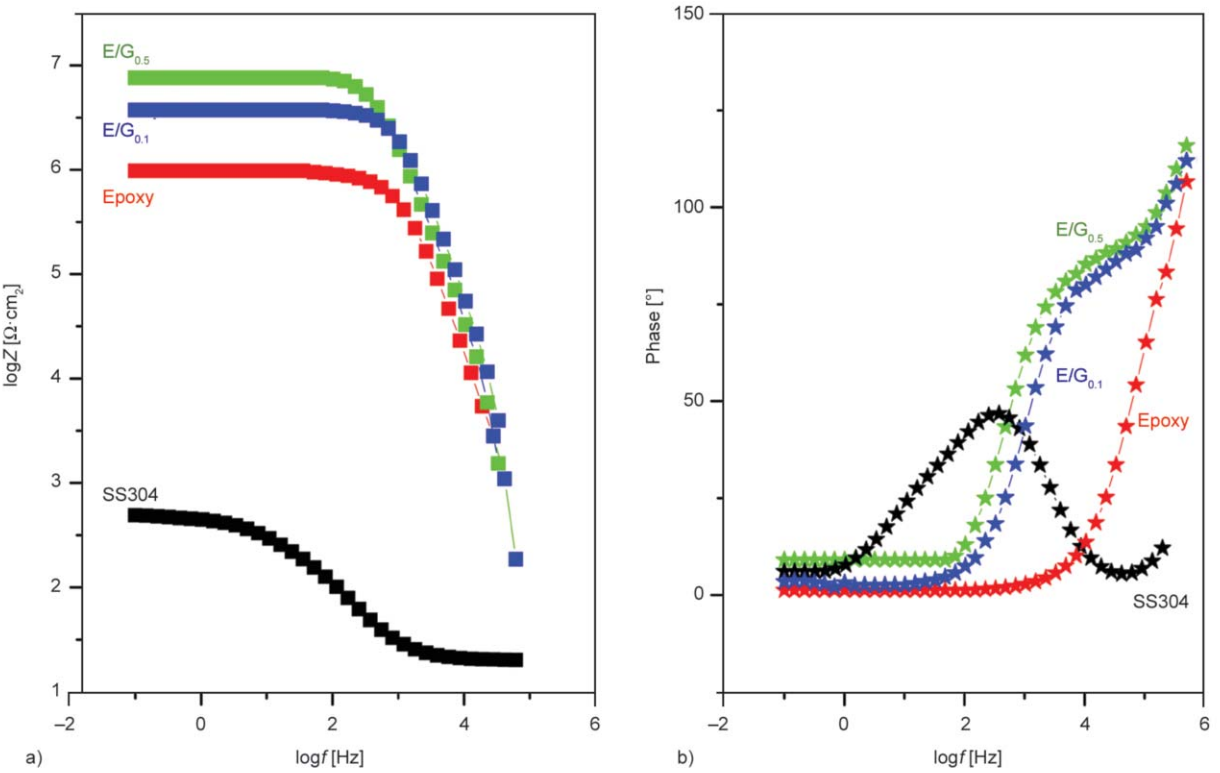

Figure 9. (a) Bode and (b) phase plots for bare SS304, epoxy, E/G$_{0.1}$ and E/G$_{0.5}$ coated SS304 substrates

3.5. Potentiodynamic measurements

Cyclic Voltammetry is a widely utilized technique to characterize electrochemical behavior of metal substrates and coatings. In this study, a three-electrode configuration was used to conduct cyclic voltammetry tests on bare and coated SS304 substrates. The raw data were recorded using the EC-Lab software and all measurements were obtained in 3.5 wt% NaCl solution at 25 °C. Furthermore, the potential of the testing sample was allowed to stabilize for 30 min before conducting any experiment. Even though the potential of the working electrode was scanned from –500 to 500 mV, only the areas where the electrode shifted from the anodic to cathodic behavior, which is known as the Tafel plots, were presented as shown in Figure 10. Important parameters such as E_{corr} and I_{corr} were extracted from the Tafel plots. Furthermore, the extracted E_{corr} and I_{corr} from triplicates measurement for each sample were utilized to demonstrate the reproducibility of the results by analysis of the standard deviation of E_{corr} ($E_{\mathrm{corr,\,STD}}$) and I_{corr} ($I_{\mathrm{corr,\,STD}}$), which are reported in Table 3.

These extracted parameters can be used to compute the polarization resistances (R_{p}) of the protective coatings using Equation (4), which is known as the Stern-Geary equation:

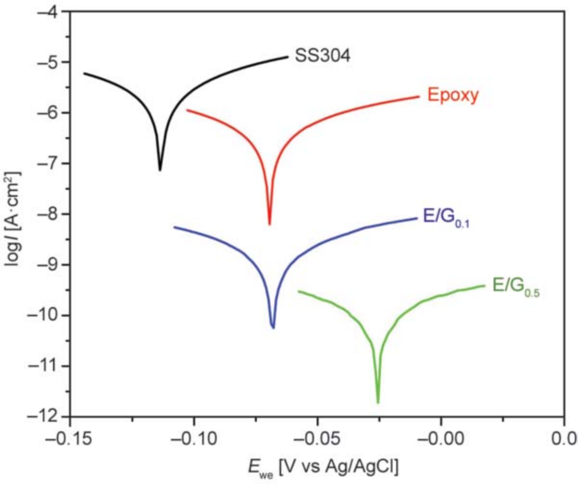

Figure 10. Tafel plots for bare SS304, epoxy, E/G$_{0.1}$ and E/G$_{0.5}$ coated SS304 substrates

$$R_{\mathrm{p}} = \frac{b_{\mathrm{a}} \cdot b_{\mathrm{c}}}{2.303(b_{\mathrm{a}} + b_{\mathrm{c}})} \cdot I_{\mathrm{corr}} \tag{4}$$

where $b_{\mathrm{a}}/b_{\mathrm{c}}$ are the anodic/cathodic Tafel slops (dE/dlog$I$), respectively, and extrapolating the linear portion of these curves determines I_{corr} at the intersection. Finally, I_{corr} values can be used to evaluate the protection efficiencies of the different coatings using Equation (5):

$$P_{\mathrm{EF}}[\%] = \left(1 - \frac{I_{\mathrm{corr}}}{I^{\circ}_{\mathrm{corr}}}\right) \cdot 100 \tag{5}$$

where $I^{\circ}_{\mathrm{corr}}$ and I_{corr} are corrosion currents of bare and coated SS304, respectively. The variations in corrosion and computed parameters (E_{corr}, I_{corr}, R_{p}), which are reported in Table 3 may explain the influences of the various protective coatings on the electrochemical behavior of the SS304 substrate. In general, a positive shift in E_{corr}, R_{p} and P_{EF} plus a drop in I_{corr}, represents an enhancement in corrosion mitigation.

The abilities of E/G coatings in mitigating corrosion on SS304 substrates were confirmed by the results presented in Figure 10 and Table 3. These results demonstrate that the corrosion protection performance of epoxy coatings can be significantly enhanced by the incorporation of graphene as illustrated by the positive shifts in the E_{corr}, R_{p} and P_{EF} and the attenuation of the I_{corr}. Furthermore, it was interesting to observe that the level of enhancement in P_{EF} of E/G can be positively influenced by increasing the graphene loading as illustrated in Figure 10 and Table 3, which is in agreement with the results obtained from the gravimetric method. This enhancement in corrosion mitigation properties of E/G coatings can again be attributed to the barrier property of graphene, which prolong the pathway that corrosive agents follow to reach the metal substrate.

3.6. Thermal behavior and UV degradation

The incorporation of graphene in polymeric matrix has influenced the thermal stability of the resin. This

Table 3. Electrochemical corrosion parameters obtained from cyclic voltammetry measurements for bare SS304, epoxy, E/G$_{0.1}$ and E/G$_{0.5}$ coated SS304 in a 3.5 wt% NaCl solution

Sample	E_{corr} [mV vs Ag/AgCl]	$E_{\mathrm{corr,\,STD}}$ [V vs Ag/AgCl]	I_{corr} [µA/cm²]	$I_{\mathrm{corr,\,STD}}$ [µA/cm²]	b_{a}	b_{c}	R_{P} [Ω·cm²]	P_{EF} [%]
SS304	–113.5	0.009	2.40	0.002	48.2	55.3	4.6	–
Epoxy	–69.4	0.060	0.46	0.010	87.0	88.2	41.3	80.8
E/G$_{0.1}$	–65.0	0.010	0.06	0.009	82.3	74.0	282.0	97.5
E/G$_{0.5}$	–27.7	0.007	$8.7\cdot10^{-3}$	0.005	61.4	54.5	1441.0	99.6

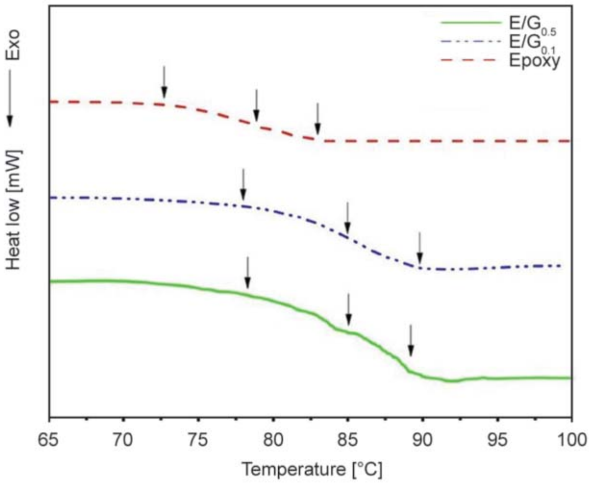

Figure 11. DSC thermograms of epoxy and E/G coatings. The three arrow on each curve represent, from left to right, the onset, mid, and end point of the T_g transition.

can be observed as an upward shift in the glass transition temperature (T_g) as depicted in Figure 11. The increase in T_g has been reported for other graphene polymer nanocomposites and is attributed to the strong interface between the filler and polymer matrix, which restricts the polymer chains' mobility [23]. Moreover, incorporation of graphene increases the thermal stability of the epoxy composite as observed by the increase in onset degradation temperature (T_{onset}), which is the temperature where 5% weight loss is observed as depicted in Figure 12, inset has increased from 352.8 °C for the neat epoxy to 358.5 and 358.8°C for E/$G_{0.1}$ and E/$G_{0.5}$, respectively, confirming the strong interactions between graphene and epoxy polymer possibility through the amine groups on the polymer chains and the epoxy/hydroxyl groups on the reduced graphene surface.

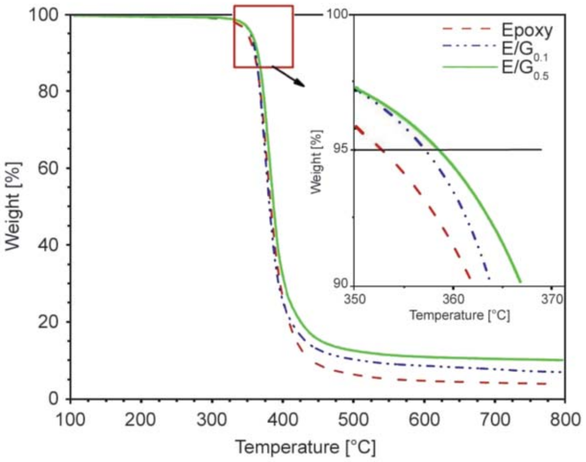

Figure 12. TGA thermograms of epoxy and E/G composites

Epoxy polymers are known to degrade when exposed to UV radiation [24]. Therefore, the surface morphology of the prepared coatings were observed after 30 days of exposure to UV and condensation cycles using SEM and results are depicted in Figure 13. Sever damages can be observed on the epoxy surface, where the damages were manifested in forms of micro-cracks and pits as illustrated in Figure 13a. Surface cracking was also observed on E/$G_{0.1}$ coating as depicted in Figure 13b; however, no evidence of pitting was observed. The capacity of graphene in enhancing the durability of the epoxy coating is well illustrated in Figure 13c, where increasing the load of graphene to 0.5%, E/$G_{0.5}$, leads to prevention of pitting as well as significant reduction in the number of observed micro-cracks due to the enhanced UV stability induced by graphene [25].

3.7. Flexibility and impact resistance

Mechanical properties such as elasticity and impact resistance in addition to adhesion and corrosion mitigation are important characteristics of polymer coatings. The bending and the impact resistance tests were conducted on epoxy and E/G composites coatings in order to evaluate the impact of graphene on the flexibility and impact resistance. Figure 14 shows the bending and impact resistance results for different coatings, where the main bending diameters and the elevations at which the coating fails for five times are reported. These results illustrate that incorporation of graphene reduces the flexibility of the epoxy coating and the degree of reduction increases with graphene loading, which is attributed to the increase in stiffness. In contrast, the addition of graphene enhances the impact resistance of epoxy and here too, the degree of enhancement is proportional to the graphene loading. The observed effects of graphene on the bending and the impact resistance are attributed to the increase in stiffness and toughness of the epoxy composite with graphene loading, which was also reported [26–29], which enhances the resistance to sudden deformation and reduces the elasticity of the epoxy coating.

4. Conclusions

Epoxy/graphene composites were prepared using situ prepolymerization approach, spin coated and thermally cured on SS304 substrates. We demonstrated

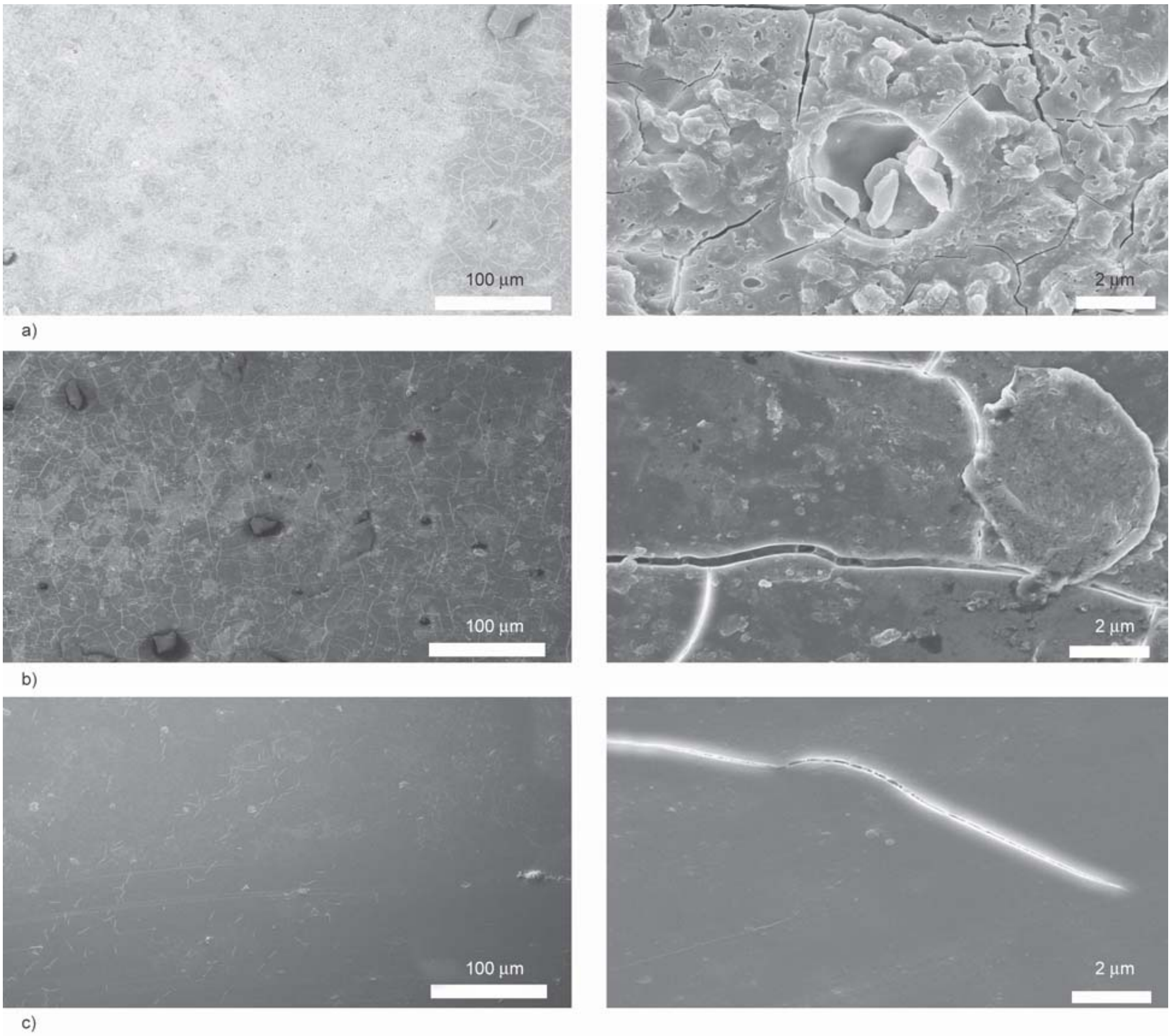

Figure 13. SEM images of post-UV degradation tests of (a) epoxy (b) E/$G_{0.1}$ and (c) E/$G_{0.5}$ coated SS304 substrates after 30 days of exposure to UV and condensation cycles

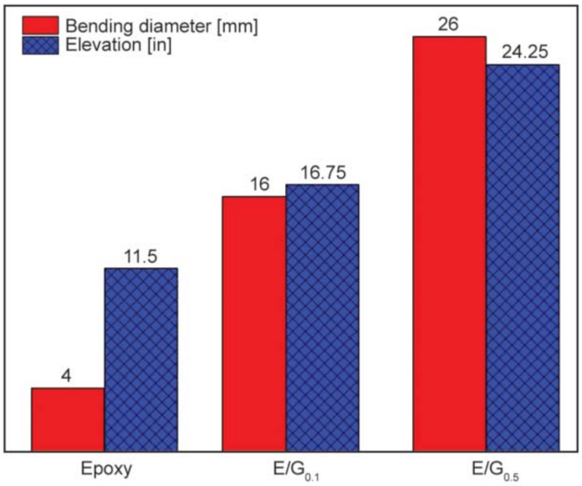

Figure 14. Bending and impact resistance test results for epoxy, E/$G_{0.1}$ and E/$G_{0.5}$ coatings on SS304.

that the corrosion protection ability of the epoxy is significantly enhanced by incorporation of graphene due to the barrier property of graphene, which shields the corrosive agents from reaching the SS304 substrate. Morover, incorporation of graphene enhances the mechanical properties and impact the thermal properties as well as the adhesion of the epoxy composite to the SS304 substrate. Graphene loading and the degree of dispersion have significant impact on the thermal, and mechanical properties as well as adhesion to the SS304 substrate, the corrosion protection characteristics and UV stability. Indeed, it is interesting to observe that increasing graphene loading in the epoxy matrix beyond an optimum loading of 0.5 wt% may attenuate the interface adhesion between coating and the SS304 substrate due to aggregation of graphene and reduction of the interface area.

Acknowledgements

The authors would like to acknowledge the financial support of the Petroleum Institute, Abu Dhabi through research project # 66. The authors also acknowledge the financial support and Mr. Alhumade full scholarship from the Ministry of Education, Saudi Arabia.

References

[1] Shen G. X., Chen Y. C., Lin C. J.: Corrosion protection of 316 L stainless steel by a TiO_2 nanoparticle coating prepared by sol–gel method. Thin Solid Films, **489**, 130–136 (2005).
DOI: 10.1016/j.tsf.2005.05.016

[2] Zheludkevich M. L., Serra R., Montemor M. F., Miranda Salvado I. M., Ferreira M. G. S.: Corrosion protective properties of nanostructured sol–gel hybrid coatings to AA2024-T3. Surface and Coatings Technology, **200**, 3084–3094 (2006).
DOI: 10.1016/j.surfcoat.2004.09.007

[3] Moretti G., Guidi F., Grion G.: Tryptamine as a green iron corrosion inhibitor in 0.5 M deaerated sulphuric acid. Corrosion Science, **46**, 387–403 (2004).
DOI: 10.1016/S0010-938X(03)00150-1

[4] Gray J., Luan B.: Protective coatings on magnesium and its alloys – A critical review. Journal of Alloys and Compounds, **336**, 88–113 (2002).
DOI: 10.1016/S0925-8388(01)01899-0

[5] Stratmann M., Feser R., Leng A.: Corrosion protection by organic films. Electrochimica Acta, **39**, 1207–1214 (1994).
DOI: 10.1016/0013-4686(94)E0038-2

[6] Mittal V. K., Bera S., Saravanan T., Sumathi S., Krishnan R., Rangarajan S., Velmurugan S., Narasimhan S.: Formation and characterization of bi-layer oxide coating on carbon-steel for improving corrosion resistance. Thin Solid Films, **517**, 1672–1676 (2009).
DOI: 10.1016/j.tsf.2008.09.094

[7] Guo S. F., Zhang H. J., Liu Z., Chen W., Xie S. F.: Corrosion resistances of amorphous and crystalline Zr-based alloys in simulated seawater. Electrochemistry Communications, **24**, 39–42 (2012).
DOI: 10.1016/j.elecom.2012.08.006

[8] Bellucci F., Nicodemo L., Monetta T., Kloppers M. J., Latanision M. R.: A study of corrosion initiation on polyimide coatings. Corrosion Science, **33**, 1203–1226 (1992).
DOI: 10.1016/0010-938X(92)90131-L

[9] Roy D., Simon G. P., Forsyth M., Mardel J.: Towards a better understanding of the cathodic disbondment performance of polyethylene coatings on steel. Advances in Polymer Technology, **21**, 44–58 (2002).
DOI: 10.1002/adv.10010

[10] Xu Z., Buehler M. J.: Geometry controls conformation of graphene sheets: Membranes, ribbons, and scrolls. ACS Nano, **4**, 3869–3876 (2010).
DOI: 10.1021/nn100575k

[11] Bao C., Song L., Wilkie C., Yuan B., Guo Y., Hu Y., Gong X.: Graphite oxide, graphene, and metal-loaded graphene for fire safety applications of polystyrene. Journal of Materials Chemistry, **22**, 16399–16406 (2012).
DOI: 10.1039/C2JM32500D

[12] Potts J., Shankar O., Du L., Ruoff R.: Processing–morphology–property relationships and composite theory analysis of reduced graphene oxide/natural rubber nanocomposites. Macromolecules, **45**, 6045–6055 (2012).
DOI: 10.1021/ma300706k

[13] Li M., Huang X., Wu C., Xu H., Jiang P., Tanaka T.: Fabrication of two-dimensional hybrid sheets by decorating insulating PANI on reduced graphene oxide for polymer nanocomposites with low dielectric loss and high dielectric constant. Journal of Materials Chemistry, **22**, 23477–23484 (2012).
DOI: 10.1039/C2JM34683D

[14] Longun J., Iroh J.: Nano-graphene/polyimide composites with extremely high rubbery plateau modulus. Carbon, **50**, 1823–1832 (2012).
DOI: 10.1016/j.carbon.2011.12.032

[15] Liao K-H., Park Y. T., Abdala A., Macosko C.: Aqueous reduced graphene/thermoplastic polyurethane nanocomposites. Polymer, **54**, 4555–4559 (2013).
DOI: 10.1016/j.polymer.2013.06.032

[16] Chang K. C., Hsu C. H., Lu H. I., Ji W. F., Chang C. H., Li W. Y., Chuang T. L., Yeh J. M., Liu W. R., Tsai M. H.: Advanced anticorrosive coatings prepared from electroactive polyimide/graphene nanocomposites with synergistic effects of redox catalytic capability and gas barrier properties. Express Polymer Letters, **8**, 243–255 (2014).
DOI: 10.3144/expresspolymlett.2014.28

[17] Alhumade H., Abdala A., Yu A., Elkamel A., Simon L.: Corrosion inhibition of copper in sodium chloride solution using polyetherimide/graphene composites. Canadian Journal of Chemical Engineering, **94**, 896–904 (2016).
DOI: 10.1002/cjce.22439

[18] Liu S., Gu L., Zhao H., Chen J., Yu H.: Corrosion resistance of graphene-reinforced waterborne epoxy coatings. Journal of Materials Science and Technology, **32**, 425–431 (2016).
DOI: 10.1016/j.jmst.2015.12.017

[19] Chang C-H., Huang T-C., Peng C-W., Yeh T-C., Lu H-I., Hung W-I., Weng C-J., Yang T-I., Yeh J-M.: Novel anticorrosion coatings prepared from polyaniline/graphene composites. Carbon, **50**, 5044–5051 (2012).
DOI: 10.1016/j.carbon.2012.06.043

[20] Chen Y., Zhang H-B., Huang Y., Jiang Y., Zheng W-G., Yu Z-Z.: Magnetic and electrically conductive epoxy/graphene/carbonyl iron nanocomposites for efficient electromagnetic interference shielding. Composites Science and Technology, **118**, 178–185 (2015). DOI: 10.1016/j.compscitech.2015.08.023

[21] Wan Y-J., Yang W-H., Yu S-H., Sun R., Wong C-P., Liao W-H.: Covalent polymer functionalization of graphene for improved dielectric properties and thermal stability of epoxy composites. Composites Science and Technology, **122**, 27–35 (2016). DOI: 10.1016/j.compscitech.2015.11.005

[22] Wang F., Drzal L., Qin Y., Huang Z.: Enhancement of fracture toughness, mechanical and thermal properties of rubber/epoxy composites by incorporation of graphene nanoplatelets. Composites Part A: Applied Science and Manufacturing, **87**, 10–22 (2016). DOI: 10.1016/j.compositesa.2016.04.009

[23] Liao K-H., Aoyama S., Abdala A., Macosko C.: Does graphene change T_g of nanocomposites? Macromolecules, **47**, 8311–8319 (2014). DOI: 10.1021/ma501799z

[24] Tang L-C., Wan Y-J., Yan D., Pei Y-B., Zhao L., Li Y-B., Wu L-B., Jiang J-X, Lai G-Q.: The effect of graphene dispersion on the mechanical properties of graphene/epoxy composites. Carbon, **60**, 16–27 (2013). DOI: 10.1016/j.carbon.2013.03.050

[25] Ghasemi-Kahrizsangi A., Neshati J., Shariatpanahi H., Akbarinezhad E.: Improving the UV degradation resistance of epoxy coatings using modified carbon black nanoparticles. Progress in Organic Coatings, **85**, 199–207 (2015). DOI: 10.1016/j.porgcoat.2015.04.011

[26] Wan Y-J., Yang W-H., Yu S-H., Sun R., Wong C-P., Liao W-H.: Covalent polymer functionalization of graphene for improved dielectric properties and thermal stability of epoxy composites. Composites Science and Technology, **122**, 27–35 (2016). DOI: 10.1016/j.compscitech.2015.11.005

[27] Rafiee M., Rafiee J., Wang Z., Song H., Yu Z-Z., Koratkar N.: Enhanced mechanical properties of nanocomposites at low graphene content. ACS Nano, **3**, 3884–3890 (2009). DOI: 10.1021/nn9010472

[28] Chandrasekaran S., Sato N., Tölle F., Mülhaupt R., Fiedler B., Schulte K.: Fracture toughness and failure mechanism of graphene based epoxy composites. Composites Science and Technology, **97**, 90–99 (2014). DOI: 10.1016/j.compscitech.2014.03.014

[29] Bortz D. R., Heras E. G., Martin-Gullon I.: Impressive fatigue life and fracture toughness improvements in graphene oxide/epoxy composites. Macromolecules, **45**, 238–245 (2011). DOI: 10.1021/ma201563k